Numerical prediction for thixotropic and non-thixotropic material systems in complex flow.

Tabatabaei, Sorour

Numerical Prediction for Thixotropic and non-Thixotropic Material Systems in Complex Flows

by

SOROUR TABATABAEI
B.Sc., M.Res.

SUBMITTED TO SWANSEA UNIVERSITY IN THE
FULFILMENT OF THE REQUIREMENTS FOR THE DEGREE OF
DOCTOR OF PHILOSOPHY

Swansea University
Prifysgol Abertawe

University of Wales Swansea
SEPTERMBER 2014

ProQuest LLC.
789 East Eisenhower Parkway
P.O. Box 1346
Ann Arbor, MI 48106 – 1346

DEDICATION

To my son, Mohammad.
To my daughter, Mogeh.
To my mother, Batoul.
To my father, Mostafa.
And, to my family.

I dedicate this work,
giving thanks to them and to
GOD.

Acknowledgements

This study would not have been possible without the contributions of many people.

First and foremost, I would like to express my thanks to my supervisor, Prof. M. F. Webster, for his supervision, insightful ideas, valuable advice in science discussion and constant support on my project. I learnt from him the ways to organize research and to present results, which will greatly benefit me in my future career. I convey special acknowledgment to Prof. Rhodri Williams, who provided intellectual support, giving me the opportunity to flourish and allow me to grow. I acknowledge the always friendly assistance, guidance and contributions of Dr. H. Tammadon-Jahromi and also departmental staff for their help throughout the studies.

Many thanks to Dr. Dan Curtis who was the first person I would seek help from for my rheological measurement work. Dr. Nafiseh Badiei was kindly answering some of my questions. Thank you.

I gratefully acknowledge the financial support provided by the EPSRC and Procter & Gamble. I acknowledge

I offer my regards to all my friends who supported me in any respect during my student career and expressing my apology that I could not mention you all personally one by one.

I take this opportunity to express my profound gratitude to my parents for their moral support and prayers. This thesis is dedicated to them and to my deceased brother. I also wish to thank my sisters for their endless love. Last but not least, I would like to share this thesis and the happiness of completing it with my beloved children for their love and patience during my study.

CONTENTS

List of Figures

List of Tables

Summary

The focus of the present work has been on viscoelastic flows through 4:1:4 hyperbolic contraction/expansion geometries, filament stretching and rheological properties of polymer melts. In this study, a time-dependent hybrid finite element/finite volume (*fe/fv*) parent-subcell scheme has been employed to solve the governing equations (mass and momentum conservation and constitutive model). Here, the *fe/fv* algorithm utilizes a time-stepping method to advance to temporal solutions or steady-state conditions.

In the study of complex flow through hyperbolic 4:1:4 contraction/expansion configurations, two types of rheological models have been used to investigate the rheological behaviour of wormlike micellar solutions. Here, the time-dependent thixotropic MBM and network-based time-independent EPTT models have been compared. At low-levels of elasticity ($We \rightarrow 0$), the MBM model inconsistently predicted *epd*–values, as opposed to the network-based EPTT. This has lead to the examination of new models (NM_τ_p and NM_T) for this purpose, which introduce elastic effects into the structure (destruction) equation. As a complimentary contribution, the influence of the shape of the contraction/expansion configuration and its effects on *epd* prediction has also been demonstrated, by comparing complimentary findings for rounded-corner abrupt 4:1:4 geometry flows.

In the study of rheological measurements for polymer melts, it has been found that viscoelastic properties cannot be effectively investigated by a single frequency-sweep, since the substance is changing dramatically during the measurement. Hence, the method of taking data in a few intervals of frequency (discrete frequency-sweep) has been proposed and adopted to avoid such issues, with either long exposure time at high temperature, or whilst taking data in a time shorter than the thermal stability time. This approach has allowed for a small improvement in precision under the data acquisition. This has satisfied one goal to improve the measurement techniques and address some possible errors in experiments; whilst also allowing these experimental data to be used as characteristic material input-data to the simulation software under polymer processing conditions.

Also experimental and computational studies of Capillary Break-up Extensional Rheometry (CaBER) have been considered to predict extensional rheological response of biofluid sputum, and correlate this to the degree of infection in patients suffering from Chronic Obstructive Pulmonary Disease (COPD). Hence, a measure of extensional rheology through R_{mid}-evolution of sputum (experimental), has been compared against that derived from numerical prediction for two models - SXPP and MBM. The aim here has been to link numerical data with that emerging from experimental/clinical trials to provide a diagnostic tool (biomarker), revealing insight on state of disorder and impact upon its resultant treatment. The broad distribution of experimental results across three patient-samples suggests the necessity of adopting specific criteria, to derive consistent correlations between infected versus uninfected data. In this manner, three different criteria have been investigated, the most appropriate of which has been found to be that, with the longest-time to break-up amongst the infected data, as well as the larger extensional viscosities (η_e). For the uninfected data, the closest R_{mid} starting-value to the infected state has been chosen (equivalencing their step-strain Hencky-strain). The sensitivity of simulation results to the choice of aspect ratio (L/D=1.6, 1.8 and 2) has also been investigated to predict suitable windows for experimental operation sets. The outcome suggests that the results commencing from a Hencky-strain two is the superior choice to adopt.

To me there has never been a higher source of earthly honour or distinction than that connected with advances in science.

Sir Isaac Newton

Chapter 1
Introduction

Fluid mechanics deals with fluids (gases or liquids), either in rest or in motion, and the forces that act upon them. In physical science, fluid dynamics is the study of the effect of forces on fluid motion. Historically, the study and practice of fluid dynamics concerned the use of pure theory or pure experiments. However, introducing the advanced computer as a tool for analysis, combined with the progress of accurate numerical techniques for solving model problems from the physical world, has transformed the approach of study and practice in fluid dynamics today. Computational Fluid Dynamics (CFD) approach has emerged and acts as an equal co-partner with theory and experimental techniques in the analysis and solution of

fluid dynamics problems. Hence, today CFD is playing a leading role in the understanding and interpretation attached to the results of theory and experimental measurements, and vice versa. Computational rheology is a sub-discipline of CFD which deals with complex non-Newtonian fluids. The main challenge to the computational rheologist is to be able to apply numerical techniques to efficiently predict the rheological characteristics of complex fluids in practical complex flow scenarios.

Personal care products, paints, inks, moulded plastics, food products, blood and mucus are some examples of rheologically complex fluids. Understanding the performance of these complex fluids under flowing conditions is of high importance in many industrial processes, such as coating, extrusion and injection moulding or natural processes within the human body. Three fundamental laws of conservation of mass, linear momentum and energy, along with a set of constitutive equations, can be applied to the analysis of any viscoelastic fluid flow problem. Here, the constitutive equations link the dynamic description of the state of stress to the material deformation in the flow. In order to evaluate the quality of the appropriate constitutive equations to the particular fluid properties involved, one can combine numerical-experimental and laboratory-experimental approaches together.

An appropriate choice of viscoelastic constitutive equation remains an open and challenging issue. For solving some flow problems, enhancement in both constitutive modelling and numerical techniques is crucial. Many constitutive equations have been introduced throughout the last decade, but none have been established as absolutely universal in application [1.1,1.2]. Hence, new and more realistic constitutive models are continuously being developed to represent more complex systems; or, to improve on those whose satisfactory description has been lacking or ambiguous [1.2]. These developments would include kinetic-theory pom-pom, network-theory non-thixotropic Phan-Thien Tanner (PTT) and thixotropic Bautista–Manero (BM) models. Industrial applications that involve polymer melts and solutions, such as plastics, paint and ink, makes their computer simulation and prediction a subject of high importance in todays modern society.

The PTT model, based on network-theory, is held to be most effective in representing the properties of polymer melts and solutions. Additionally, the

relatively new pom-pom models, based on kinetic tube-theory, have improved the performance representation of branched polymeric systems, in both extensional and shear flow situations. In contrast, the thixotropic BM models are proposed to represent the unique rheological phenomena typically demonstrated by viscoelastic surfactant (worm-like micellar) systems, so common in biofluids.

Surfactant solutions, capable of aggregating to form giant worm-like micelles, can behave in a manner comparable to that displayed by polymeric systems. These wormlike micellar solutions are self-assembled and exhibit rapid evolution in structure, and therefore, in rheological behaviour [1.3]. The remarkable rheological properties of these solutions have led to their expansive use as rheological modifiers in many consumer/personal care products, such as paints, detergents and shampoos. Moreover, viscoelastic surfactant solutions are currently being used in a wide range of industrial applications including examples within oil fields as fracturing-fluids (enhanced-oil-recovery), and in hydrodynamic engineering as drag-reducing agents [1.4,1.5]. The modelling of these types of solutions requires appropriate rheological models capable of predicting structural change (construction and destruction). Of this variety, the BM models have been introduced recently to deal in particular with the modelling of wormlike micellar solutions. These BM models are based on the Oldroyd-B model, coupled with a dynamic accompanying equation for fluidity (viscosity inverse), comprising of thixotropic parameters that govern structural change.

The flow through a contraction/expansion configuration has more recently become established as a standard benchmark problem in experimental and computational rheology [1.6]. This also closely represents the typical shape of a bottle-neck of industrial interest for holding or distributing personal care products, such as shampoos. The first point of which is to focus on the accurate prediction of excess pressure-drop (*epd*). This in itself stands as a 'grand-challenge' to the field of computational rheology [1.6,1.7], more particularly for constant viscosity strain-hardening types of fluids. Such an extra pressure loss is observed in axisymmetric contraction/expansion flows, for constant-viscosity Boger fluids and shear-thinning elastic liquids, over that presented by an equivalent Newtonian fluid of similar

viscosity. As argued in chapter 4, the modelling of such phenomena requires robust and reliable rheological models.

The research conveyed in this thesis aims to investigate the flow performance of rheologically complex fluids (computational rheology) in two areas: flows in axisymmetric hyperbolic 4:1:4 contraction/expansion configurations, and filament stretching apparatus (Capillary Break-up Extensional Rheometer_CaBER). In addition, rheological characterization (experimental rheology) of three polymer melts has been carried out. The simulation work has been conducted using a Taylor-Galerkin Pressure-Correction [1.8], time-dependent hybrid finite element/finite volume (*fe/fv*) parent-subcell software suite for solving viscoelastic flow problems, developed in-house by the Swansea computational rheology group. This software, and its associated algorithms, has proven itself well capable of solving the range of flow-settings and configurations of current interest [1.9-1.19].

After this general introduction on computational rheology and the flow of thixotropic material in complex geometry, the presentation of the work proceeds in chapter 2 to provide a general background to the governing equations, rheometrical flows (pure shear and pure extensional flows) and various relevant and related viscoelastic constitutive equations. In particular, the MBM model and its material functions have been highlighted, providing some of the adjustments proposed for this type of model. Additional and supportive rheological plots are included in later chapters, as and where necessary; see for instance, discussion on the new micellar models covered in chapter 4. Moreover, different types of rheometers, with their functionality and practical use, are also described.

Chapter 3 outlines the details on the numerical procedures employed in this thesis (hybrid finite element/finite volume subcell (*fe/fv*) method). This covers the basis and derivation of such a scheme, as it is deployed in solving the current isothermal incompressible viscoelastic flow problems of immediate interest.

Modelling of flow through a rounded-corner hyperbolic 4:1:4 contraction-expansion geometry, of axisymmetric configuration, is considered in chapter 4, whilst appealing to three types of constitutive models - the MBM model (for base thixotropic properties), the new micellar models (NM_τ_p & NM_T; for advanced

thixotropic modelling), and the EPPT model (for non-thixotropic properties). Focus is given to interpret the flow behaviour of these constitutive models, employed in this configuration, against their response in simple rheometrical flows (characterization of their material functional response). For this purpose, this study reports on the relationship between the pressure-drop, the first normal stress difference, the strain rate across the geometry and the material functions involved. Here, the flow is considered under laminar, isothermal, and incompressible flow conditions. To determine the factors that contribute to *epd*-prediction, a supplementary study has been prepared by comparing current findings against those reported earlier in abrupt axisymmetric, rounded-corner, 4:1:4 contraction-expansion flows of Lopez-Aguilar et al. [1.20].

Chapter 5 presents the experimental work and characterisation results for three polymer-melts. This section focuses on the determination of the dynamic viscoelastic properties of High-Density Polyethylene (HDPE), Nylon 11 (Polyamide-PA11) and Poly-Vinylidene Fluoride (PVDF) melt, which were measured using a controlled-strain rheometer (TA Instruments ARES-G2), for the temperature range of 220-240 ^{o}C. Using the Cox-Merz rule, dynamic oscillatory data (in terms of $G^{'}, G^{''}$) were fitted to predictions according to the Cross model. The experimental data collected in this part of the study was used by others as characteristic material input-data to the same simulation software suite as used here (see [1.21]). A quantitative practical comparison is described in chapter 6 between experimental data for a bio-fluid (sputum), derived from a FiSER-CaBER apparatus, against corresponding numerical simulations, using the techniques explored above. Here, a full description is provided of the dynamic free-surface problem specification and variations required to the numerical algorithm. The selection of constitutive models used in this section of work included the Pom-Pom and the MBM models. Finally, in chapter 7 conclusions are presented, along with some general remarks and recommendations for future work.

References

[1.1] R.G. Larson, *A critical comparison of constitutive-equations for polymer melts*, J. Non-Newtonian Fluid Mech. **23** (1987) 249-269.

[1.2] R.G. Larson, *Constitutive equations for polymer melts and solutions*, Butterworths, (1988).

[1.3] E.S. Boek, A. Jusufi, H. Löwen, G.C. Maitland, Molecular design of responsive fluids: molecular dynamics studies of viscoelastic surfactant solutions, *Journal of Physics: Condensed Matter* **14** (2002) 9413-9430

[1.4] J. Yang, *Viscoelastic wormlike Micelles and their Applications*, Curr. Opin. Colloid Interface Sci. **7**, 276 - 281 (2002).

[1.5] M.J. Rosen, M. Dahanayake, *Industrial Utilization of Surfactants: Principle and Practice*, Champaign, Illinois, AOCS Press (2000).

[1.6] K. Walters, M.F. Webster, *The distinctive CFD challenges of computational rheology*, Int. J. Numer. Meth. Fluids 43 (2003) 577–596.

[1.7] D.M. Binding, P.M. Phillips, T.N. Phillips, *Contraction/expansion flows: the pressure drop and related issues*, J. Non-Newtonian Fluid Mech. **137** (2006) 31–38.

[1.8] P. Townsend and M.F. Webster, *An algorithm for the three-demensional transient simulation of non-Newtonian fluid flows*, G.E. Pande, J. Middleton, Int. Conf. Numerical Methods in Engineering: Theory and Applications - NUMETA 87, Kluwer, (1987), T12/11-11.

[1.9] M. Aboubacar, T.N. Phillips, H.R. Tamaddon-Jahromi, B.A. Snigerev and M.F. Webster, *High-order finite volume methods for viscoelastic flow problems*, Journal of Computational Physics **199** (2004) 16-40.

[1.10] M. Aboubacar and M.F. Webster, *A cell-vertex finite volume/element method on triangles for abrupt contraction viscoelastic flows*, Journal of Non-Newtonian Fluid Mechanics **98** (2001) 83-106.

[1.11] A. Baloch, P. Townsend and M.F. Webster, *On the simulation of highly elastic complex flows*, J. Non-Newtonian Fluid Mech. **59** (1995) 111-128.

[1.12] E.O.A. Carew, P. Townsend and M.F. Webster, *A Taylor-Petrov-Galerkin algorithm for viscoelastic flow*, J. Non-Newtonian Fluid Mech. **50** (1993) 253-287.

[1.13] D.M. Hawken, H.R. Tamaddon-Jahromi, P. Townsend and M.F. Webster, *A Taylor-Galerkin-based algorithm for viscous incompressible flow*, International Journal for Numerical Methods in Fluids **10** (1990) 327-351.

[1.14] P. Wapperom and M.F. Webster, *A second-order hybrid finite element/ volume method for viscoelastic flows*, J. Non-Newtonian Fluid Mech. **79** (1998) 405-431.

[1.15] P. Wapperom and M.F. Webster, *Simulation for viscoelastic flow by a finite volume/element method*, Computer Methods in Applied Mechanics and Engineering **180** (1999) 281-304.

[1.16] M.F. Webster, H.R. Tamaddon-Jahromi and M. Aboubacar, *Time-dependent algorithm for viscoelastic flow-finite element/volume schemes*, Numerical Methods for Partial Differential Equations **21** (2005) 272-296.

[1.17] M. Aboubacar, H. Matallah, H.R. Tamaddon-Jahromi, M.F. Webster, *Numerical prediction of extensional flows in contraction geometries: hybrid finite volume/element method*, J. Non-Newtonian Fluid Mech. **104** (2002) 125-164.

[1.18] M. Aboubacar, H. Matallah, M.F. Webster, *Highly elastic solutions for Oldroyd-B and Phan-Thien/Tanner fluids with a finite volume/element method: planar contraction flows*, J. Non-Newtonian Fluid Mech. **103** (2002) 65-103.

[1.19] M. Aboubacar, M.F. Webster, *Development of an optimal hybrid finite volume/element method for viscoelastic flows*, International Journal for Numerical Methods in Fluids **41** (2003) 1147-1172.

[1.20] J.E. López-Aguilar, M.F. Webster, H.R. Tamaddon-Jahromi, O. Manero, *A new constitutive model for worm-like micellar systems - Numerical simulation of confined contraction-expansion flows*. J. Non-Newtonian Fluid Mech. **204** (2014) 7-21.

[1.21] A, Al-Muslimawi, H.R. Tamaddon-Jahromi and M.F. Webster, *Numerical computation of extrusion and draw-extrusion cable-coating flows with polymer melts.* Appl. Rheol. **24** (2014) 34188. DOI: 10.3933/ApplRheol-24-34188

All the mathematical sciences are founded on relations between physical laws and laws of numbers, so that the aim of exact science is to reduce the problems of nature to the determination of quantities by operations with numbers.

James Clerk Maxwell

Chapter 2

Rheology and Rheometry

This chapter delivers introductory concepts in rheology, the characteristics of viscoelastic materials and fluids, the basic equations of fluid mechanics (conservation laws), simple (rheometric) flows and constitutive equations. In addition, rheological models are considered, which provide physical interpretation of viscoelastic behavior. Models such as Maxwell, Oldroyd-B, Phan-Thien/Tanner, are addressed briefly. A more recent type of constitutive equation, the MBM model and its response in rheometrical flows, is also expressed in some detail. Moreover, two

characteristically different types of rheometer are introduced, these being those used to primarily determine shear properties and those counterparts used for extensional properties.

2.1 Introduction

Rheology is part of the physical sciences and is concerned with the description of flow and deformation of materials, in a liquid or soft-solid state, under the effects of applied force (external and internal forces). Newtonian fluids can be characterized by a constant coefficient of viscosity regardless of any prevailing external stress, for a particular pressure and temperature. In other words, these fluids have a linear relationship between viscosity and shear stress or strain rate. Only a small group of fluids demonstrate such a constant viscosity behaviour. This can be contrasted with non-Newtonian fluids (covering a large class of fluids), whose viscosity and viscoelasticity depends either on the applied shear rate or on the history of the fluid. As such, they can become thicker or thinner when exposed to an external stress. Additionally, internal variations are also a fundamental factor that contributes to the bulk rheological properties of a material. In general, rheologists are interested in the flow of non-Newtonian complex fluids.

Viscoelastic materials are a special case of non-Newtonian fluids. To clarify the term viscoelastic, it is appropriate to outline a general classification of solids and liquids. If a material retains its shape when subject to an external stress, it is referred to as a solid; whilst, if the change in shape is continuous and irreversible (flow) with the applied stress, the material is characterized as a liquid (see Barnes et al. [2.1]). As a result, two limiting elastic and viscous responses can be represented through the corresponding two fundamental laws of Hook and Newton. Both are linear laws, which adopt linear proportionality relationships, regardless of the degree of applied stress: between stress and strain (in the case of a deforming solid), and between stress and strain rate (in the case of a flowing fluid). This interdisciplinary field is often governed by research on materials with industrial application, whose properties fall

between those of ideal solids and ideal liquids, which occupy two ends of the material description spectrum. Viscoelastic materials exhibit both solid-like (elasticity) and liquid-like (viscous) response. Accordingly, the relationship between stress and deformation for these types of material proves a combination of a partly-viscous contribution and a partly-elastic one. Thus, neither Newton's law of viscosity, nor Hooke's law of elasticity, prove adequate to completely describe the flow behavior of such complex fluids. For a given material and a flow state, after termination of applied stress, the time of the fluid to relax can also be determined to supply a relaxation time.

All the research carried out in the present study applies the general concept of continuum mechanics. Modeling substances at a continuum level essentially absorbs those process and interactions that are transmitted at inter-molecular distances, with the change in properties due to these lengths, to represent their consequence at this larger level of length description. Continuum mechanics is a combination of mathematics and fundamental physical laws, such as energy, mass and force balances; that approximate the large-scale behaviour of a material that is subjected to mechanical stress. Modeling objects in this way, we normally choose an arbitrary large number of molecules, a fluid element, to average properties and describe motion. To describe the behaviour of a fluid element under deformation, fundamental balance laws (conservation laws) are applied via temporal-spatial differential and integral operators over appropriately small volumes (large enough to satisfy the continuum assumption). A constitutive equation, or stress equation of state (stress-strain interaction relation), proves to supply a vital connection between material property description from rheology and the laws of flow under continuum mechanics. As such and together, these conservation laws and constitutive equations (stress-strain laws) may be appealed to adequately represent the flow of realistic materials. Thus, determining a suitable equation relating stress and strain for any specific material becomes a principal concern. These models must be selected and adjusted carefully to suit any particular application and deformation state.

2.2 Viscoelastic Fluid Flow Equation

Following on from above, the equations governing incompressible laminar isothermal fluid motion therefore consist of three sets of equations resulting from the conservation of mass and linear momentum, along with a constitutive equation for stress. From the condition of incompressibility, mass conservation is converted into a continuity equation.

2.2.1 Conservation of Mass

The conservation of mass (a fundamental concept of physics) states that the amount of mass in any closed flow system remains constant, mass is neither created nor destroyed. This law implies that the rate of increase of mass in an arbitrary control volume V equals the net influx of mass crossing its surrounding surface area S. This can be expressed mathematically in integral form as:

$$\frac{\partial}{\partial t}\int_V \rho dv = -\oint_S \rho \boldsymbol{u}.\boldsymbol{n} ds\,, \tag{2.1}$$

In this form, ρ represents the fluid density, **u** the fluid velocity vector, **n** the unit surface normal vector (defined positively in the outward direction from the surface) and t represents the independent time variable. Applying the divergence theorem[1] to Eq. (2.1), the differential form of the mass conservation is written as:

$$\frac{\partial \rho}{\partial t} + \nabla \cdot (\rho \mathbf{u}) = 0\,, \tag{2.2}$$

[1] The divergence theorem relates the flow (flux) of a vector through a surface to the state of the vector field inside the surface.

For isothermal and incompressible flow, where ρ is taken as a constant in time and spatial distribution, Eq. (2.2) reduces to the continuity equation:

$$\nabla \cdot \mathbf{u} = 0, \tag{2.3}$$

2.2.2 Conservation of Linear Momentum

Newton's second law of the motion (identified as the principle of conservation of linear momentum) states that, the change of linear momentum in a system is equal to the sum of the external forces acting upon it.

This law implies that the rate of increase of momentum in any arbitrary control volume *V* equates to the net influx of momentum, crossing its surrounding surface area *S,* plus any external forces. The external forces can be classified into two distinct groups of forces, body forces (such as gravitational and electromagnetic forces) and surface forces. The surface force can be described through the Cauchy stress tensor. This can be expressed in differential form as:

$$\frac{D(\rho \mathbf{u})}{Dt} = \nabla \cdot \boldsymbol{\sigma} + \rho \boldsymbol{g} \ , \tag{2.4}$$

where $\boldsymbol{\sigma}$ is the Cauchy stress tensor. This is a combination of the extra-stress tensor (**T**), and isotropic pressure, as:

$$\boldsymbol{\sigma} = -p\boldsymbol{I} + \boldsymbol{T} \tag{2.5}$$

In this equation, *p* is the isotropic pressure, **I** is the identity tensor and **T** (extra-stress tensor) accounts for viscous/viscoelastic phenomena. Using the definition of a total convected derivative as,

$$\frac{D}{Dt} = \frac{\partial}{\partial t} + \boldsymbol{u}.\nabla \tag{2.6}$$

and neglecting body or gravitational forces ($\boldsymbol{g}$), due to insignificant contributions in comparison to other forces such as pressure or stress, the momentum transport equation can be expressed as:

$$\rho\left(\frac{\partial \mathbf{u}}{\partial t}+\mathbf{u}\cdot\nabla\mathbf{u}\right)=-\nabla p+\nabla\cdot\mathbf{T}. \tag{2.7}$$

2.2.3 Constitutive Equations

As expressed above, the constitutive equation or rheological equation of state, deals with supplying a mathematical model to relate applied stress to strain (or deformation) experienced by a material. Apart from experimental observations, such derived constitutive equations must also satisfy some theoretical and basic mathematical principles, considerations to effectively represent fluid response from a mathematical point of view [2.2,2.3].

- ***Stress Determinism***: The stress acting on a viscoelastic fluid at a given point in a flow is determined by the history of the motion of that point.

- ***Local action***: The stress at any spatial point in the fluid is influenced by the history of the deformation in the neighbourhood around that point.

- ***Frame indifference***: The constitutive equations must be independent of the coordinate frame of reference. Based on the principle that constitutive equations characterize inherent properties of a material, they must be *'frame invariant'*.

- ***Invariance under superposed rigid body motion***: Any rigid body motion imposed on the whole fluid must not influence the response of the material.

2.3 Standard Rheometrical Flow

To investigate the behaviour of a fluid in a complex flow setting, it is essential to study the behaviour of that fluid in simple well-defined *'ideal flows'*. The two typical sets of flows, simple shear and elongation deformation, are those conventional flows

used for this purpose and in rheological measurement. A requirement is that these two flow types should be sufficiently simple, so that either their corresponding velocity field or stress tensor can be easily calculated from the proposed constitutive equation, or that the flow should be practically feasible under experimental good practice.

2.3.1 Simple Shear Flow

For a simple shear flow we consider the situation represented in Figure 2.1. The fluid is restricted between two parallel flat-surfaces, separated by a gap h, with the upper-plate moving at constant velocity U. To maintain the constant velocity of the plate, an applied stress (σ) is necessary which is proportional to the velocity gradient ($\dot{\gamma}$ is the shear rate), i.e.

$$\sigma = \eta_s(\dot{\gamma})\dot{\gamma}, \tag{2.8}$$

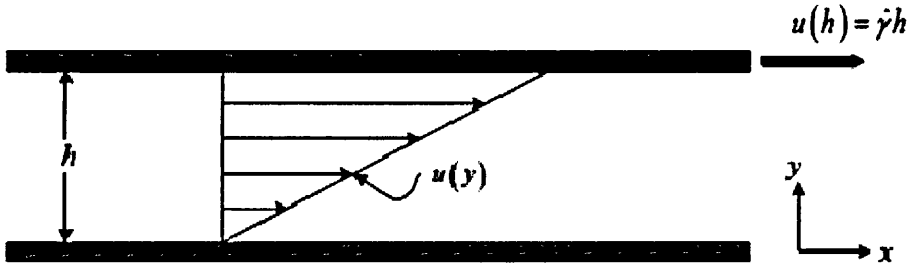

Figure 2.1. Schematic diagram of simple shear flow under constant shear-rate

For a Newtonian fluid, viscosity (η_s) is constant under all shear-rates. In simple shear, the velocity field is $\mathbf{u} = (u, v, w) = \dot{\gamma}(y, 0, 0)$ and the velocity gradient in this case (in Cartesian coordinate) is defined as:

$$\nabla \mathbf{u} = \begin{bmatrix} 0 & 0 & 0 \\ \dot{\gamma} & 0 & 0 \\ 0 & 0 & 0 \end{bmatrix}, \tag{2.9}$$

The shear rate tensor $\dot{\gamma}$ for this flow is then given by:

$$\overset{\square}{\gamma} \equiv \nabla \mathbf{u} + \nabla \mathbf{u}^T = \begin{bmatrix} 0 & \dot{\gamma} & 0 \\ \dot{\gamma} & 0 & 0 \\ 0 & 0 & 0 \end{bmatrix}, \tag{2.10}$$

The properties that vary between Newtonian and non-Newtonian fluids are the first (N_1) and second (N_2) normal stress difference. Their magnitudes are zero for the case of Newtonian fluids, whilst for non-Newtonian fluids, they are defined as:

$$N_1(\dot{\gamma}) = \sigma_{xx} - \sigma_{yy} = \psi_1(\dot{\gamma})\dot{\gamma}^2, \tag{2.11}$$

$$N_2(\dot{\gamma}) = \sigma_{yy} - \sigma_{zz} = \psi_2(\dot{\gamma})\dot{\gamma}^2, \tag{2.12}$$

where ψ_1 and ψ_2 are known as primary and secondary normal stress coefficients, respectively.

2.3.2 Uniaxial Elongational Flow

There are three different types of extensional (shear-free) deformation, namely, uniaxial, biaxial and planer; each categorized according to their velocity and deformation rate profiles. Here, we consider uniaxial elongational flow (see Figure 2.2) in which the flow is stretched (exposing a positive constant extensional rate) in one particular direction, where the extension is maximum in magnitude. Due to the incompressibility[2] condition, the flows in the other two directions will tend to

[2]The flow is incompressible if the divergence of the velocity field is identically zero.

compress equivalently. In general, pure extensional flow occurs along the centreline in a contraction and contraction/expansion flow geometry.

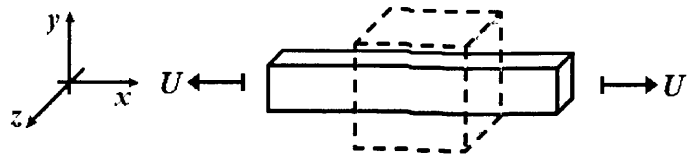

Figure 2.2. Schematic diagram of uniaxial elongational flow

In steady uniaxial extensional flow, the velocity field and velocity gradient are expressed as:

$$\begin{aligned} u(x) &= \dot{\varepsilon}\, x \\ v(y) &= -\tfrac{1}{2}\dot{\varepsilon}\, y \\ w(z) &= -\tfrac{1}{2}\dot{\varepsilon}\, z \end{aligned} \quad , \qquad \& \qquad \nabla \mathbf{u} \approx \begin{bmatrix} \dot{\varepsilon} & 0 & 0 \\ 0 & -\tfrac{1}{2}\dot{\varepsilon} & 0 \\ 0 & 0 & -\tfrac{1}{2}\dot{\varepsilon} \end{bmatrix}, \tag{2.13}$$

where $\dot{\varepsilon}$ is the strain or extensional rate. The resistance, or extensional viscosity, is then defined through the relationship:

$$\eta_e(\dot{\varepsilon}) = \frac{\sigma_{xx}(\dot{\varepsilon}) - \sigma_{yy}(\dot{\varepsilon})}{\dot{\varepsilon}}\ , \tag{2.14}$$

For a Newtonian fluid, viscosity (η_e) is a constant under all shear-rates, and the subsequent relation is satisfied:

$$\eta_e = 3\eta_s \qquad (\textit{Newtonian}) \tag{2.15}$$

At all deformation rates, it is expected that all fluids, including those with viscoelastic properties, fulfil (2.15), that is,

$$\eta_e(\dot{\varepsilon} \to 0) = 3\eta_s(\dot{\gamma} \to 0) \qquad (\textit{Viscoelastic}) \tag{2.16}$$

The ratio of extensional to shear viscosity is defined as the Trouton ratio (Tr). The Trouton ratio, proposed by Jones et al. [2.4], for uniaxial elongational flow can be defined as:

$$Tr = \frac{\eta_e(\dot{\varepsilon})}{\eta_s\left(\dot{\gamma} = \sqrt{3}\,\dot{\varepsilon}\right)}\,, \tag{2.17}$$

This ratio, for all values of $\dot{\varepsilon}$, for inelastic fluids assumes the constant value of three. Additionally, for viscoelastic fluids this Trouton ratio is anticipated to satisfy,

$$Tr(\dot{\varepsilon} \to 0) = 3 \tag{2.18}$$

2.4 Constitutive Models

Constitutive equations (or their derived and associated models) establish a relationship between stress, rate-of-change of stress and deformation rate. They can be expressed in either differential or integral form: in the present work, only the differential form is considered. Such constitutive equations can be classified into those derived from simply phenomenological[3] observation, and those models derived from underlying theory (first principles). Classical cases of phenomenological models are Maxwell model, Oldroyd-B model. The PTT model, based on network theory, and the pom-pom model, based on tube-kinetic theory, are just some examples of typical constitutive models of relevance to this work and derived from background theory.

For an incompressible Newtonian fluid, the purely viscos stress is given by,

$$\mathbf{T} = 2\mu\mathbf{D}\,, \tag{2.19}$$

[3] Phenomenological models try to model a system based on observations of phenomena occurring.

where **D** is the rate-of-deformation tensor, expressed as:

$$\mathbf{D} = \tfrac{1}{2}\left(\nabla\mathbf{u} + \nabla\mathbf{u}^{\mathrm{T}}\right), \tag{2.20}$$

As discussed above, μ is the constant shear viscosity. Also, the extensional viscosity for a Newtonian fluid is constant in extension. Note that more complex fluids under small deformation also manifest Newtonian-like behaviour. With a generalized Newtonian fluid, the shear viscosity is not constant, but a function of the shear-rate, expressed by,

$$\mathbf{T} = 2\mu(\dot{\gamma})\mathbf{D}, \tag{2.21}$$

The elastic-viscous stress-splitting (EVSS) concept, which introduces a derived extra-stress tensor variable, was first introduced by Perera and Walters [2.5],

$$\mathbf{T} = \boldsymbol{\tau}_s + \boldsymbol{\tau}, \tag{2.22}$$

This technique applies splitting of extra-stress into its viscous and elastic (polymeric) terms, and modifies variable reference in the momentum and constitutive equations, producing a set of equations involving the velocity **u**, the pressure p, and new additional elastic-stress $\boldsymbol{\tau}$.

2.4.1 Maxwell Model

The Maxwell model [2.6] is considered as the simplest constitutive equation to model viscoelastic fluids. The general form for this model in tensor form is,

$$\mathbf{T} + \lambda\dot{\mathbf{T}} = 2\mu\mathbf{D}. \tag{2.23}$$

where λ represent the characteristic (relaxation) time of the material. Replacing the original time derivative in (2.23) by a convective derivative alternative, this equation (2.23) can be re-written as the upper-convected Maxwell (UCM) model,

$$\mathbf{T}+\lambda\overset{\nabla}{\mathbf{T}}=2\mu\mathbf{D}. \tag{2.24}$$

or the lower-convected Maxwell (LCM) model,

$$\mathbf{T}+\lambda\overset{\Delta}{\mathbf{T}}=2\mu\mathbf{D}. \tag{2.25}$$

where the upper- ($\overset{\nabla}{\mathbf{T}}$) and lower- ($\overset{\Delta}{\mathbf{T}}$) convected derivative of the extra-stress tensor are expressed, respectively, as:

$$\overset{\nabla}{\mathbf{T}}=\frac{\partial}{\partial t}\mathbf{T}+\mathbf{u}\cdot\nabla\mathbf{T}-\left(\nabla\mathbf{u}^{\mathrm{T}}\cdot\mathbf{T}+\mathbf{T}\cdot\nabla\mathbf{u}\right), \tag{2.26}$$

$$\overset{\Delta}{\mathbf{T}}=\frac{\partial}{\partial t}\mathbf{T}+\mathbf{u}\cdot\nabla\mathbf{T}+\left(\nabla\mathbf{u}^{\mathrm{T}}\cdot\mathbf{T}+\mathbf{T}\cdot\nabla\mathbf{u}\right), \tag{2.27}$$

The both UCM and LCM models include memory effects and first normal stress differences.

2.4.2 Oldroyd-B Model

The Maxwell model does not include a term to express solvent presence. To overcome this deficiency, a characteristic retardation time, λ_J, is introduced into the equation for the UCM model (2.24);

$$\mathbf{T}+\lambda\overset{\nabla}{\mathbf{T}}=2\mu\left(\mathbf{D}+\lambda_J\overset{\nabla}{\mathbf{D}}\right). \tag{2.28}$$

Equation (2.28) is known as the upper-convected Jeffreys or Oldroyd-B model [2.7]. Referring to equation (2.22), under an EVSS construction, the model is split into two different equations, one for the solvent (viscous) contribution and the other for polymeric (elastic) component, i.e.

$$\boldsymbol{\tau}_s=2\mu_s\mathbf{D}, \tag{2.29}$$

$$\boldsymbol{\tau} + \lambda \overset{\nabla}{\boldsymbol{\tau}} = 2\mu_p \mathbf{D}, \tag{2.30}$$

in which,

$$\mu = \mu_s + \mu_p \qquad \text{and} \qquad \lambda_J = \frac{\mu_s}{\mu_s + \mu_p}\lambda, \tag{2.31}$$

In equations (2.29)-(2.31) $\boldsymbol{\tau}$ and μ_p represent the polymeric stress and zero shear-rate viscosity contributions, respectively; likewise, $\boldsymbol{\tau}_s$ and μ_s are the contributions to the solvent component. This model does not support shear-thinning behaviour; yet, it does predict a non-zero response in N_1 under shear. Both, Maxwell and Oldroyd-B, models predict the same unbounded response in extensional viscosity, tending to infinity as the strain-rate approaches to $1/(2\lambda)$. In addition, both model forms and for all shear-rates, predict a constant shear viscosity and a vanishing N_2 in shear (with the exception of lower convected model alternatives that would predict a non-zero N_2).

2.4.3 Phan-Thien/Tanner (PTT) Model

This model was introduced by Phan-Thien and Tanner (PTT) based on the network theory (for polymer network and solutions) [2.8,2.9], considering the rate of creation and destruction of network junctions. The single relaxation time PTT constitutive equation may be expressed as,

$$f(\boldsymbol{\tau})\boldsymbol{\tau} + \lambda \overset{\square}{\boldsymbol{\tau}} = 2\mu_p \mathbf{D}, \tag{2.32}$$

Here, $\overset{\square}{\boldsymbol{\tau}}$ is the Gordon-Scholwalter convected derivative[4] and the general form of the extra function $f(\boldsymbol{\tau})$ is expressed as,

$$f(\boldsymbol{\tau}) = exp\left(\frac{\varepsilon\lambda}{\mu} Tr(\boldsymbol{\tau})\right). \tag{2.33}$$

The ε and ξ constants are two variable non-dimensional material parameters which contribute in controlling the extensional and shear response of the model. Through Taylor series expansion of the exponential term, the linear alternative form may be extracted and identified as,

$$f(\boldsymbol{\tau}) = \begin{cases} exp\left(\varepsilon_{PTT} \dfrac{\lambda}{\mu_p} tr(\boldsymbol{\tau})\right) & exponential, \\ 1 + \varepsilon_{PTT} \dfrac{\lambda}{\mu_p} tr(\boldsymbol{\tau}) & linear. \end{cases} \tag{2.34}$$

This class of models support Shear-thinning behaviour. Additionally, both model forms predict extension-hardening response in extensional viscosity, although strain-softening is expected for the exponential form, whilst the linear form displays sustained hardening except for some extreme values ($\varepsilon_{PTT} \to 1$) moderate softening is also detected.

2.4.4 Pom-Pom Model (SXPP)

The original pom-pom model was proposed by McLeish and Larson [2.10] to represent the behaviour of idealized polymer chains. This model is based on the tube-theory and takes into account the simplified topological structure of the polymer branched chains, see Figure 2.3. The polymer chains appear as a backbone segment

---

[4] Defined as: $\overset{\square}{\boldsymbol{\tau}} = \overset{\nabla}{\boldsymbol{\tau}} + \xi(\boldsymbol{\tau}.\mathbf{D} + \mathbf{D}.\boldsymbol{\tau})$.

with the same number of dangling-arms (q) attached at both limits of the backbone section. The drag that the melt exerts on these arms causes the backbone to stretch.

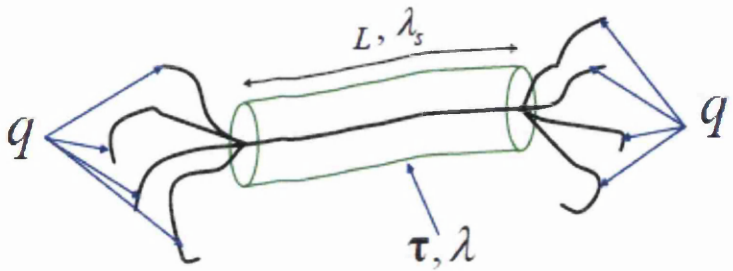

Figure 2.3. Schematic structure of pom-pom molecules

The existence of branching points slows down the backbone-reptation[5] development. The process of arm-retraction assists the molecule to free the polymer chain from the tube shaped by its environments. When the molecule reaches its maximum stretched condition the arm-retraction is activated and the arms slowly free from the tube by diffusion. The backbone stretch is represented by the parameter, which is the extension of the polymer chain scaled by its equilibrium length ($\lambda = L_{backbone} / L_{0_{backbone}}$).

A key feature of this type of model is the separation of stretch and orientation relaxation times. The model comprises of two decoupled equations, one for each relaxation process. An extended version of the original pom-pom model, Single-eXtended Pom-Pom (SXPP), introduced by Verbeeten et al. [2.11,2.12] to overcome

[5] Chain relaxation in tube theory along their confining tube.

three drawbacks encountered with the original formulation of the model, which is unbounded response at high strain-rates for the backbone orientation equation; discontinuities due to the finite extensibility (maximum backbone stretch) condition; and a zero second normal stress difference in shear. The evolution for the polymeric extra-stress in the (SXPP) model in differential form is,

$$\lambda_{0b}\overset{\nabla}{\boldsymbol{\tau}}+f(\boldsymbol{\tau})\boldsymbol{\tau}+\frac{\alpha}{G_0}\boldsymbol{\tau}\cdot\boldsymbol{\tau}+G_0\left[f(\boldsymbol{\tau})-1\right]\mathbf{I}=2\lambda_{0b}G_0\mathbf{D}, \tag{2.35}$$

where,

$$f(\boldsymbol{\tau})=2\frac{\lambda_{0b}}{\lambda_{0s}}\left(1-\frac{1}{\lambda}\right)e^{\nu(\lambda-1)}+\frac{1}{\lambda^2}\left(1-\frac{\alpha}{3G_0^{\,2}}Tr(\boldsymbol{\tau}\cdot\boldsymbol{\tau})\right), \tag{2.36}$$

Here, $\lambda_{0b}>\lambda_{0s}$ are the orientation and backbone stretch relaxation times, respectively; α is an isotropy parameter and G_0 is the linear relaxation modulus. The backbone stretch is directly coupled to the extra-stress tensor,

$$\lambda=\sqrt{1+\frac{1}{3G_0}\left|Tr(\boldsymbol{\tau})\right|}\,. \tag{2.37}$$

2.4.5 Bautista-Manero Model; Modified BM Model (MBM) Model

To investigate the rheological behaviour of wormlike micelle systems, Manero et al. [2.13] introduced a new model, Bautista-Manero (BM) model, akin in structure to the Oldroyd-B model for the stress, coupled with the kinetic equation. Such a model accounted for construction and destruction of the structure of micelles in fluid, which derived a constitutive system capable of producing shear-thinning and strain-hardening/softening response. This BM-model may be expressed through the following system of equations:

Extra-stress evolution for ($\boldsymbol{\tau}$),

$$\boldsymbol{\tau}+\frac{\eta}{G_0}\overset{\nabla}{\boldsymbol{\tau}}=2\eta\left(\mathbf{D}+\lambda_J\overset{\nabla}{\mathbf{D}}\right) \tag{2.38}$$

Kinetic equation for $(1/\eta)$,

$$\frac{\mathbf{d}}{\mathbf{dt}}\left[\eta^{-1}\right]=\underset{construction}{\frac{1}{\lambda_s}\left(\frac{1}{\eta_0}-\frac{1}{\eta}\right)}+\underset{destruction}{k\left(\frac{1}{\eta_\infty}-\frac{1}{\eta}\right)}\boldsymbol{\tau}:\mathbf{D}, \tag{2.39}$$

where λ_s is the structural relaxation time (micellar network construction), k the kinetic constant for structural breakdown (network destruction), G_0 the elastic modulus, λ_J the retardation time (associated to the solvent viscosity), η_0 and η_∞ are the zero and high shear-rate viscosity, respectively.

However, the BM-model predicts the unbounded response in extensional viscosity, even at finite deformation rates, presenting unphysical behaviour. In order to address this problem, Boek et al. [2.14], suggested a modified version of BM (MBM) model, in which the solvent (η_s) and polymeric (η_p) viscosity contributions are split. This MBM model, based on the EVSS concept $(\mathbf{T}=\boldsymbol{\tau}_s+\boldsymbol{\tau}_p)$, consists of Newtonian-type solvent contribution $(\boldsymbol{\tau}_s=2\mu_s\mathbf{D})$ and the polymeric terms (in dimensional form) represented through the following equations:

$$\boldsymbol{\tau}_p+\frac{\eta_p}{G_0}\overset{\nabla}{\boldsymbol{\tau}}_p=2\eta_p\mathbf{D}, \tag{2.40}$$

structure equation,

$$\frac{\partial}{\partial t}\left(\frac{1}{\eta_p}\right)=\frac{1}{\lambda_s}\left(\frac{1}{\eta_{p0}}-\frac{1}{\eta_p}\right)+\left(\frac{k}{\eta_\infty}\right)\boldsymbol{\tau}_p:\mathbf{D}. \tag{2.41}$$

Here, the coefficient k/η_∞ is treated as a single parameter. This reformulation delivers continues extensional viscosity response.

- ***Non-dimensional form:*** In order to include this model within the local finite element/volume software library, expressing the system of equations in non-dimensional form is essential.

The governing equations in non-dimensional forms are expressed via length scale L (unit length), velocity scale U, time scale L/U, and pressure and extra-stress scale of $\mu U/L$. The parameter $\mu = \mu_s + \mu_p$ is the total viscosity. The non-dimensional parameters are defined as:

$$\mathbf{u}^* = \frac{\mathbf{u}}{U}, \quad t^* = \frac{U}{L}t, \quad \mathbf{D}^* = \frac{L}{U}\mathbf{D}, \quad p^* = \frac{p}{\left(\eta_{p0} + \eta_s\right)\frac{U}{L}}, \quad \tau_p^* = \frac{\tau_p}{\left(\eta_{p0} + \eta_s\right)\frac{U}{L}}. \tag{2.42}$$

For an incompressible and isothermal flow conditions, the relevant mass (Equation 2.2) and momentum (Equation 2.7) conservation equations may be expressed in dimensionless form (the * notation on dimensionless variable is omitted) as:

$$\nabla \cdot \mathbf{u} = 0, \tag{2.43}$$

$$Re\frac{\partial \mathbf{u}}{\partial t} = \nabla \cdot \mathbf{T} - Re\mathbf{u} \cdot \nabla \mathbf{u} - \nabla p. \tag{2.44}$$

Introducing the group numbers and dimensionless parameters Reynolds number (Re), Weissenberg number (We)[6] and solvent fraction (β) are given by,

$$Re = \rho\frac{UL}{\left(\eta_{p0} + \eta_s\right)}, \qquad We = \lambda_1\frac{U}{L}, \qquad \beta = \frac{\eta_s}{\left(\eta_{p0} + \eta_s\right)}, \tag{2.45}$$

[6] *We* notation is used here; note: this is frequently replaced by *Wi* to avoid confusion in wider CFD context with Weber Number.

Where the reference viscosity is taken as the zero shear-rate viscosity, so that $\frac{\eta_{p0}}{(\eta_{p0}+\eta_s)}+\frac{\eta_s}{(\eta_{p0}+\eta_s)}=1$. Here, η_s and η_{p0} are the solvent and zero-rate polymeric viscosity, respectively; and *We* governing elasticity is a function of the characteristic material relaxation time (λ_1).

A differential constitutive equation in general form (in dimensionless-form) may be expressed as [2.1],

$$We\frac{\partial \boldsymbol{\tau}_p}{\partial t}=2(1-\beta)\mathbf{D}-f\boldsymbol{\tau}_p-We\left(\mathbf{u}.\nabla\boldsymbol{\tau}_p-\nabla\mathbf{u}^T.\boldsymbol{\tau}_p-\boldsymbol{\tau}_p.\nabla\mathbf{u}\right). \tag{2.46}$$

Using the zero-rate polymeric viscosity as a scaling factor, the parameter f can be defined as $f=(\eta_{po}/\eta_p)$, then Equation (2.41) can be reorganize into that to determine f, as follows:

$$\frac{\partial f}{\partial t}=\frac{1}{\lambda_s}(1-f)+\left(\frac{k}{\eta_\infty}\right)\eta_{p0}\boldsymbol{\tau}_p:\mathbf{D}. \tag{2.47}$$

Once again, applying non-dimensionalisation, Equation (2.40) takes the general form of Equation (2.46) and Equation (2.47) now becomes,

$$\frac{\partial f}{\partial t}=\frac{1}{\omega}(1-f)+\xi_{\eta_{po}}\boldsymbol{\tau}_p:\mathbf{D}. \tag{2.48}$$

From Equation (2.48), the dimensionless parameters of structural construction ($\omega=\lambda_s U/L$) and destruction ($\xi_{\eta_{p0}}=(k/\eta_\infty)\eta_{p0}(\eta_{p0}+\eta_s)U/L$) in this micellar model appear in the equivalent terms for theses mechanism.

Material functions: The base set of parameters for the MBM model fluid used in this study are $\xi_{\eta_{p0}}$=0.1125 and ωsettings, corresponding to shear thinning properties with moderate hardening ($\omega=4.0$) and strong hardening ($\omega=0.28$) followed by

softening, using the reference value of β=1/9. In order to study the impact of the various model parameter in viscometric flows, apart from the base case, some variation in the construction parameter (ω) and destruction ($\xi_{\eta_{p0}}$) are also considered and presented in Figures 2.4 and 2.5, respectively.

The influence of variation in ω can be gathered from Figure 2.4. For shear viscosity, an increase in ω is reflected in a decrease of the shear-rate, affecting where the thinning starts. The levels of asymptotic plateaux are independent of this parameter. From $\omega = 0.1$ to 4.0, the final limiting value of the first normal stress difference (stress saturation) decreases by more than two decades and is attained at lower shear-rates. A similar increment in ω lowers the degree of strain-hardening, so that for the fluid with $\omega = 4.0$, η_e decreases rapidly, softening at much lower deformation rates.

Referring to Figure 2.5, the response of the model to a change in $\xi_{\eta_{p0}}$ somewhat replicates that dealt with under ω. It can be appreciated that the shear viscosity enters the thinning regime at lower deformations rates, and N_1 is decreased by about three decades when $\xi_{\eta_{p0}}$ varies from 0.001 to 0.1. An increase in $\xi_{\eta_{p0}}$ produces a considerable decrease in the degree of strain-hardening. Lower values of $\xi_{\eta_{p0}}$ are observed to generate larger peaks in extensional viscosity and steeper softening regimes.

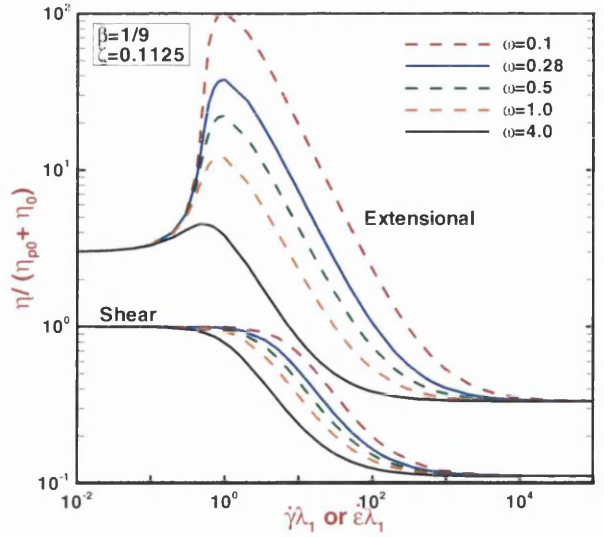

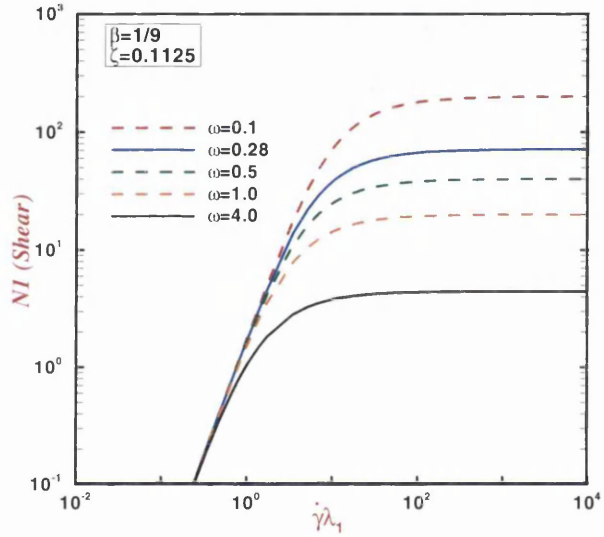

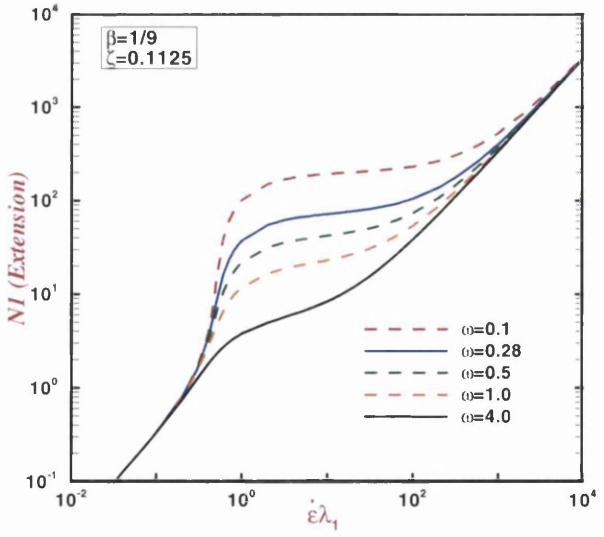

Figure 2.4. Shear and uniaxial extensional viscosities, including N_1 in shear and extension, variation with material parameter ω, (MBM model)

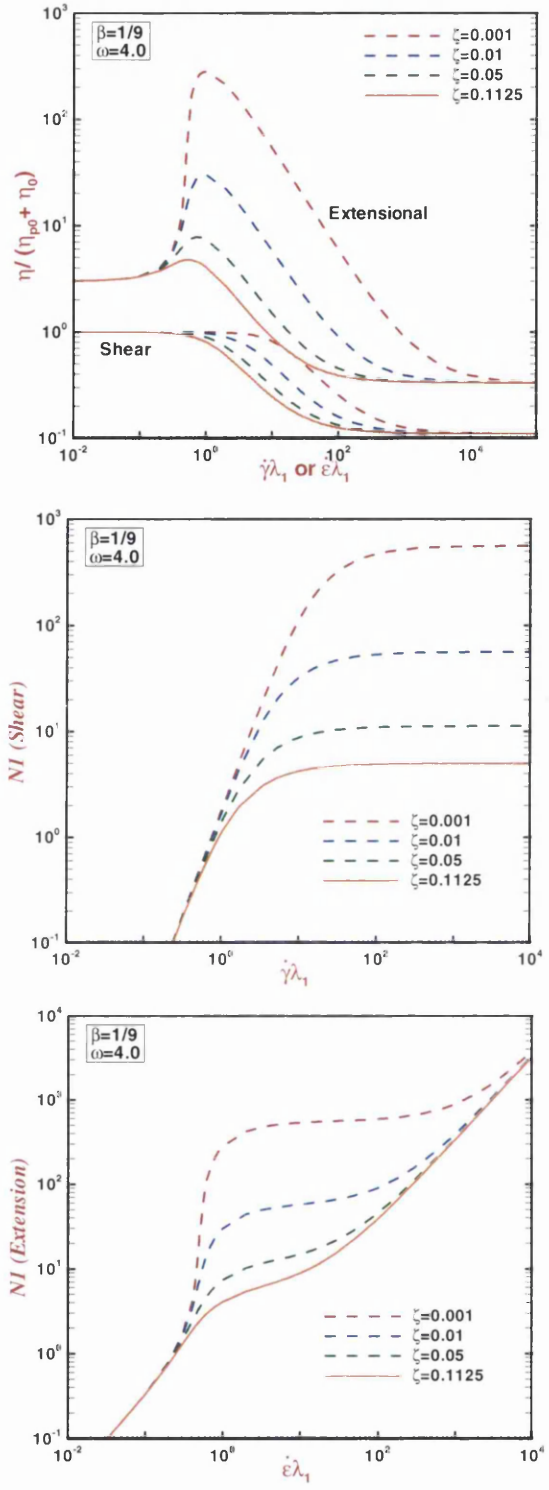

Figure 2.5. Shear and uniaxial extensional viscosities, including N_1 in shear and extension, variation with material parameter $\xi_{\eta_{p0}}$, (MBM model)

2.5 Rheometery

Rheometry is the science of the measurement of typical viscoelastic parameters (rheological properties) of materials of interest. Employing different types of rheometers, we are able to measure viscoelastic properties of a material as a function of either the applied stress or the applied strain (shear rate). Rheometers can be divided into two broad categories, according to their practical use: shear (rotational or oscillatory) rheometers, that conduct measurement under applied shear stress or strain; and extensional rheometers, that apply measurement under extensional stress or strain.The choice of a suitable rheometer depends on the particular rheological property to be determined.

2.5.1 Shear (Rotational/Oscillatory) Rheometers

Rotational Rheometry is one of the most widely used techniques for the measurement of complex shear rheological behaviour across wide range of materials from dilute polymer solutions to high modulus polymer melts. Several rheological properties of the sample can be characterised either by controlling motor torque (controlled shear stress) or position change (controlled shear deformation). Rotational instruments are most suited to low shear rates/low-frequency for investigating structural and compositional changes of materials via low stress/strain amplitude and associated tests such as yield stress analysis, stress relaxation, thixotropy, creep and creep recovery. This type of rheometer may be operationally functional under two different modes: the steady (constant angular velocity) mode to measure shear viscosity; and the unsteady (oscillatory) mode to determine dynamic material properties, such as viscoelastic modulus and phase angle.

Here, the emphasis is on oscillatory Controlled Shear Stress (CSS) type of rheometers. These devices investigate the structure or structural changes in materials by way of applying a harmonically time-varying sinusoidal oscillation. In order to

accurately determine the inherent rheological properties of a material, it is essential to ensure that the measurements are conducted in the Linear Viscoelastic (LVE) range, where the structural character of the sample is retained unaltered. Under dynamic testing, the evolution from linear to non-linear viscoelastic behaviour is dependent on strain amplitude. Thus, Small Amplitude Oscillatory Shear (SAOS) flow is one of the most common types of tests to determine the linear range for a specific material. At amplitudes higher than the material's critical strain, the structure of the sample has either already been changed irreversibly, or is even completely destroyed [2.15].

When using this type of rheometer, the sample is being sheared in a narrow gap of a measuring system (geometry), such as a cone-and-plate, parallel-plates or concentric cylinders; which are specifically designed to impose simple shear flow under rotation. There are advantages and disadvantages associated with each geometry. Figure 2.6 represents a schematic diagram of some typical flow geometries, such as cone-plate and parallel-plates shear rheometers. Here, the waveforms of the applied sinusoidal oscillating stress and resulting strain (input/output waves) are also presented, along with the phase lag between them (δ).

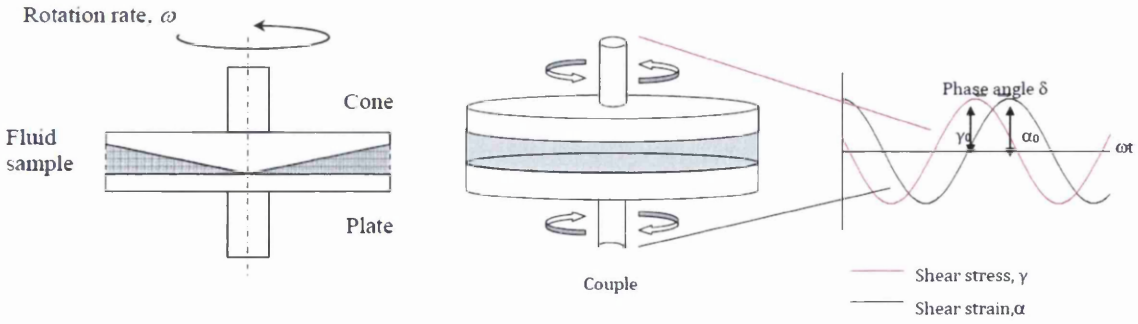

Figure 2.6. Schematic diagram of the typical flow geometry in shear rheometers and sinusoidal wave forms of stress and strain for viscoelastic material.

The subsequent deformation from a given stress will be determined by the properties of the material. The deformation may be reversible (recoverable) for purely elastic (Hookean solid) materials; or conversely irreversible (permanent) deformation for purely viscous (Newtonian fluid) materials; or, it may contain both a recoverable and a permanent part (viscoelastic material).

The geometry is attached to a spindle which is driven by a non-contact ultra-low inertia motor. The drive system is supported by a high quality air bearing which results in practically frictionless movement of the measuring system, coupled to an ultra-high precision position encoder. Both, the sample and measuring system are temperature controlled. A typical shear rheometer is capable of producing two principal outputs, the torque and normal force, detected by its sensor on the torsion bar and the non-oscillating geometry, respectively. From these two outputs, a great number of material properties can be determined.

The viscoelastic moduli for a SAOS flow are: the *storage modulus* (G'), representing the elastic component, that is, the amount of energy stored in the material; and the *loss modulus* (G''), representing the viscous component, that is, the amount of energy dissipated in the deformation, defined as [2.16]:

$$G'(\omega) \equiv \frac{\tau_0}{\gamma_0}\cos\delta\,, \tag{2.49}$$

$$G''(\omega) \equiv \frac{\tau_0}{\gamma_0}\sin\delta\,, \tag{2.50}$$

Where τ_0 is the maximum stress amplitude (Pa), γ_0 is the maximum strain amplitude, and ω is the angular frequency (rad/s). Here, δ (phase angle) gives the phase difference between the imposed shear stress wave and a corresponding strain wave response. For a Hookean solid, this phase angle is 0^o ($\delta=0^o$); in counter position, a Newtonian fluid has a phase angle of 90^o ($\delta=90^o$). For a viscoelastic substance, the viscoelasticity displays itself as a phase lag between 0 and 90 degrees

($0^o < \delta < 90^o$) (see Figure 2.6). By definition the loss factor, the relation between the both viscoelastic moduli, is given by:

$$\tan\delta = \frac{G''}{G'} \tag{2.51}$$

In principle, the loss and storage moduli provide a degree of the in- and out-of phase portions of the response to the imposed wave. The moduli and frequency relationship may be expressed in terms of the dynamic complex viscosity (η^*), which is a function of the frequency and consists of the viscous and elastic parts:

$$|\eta^*| = \sqrt{\left(\eta'^2 + \eta''^2\right)} = \sqrt{\left[\left(\frac{G'}{\omega}\right)^2 + \left(\frac{G''}{\omega}\right)^2\right]} = \frac{|G^*|}{\omega}, \tag{2.52}$$

In general, SAOS tests provide highly useful rheological characterization of complex fluids. Data of most significance resulting from these SAOS tests are complex viscosity (η^*), phase angle (δ), storage and loss modulus (G' & G''), as a function of frequency (ω), (Figure 2.7). Some typical isothermal frequency sweep test results are provided in Figure 2.7; (extend - very short/long time scale). In the derived results, the limiting (plateau) value of viscosity at low frequency is representative of a zero shear viscosity of a material. Moreover, these results convey information about the molecular weight distribution MWD (cross-over modulus, $G'=G''$) besides average molecular weight AWM (cross-over frequency), Figure 2.8. Here, the notation of positive/negative MWD are assigned to broad and narrow MWD, and positive/negative AMW are allocated to high and low AMW polymers. When measurements are made as a function of temperature, the phase angle (δ) can be a good indicator of phase transitions.

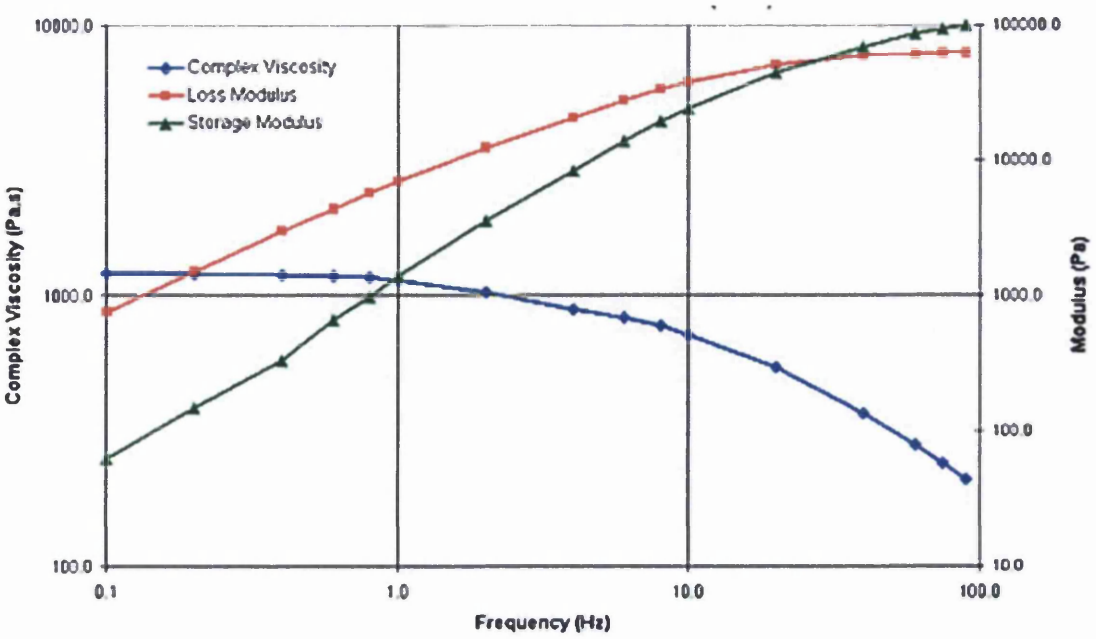

Figure 2.7. Typical isothermal frequency sweep test.

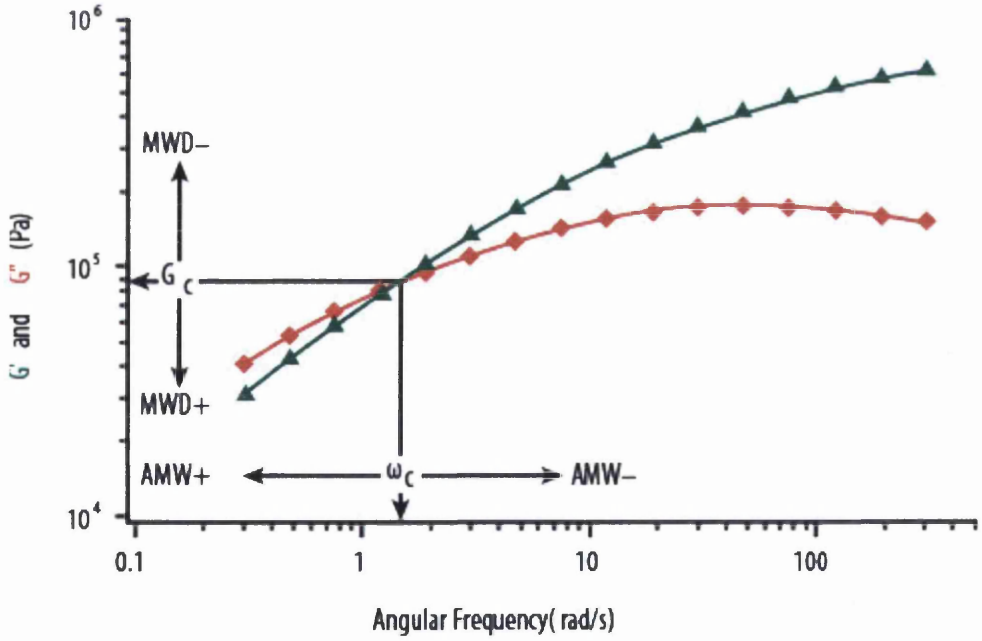

Figure 2.8. Dynamic moduli vs. frequency curves from SAOS test.

The resulting characterisations of material structure is ideal for observing individual changes in material structure and can be used for particular batch-to-batch inconsistency in pre-process quality control testing of bought-in materials.

Simple steady shear testing is the most common type of test for the majority of industrial applications. These types of tests are performed by subjecting a material to a constant shear stress or shear-rate and measuring the resistance to flow, resulting in the determination of a viscosity measure. The cone-and-plate is more desirable than other geometries for characterising a viscous fluid, due to its capacity to produce a viscometric flow, where the shear stress and shear rate are radially constant and uniform throughout the sample during the test.

2.5.2 Extensional (FiSER/CaBER) Rheometers

For some particular fluids and specific aspects of fluid behaviour under designated applications, it is often valuable to study a material under extensional flow. It is well known that, by adding of a slight amount of high molecular-weight polymer to a solution, the extensional flow resistance of the fluid can be significantly enlarged. Thus, the response of a viscoelastic fluid to an extensional flow can be considerably different from its shear response [2.17]. There are some typical industrially processes in which this is the case and for which the polymeric materials undergo a strong extensional/elongational mode of deformation, such as under film blowing and extrusion; and in applications, for instance in coating and enhanced oil recovery. For this reason, extensional rheology is a prime subject of interest and has advanced considerably in its achievements within the complex fluids community. There are a number of approaches of constructing an extensional flow, such as opposed jet device and certain contraction-expansion flows. Unfortunately, most of these devices have drawbacks due to the challenges associated with generating a homogeneous flow, transient measurements, and unknown strain history. Presently, the filament-stretching technique has been recognized as an accurate and reproducible method for imposing a homogeneous and uniaxial extensional flow [2.18]. Under filament-stretching considerations, the filament stretching rheometer

[2.19-2.25] has emerged as a favourable apparatus for measuring the extensional properties of highly-mobile low-medium viscosity fluids. A schematic diagram of a fluid within a filament stretching rheometer is shown in Figure 2.9. Here, typical filament samples may vary in length (nano, micro, macro) and loading (length/breath).

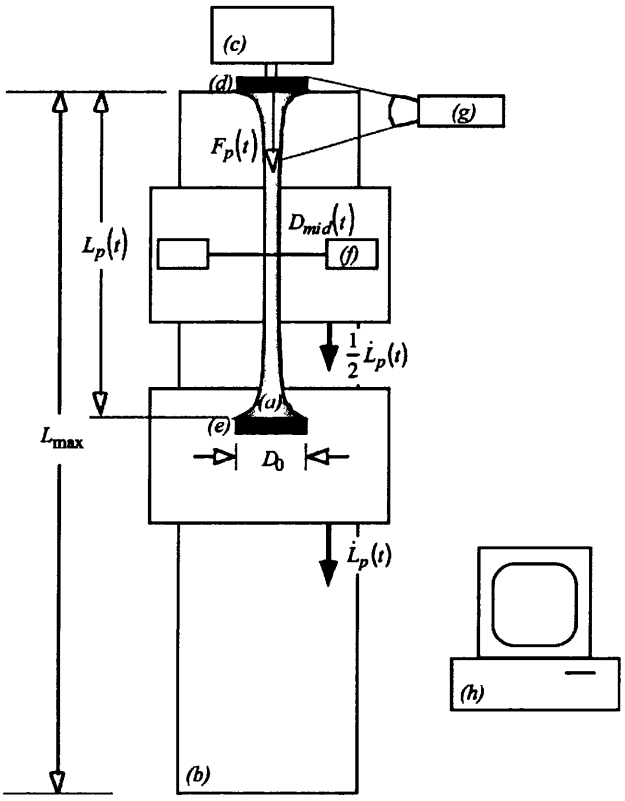

Figure 2.9. Schematic diagram of a filament-stretching instrument (Reproduced from [2.18]).

In a typical filament-stretching device, a cylindrical liquid bridge is initially placed between two flat circular end-plates. Then, one or both plates are retracted under a controlled synchronous motion to a specific time/length. Subsequent necking leads to significant thinning and reduction in the central region of the liquid bridge, whilst end-effects result in considerable shearing within the near end-plate zone (filament-foot). A comprehensive overview of filament stretching technology is

provided by McKinley and Sridhar [2.19], covering the flow dynamics within filament-stretching rheometers for non-Newtonian fluids. Typically, the dynamic development of the mid-filament diameter is monitored during the process of necking and failure, from which the appropriate rheological calculations are performed (dynamic extensional viscosity, relaxation time). There are two main modes used in commercially available filament-stretching instruments: Filament Stretching Extensional Rheometer (*FiSER* mode), and Capillary Break-up Extensional Rheometer (*CaBER* mode). Under continuous stretching (*FiSER*-mode), common practice is to impose a predetermined velocity upon the fluid formed between the end-plates, either at a fixed exponential rate (providing constant extension rate) or under uniform contact velocity (giving variable extension rate). Under the constant extension rate scenario, the resulting deformation is expected to approach ideal uniaxial elongation at the filament center. In this mode, the time-scale is inversely proportional to the initial constant stretch-rate imposed on the moving-plates.

In step-strain mode (*CaBER*-mode), the filament stretching rheometer may be employed under capillary-breakup conditions (short initial stretch) [2.20, 2.21, 2.25]. *CaBER* trials impose a rapid axial step-strain of prescribed magnitude, and then allow the sample to relax and breakup under the action of capillary forces (fluid self-selecting time-scale). Commonly, this implies short initial stretched samples (user-controlled), and much shorter than under *FiSER*-mode (continuous stretching, imposed rate/time scale). The relaxation and decay of the necked sample is governed by the viscous, elastic, gravitational and capillary forces [2.26], and as with *FiSER*-procedures, the evolution of the mid-filament diameter is again monitored. Although the flows in these two types of filament-stretching rheometer differ, both devices generate, *a priori* a uniaxial extensional deformation – hence, accessing dynamic extensional viscosity.

Background theory that links evolution of filament mid-plane radius (R_{mid})(t) to rheometric functions, such as apparent extensional viscosity (μ_{app}), and principal

relaxation time (λ), requires the satisfaction of certain base assumptions. Here, in pure uniaxial extensional deformation, one seeks the formation of a cylindrical filament shape, persistent in symmetry about the mid-plane, on which constant state of stress/deformation-rate applies at any particular time. Then, during the thinning-down stress-growth process under *CaBER* trials, evolution of the filament mid-plane radius, $R_{mid}(t)$, can be measured and related to extensional viscosity. Hence, both such quantities are governed by a force balance on the filament, determined through viscous, elastic and capillary forces. The extensional viscosity may be expressed dimensionally as [2.27],

$$\mu_{app} = \frac{-\chi}{2(dR_{mid}/dt)}, \tag{2.53}$$

where centre-plane extension-rate for a slender filament may be interpreted through the evolution of filament radius, $R_{mid}(t)$, as [2.21].

$$\dot{\varepsilon}(t) = -\frac{2}{R_{mid}}\frac{dR_{mid}(t)}{dt}, \tag{2.54}$$

The force balance on the filament and related equations used with these types of rheometers shall be reported in chapter 6.

References

[2.1] H.A. Barnes, J.F. Hutton, K. Walters, *An Introduction to Rheology*, Elsevier, (1989).

[2.2] R. Sizaire, *keyFE2 User Manual*, (2004).

[2.3] B. Puangkird, *Numerical Simulation of Complex Viscoelastic Flows*. In: Computer Science, Vol. Philosophiae Doctor, University of Wales, Swansea, Swansea, U.K., 2007, p. 28.

[2.4] D.M. Jones, K. Walters, P.R. Williams, *On the extensional viscosity of mobile polymer solutions*, Rheological Acta **26** (1987) 20-30.

[2.5] M.G.N. Perera, K. Walters, *Long-range memory effects in flows involving abrupt changes in geometry. Part I. Flows sssociated with L-shaped and T-shaped geometries*, J. Non-Newtonian Fluid Mech. **2** (1977) 49-81.

[2.6] J.C. Maxwell, *On the dynamical theory of gases*, Philosophical Transactions of the Royal Society A **157** (1867) 49-88.

[2.7] J.G. Oldroyd, *On the formation of rheological equations of state*, roceedings of the Royal Society of London. Series A **200** (1950) 523–541.

[2.8] N. Phan-Thien, *A nonlinear network viscoelastic model*, Journal of Rheology **22** (1978) 259-283.

[2.9] N. Phan-Thien and R.I. Tanner, *A new constitutive equation derived from network theory*, J. Non-Newtonian Fluid Mech. **2** (1977) 353- 365.

[2.10] T.C.B. McLeish, R.G. Larson, *Molecular constitutive equations for a class of branched polymers: The pom-pom polymer*, Journal of Rheology **42** (1998) 81-110.

[2.11] W.M.H. Verbeeten, *Computational polymer melts rheology*, Ph.D. Thesis, Technische Universiteit Eindhoven, (2001).

[2.12] W.M.H. Verbeeten, G.W.M. Peters and F.P.T. Baaijens, *Differential constitutive equations for polymer melts: The extended Pom-Pom model* Journal of Rheology **45** (2001) 1489-1489.

[2.13] O. Manero, F. Bautista, J.F.A. Soltero, J.E. Puig, *Dynamics of worm-like micelles: the Cox-Merz rule*, J. Non-Newtonian Fluid Mech. **106** (2002) 1-15.

[2.14] E.S. Boek, J.T. Padding, V.J. Anderson, P.M.J. Tardy, J.P. Crawshaw, J.R.A. Pearson, *Constitutive equations for extensional flow of wormlike micelles:*

stability analysis of the Bautista-Manero model, J. Non-Newtonian Fluid Mech. **126** (2005) 39-46.

[2.15] T.G. Mezger, *The Rheology Handbook: for users of rotational and oscillatory rheometers*, Vincentz Network, Hannover (2006).

[2.16] F.A. Morrison, *Understanding Rheology*. Oxford University Press, New York (2001).

[2.17] J.P. Rothstein and G.H. McKinley, *Inhomogeneous transient uniaxial extensional rheometry*. Journal of Rheology **46** (2002) 1419-1443.

[2.18] S.L. Anna, G.H. McKinley, D.A. Nguyen, T. Sridhar, S.J. Muller, J. Huang and D.F. James, *An interlaboratory comparison of measurements from filament-stretching rheometers using common test fluids.* Journal of Rheology **45** (2001) 83-114.

[2.19] G.H. Mckinley, T. Sridhar, *Filament-stretching rheometry of complex fluids*, Annu. Rev. Fluid Mech. **34** (2003) 375–415.

[2.20] J. Eggers, *Nonlinear dynamics and breakup of free-surface flows*, Rev. Mod. Phys. **69** (1997) 865.

[2.21] S.L. Anna and G.H. McKinley, *Elasto-capillary thinning and breakup of model elastic liquids*, J. Rheol. **45** (2001) 115–138.

[2.22] M. Yao, G.H. McKinley, B. Debbaut, *Extensional deformation, stress relaxation and necking failure of viscoelastic filaments*, J. Non-Newtonian Fluid Mech. **79** (1998) 469-501. doi:10.1016/S0377-0257(98)00116-5.

[2.23] M. Yao, G.H. McKinley, *Numerical simulation of extensional deformations of viscoelastic liquid bridges in filament stretching devices*, J. Non-Newtonian Fluid Mech. **74** (1998) 47–88. doi:10.1016/S0377-0257(97)00052-9.

[2.24] M. Yao, S.H. Spiegelberg, G.H. McKinley, *Dynamics of weakly strain-hardening fluids in filament stretching devices*, J. Non-Newtonian Fluid Mech. **89** (2000) doi:10.1016/S0377-0257(99)00028-2.

[2.25] A. Bhardwaj, E. Miller, J.P. Rothstein, *Filament stretching and capillary breakup extensional rheometry measurements of viscoelastic wormlike micelle solutions*, J. Rheol. (N. Y. N. Y). **51** (2007) 693. doi:10.1122/1.2718974.

[2.26] V.M. Entov, E.J. Hinch, *Effect of a spectrum of relaxation times on the capillary thinning of a filament of elastic liquid*, J. Non-Newtonian Fluid Mech. **72** (1997) 31–53.

[2.27] G.H. Mckinley, *Visco-Elasto-Capillary thinning and break-up of complex fluids*, Rheol. Rev. (2005) 1–48. doi: 10.1007/s00247-009-1482-4.

All exact science is dominated by the idea of approximation.

Bertrand Russell

Chapter 3

Numerical Algorithms

The present study has benefited from a hybrid numerical procedure comprising of a finite element (FE) method for both the momentum and continuity equations, along with the finite volume (FV) method for the constitutive law. These methods have been employed separately and with success for a range of different computational fluid dynamics (CFD) problems. The implementation of this hybrid method takes advantages of many features of both algorithms, and results in a stable high-order finite element/finite volume (*fe/fv*) scheme.

3.1 Introduction

Modern developments in computer programming has played a vital role in bringing about a significant improvement in the capability of numerical modelling. Now, and due to this devolvement, only a relatively short time is needed to find a solution to a physical system which consists of several sets of governing equations. So far, modelling physical problems with CFD, has evolved through three principal numerical methods, and which have been employed successfully on a range of fluid flow problems. The physical domains to which these numerical methods have been applied involve both simple and complex fluid flow. Typically, these methods are: finite difference, finite element and finite volume schemes, respectively. For more information on viscoelastic flows the reader is referred to [3.1-3.3]. In addition, these methods had been used to analyse a variety of constitutive laws for stress.

The finite difference method is one of the most widely used numerical techniques for solving differential equations. It is a relatively simple technique to use for simple rectangular-type domains. Complications arise when dealing with complex geometries and boundary conditions, which are generally to be avoided. This is because this technique could lead to inaccurate results and produce complicated discretisation schemes. In such instances, this technique necessitates the need for conformal mapping. The use of FE and the FV methods are commonly suggested for non-uniform grids. This in turn will allow simulating non-simple flow geometries comprising a reduced number of equations in comparison to standard finite difference schemes.

The FE and FV method are known to result in the same type of algorithm. Both methods dictate that the physical problem domain be divided into a non-overlapping finite number of sub-domains. The equations to be modelled are then used over each finite element or finite volume cell. Thereafter variable solution unknowns are approximated by interpolation ('shape' or 'trial') functions that are themselves dependent on nodal values over these physical sub-domains. For this purpose, in FE

and FV methods, low order polynomials are customary to use. A system of algebraic equations, in which the nodal solution of unknowns is sought, emerges once these equations are integrated over the known physical domain, whereupon weighting ('test') functions are introduced within the integrand.

A combination of FE and FV methods are involved in forming the computational procedures of the hybrid scheme used for the present study. To solve the momentum equation a finite element approach is used. The approach was based on a time discretisation via a semi-implicit formulation on a Taylor-Galerkin procedure. A three-staged algorithm results when incompressibility is enforced through a fractional-staged procedure commonly termed pressure-correction. For spatial discretisation of the constitutive equation a subcell cell-vertex FV technique is used, however. The finite volume grid is formed via a partition of each finite element triangle by connecting the mid-side nodes of that element. Accuracy is achieved through a consistent treatment of the flux and source terms of the constitutive equation. Flux and source residuals are distributed to the vertices of each finite volume control cell through the use of fluctuation distribution (FD) schemes. Stability in terms of high Weissenberg number attainment is improved by the use of a median-dual-cell (MDC) approach for evaluation of flux and source terms.

The basis of the finite element implementation used in this thesis is the Taylor-Galerkin/pressure-correction (TGPC) algorithm, first proposed by Townsend and Webster [3.4] to simulate the flow of viscous and viscoelastic fluids. The main idea is to solve the hyperbolic-type constitutive equation with an algorithm suitable for the task. Since the FV method has often been found superior to the FE method for this purpose, due to its particular inherent properties, the present hybrid finite element/finite volume algorithm has appeared. Donea [3.5] was the first to work on Taylor-Galerkin schemes for convection-diffusion problems, with implementations based upon Euler, leapfrog and Crank-Nicolson time-stepping procedures. Temam [3.6] and Chorin [3.7] proposed the earliest forms of pressure-correction schemes (projection methods) for viscous incompressible flows. Second-order pressure-

correction versions were introduced by van Kan [3.8], through a finite difference discretisation and Crank-Nicolson time-splitting. The combination of these ideas under FE discretisation is the basis of the numerical algorithm proposed by Townsend and Webster [3.4]. Hawken et al. [3.9] improved the proposed initial explicit time-discretisation, advancing to a semi-implicit form for viscous flows, overcoming viscous stability restrictions. Subsequently, Carew et al. [3.10] and Baloch et al. [3.11] advanced such a semi-implicit implementation to address viscoelastic flow problems.

The main features of the Galerkin finite element (see 3.12-3.14), are discussed below. In addition to this, an outline of the finite volume [3.15, 3.16] technique is considered.

3.1.1 The Galerkin Finite Element Method

The application of the finite element method involves dividing the spatial geometry (physical domain) into a set of finite elements, known as mesh (tessellation), where the solution of the problem is sought. For practical flow problems, the geometric domain under consideration may be either a simple or a complex one. For instance, consider the following time independent Poisson equation,

$$\frac{\partial^2 u}{\partial x^2} = f(x). \tag{3.1}$$

Here, a polynomial, usually of first or second order, is used to interpolate the unknown variables by appropriate functions. The resulting residuals are weighted and then integrated over the individual elements, the sum of which contribute to the complete problem discrete representation.

$$u(x) = \sum_{i}^{nt} \phi_i(x) u_i, \tag{3.2}$$

In equation (3.2), nt stands for the total number of nodes in a given element, $\phi_i(x)$ is the trial functions and u_i, the unknown solution nodal values. With $w_j(x)$ weighting functions, substitution of (3.2) in (3.1) yields:

$$\int_{\Omega_e} \frac{\partial^2}{\partial x^2}\left[\phi_i(x)u_i\right] w_j(x)\,\mathrm{d}\Omega_e = \int_{\Omega_e} f(x)\,w_j(x)\,\mathrm{d}\Omega_e. \tag{3.3}$$

As far as the Galerkin method is concerned, weighting (test) functions are selected from the same space of functions as the trial functions, which is denoted by $w_j(x) = \phi_j(x)$. Upon integrating by parts (using the Green-Gauss Theorem),

$$\left.\frac{\partial \phi_{i(x)}}{\partial x}\phi_{j(x)}\right|_{\Gamma_e} - u_i \int_{\Omega_e} \frac{\partial \phi_{i(x)}}{\partial x}\frac{\partial \phi_{j(x)}}{\partial x}\,\mathrm{d}\Omega_e = \int_{\Omega_e} f_{(x)}\phi_{j(x)}\,\mathrm{d}\Omega_e. \tag{3.4}$$

The system over the domain $\Omega = \Sigma_e \Omega_e$ is made up of all such elemental contributions and/or meshes. The boundary contribution term, evaluated over the boundary (Γ_e) of the element, generally cancels out over interior elements, assuming sufficient smoothness of representation. When solution values are known (Dirichet conditions) at the outer domain boundary, this is imposed on the 'trial solution' and then 'test functions' vanish there. In the present study, this strategy is largely followed for the velocity which is imposed on most boundaries.

The full system of equations, in matrix notation, emerging from equation (3.4) can be expressed as:

$$\mathbf{K}\,\mathbf{u} = \mathbf{b}, \tag{3.5}$$

the column-matrix $\mathbf{u}$ contains the nodal values, where $\mathbf{K}$ and $\mathbf{b}$ are defined as,

$$K_{ij} = \int_{\Omega} \frac{\partial \phi_i(x)}{\partial x}\frac{\partial \phi_j(x)}{\partial x}\,\mathrm{d}\Omega, \qquad b_j = \int_{\Omega} f(x)\phi_j(x)\,\mathrm{d}\Omega, \tag{3.6}$$

which can be evaluated either analytically or numerically. Analytical evaluation is available for many standard integrand and domain types, such as polynomial on simplex domains. The summation of all individual elements into a complete system must introduce the specified boundary conditions. For instance, as known values of the solution (Dirichlet conditions) are imposed in this example, nodal values on the sides of the domain (boundary Γ) are then specified. These can be substituted directly into the corresponding equation positions (within rhs terms $\mathbf{b}$), and hence, eliminated from $\mathbf{u}$. Matrix algebra is used to solve equations such as (3.5). Algebraic procedures used here may be either of a direct and/or iterative nature; the decision between which, highly depends on the conditioning of the system, the number of elements/nodes and the complexity of the shape functions.

3.1.2 The Finite Volume Method

The Finite Volume technique again uses an integral representation of the system of equations to seek a solution to the differential equations describing any particular physical problem behaviour. A similar treatment to that above is used for the differential constitutive model, and which is integrated over the *fv*-subdomain. This is typically a subclass of the finite element procedure with weighting functions set to unity, $w(x)=1$. A general conservation law for quantity ς is considered here:

$$\frac{\partial}{\partial t}\int_{\Omega}\varsigma\,\mathrm{d}\Omega+\int_{\Gamma}\mathbf{f}\cdot\mathbf{n}\,\mathrm{d}\Gamma=\int_{\Omega}\mathbf{q}\,\mathrm{d}\Omega, \tag{3.7}$$

where ς is a conservative quantity such as mass, momentum or energy, $\mathbf{f}$ is the flux of this quantity (which can be determined separately in convective and diffusive parts), $\mathbf{n}$ is an outward unit vector normal to the surface Γ which encompass the

volume Ω, and $\mathbf{q}$, comprises the source terms and/or body forces. Considering the classical cell-centred FV-approximation[1], mean values in a *fv*-cell are defined as:

$$\varsigma_i = \frac{1}{|\Omega_i|}\int_{\Omega_i} \varsigma \, d\Omega_i, \tag{3.8}$$

Upon applying (3.7) on a single finite volume, having mean values ς_i and q_i, one may extract the following relation:

$$\frac{\partial}{\partial t}\varsigma_i + \frac{1}{|\Omega_i|}\sum_k \int_{\Gamma_k} \mathbf{f}\cdot\mathbf{n}_k d\Gamma_k = q_i, \tag{3.9}$$

where k is the number of 'faces' of the *fv*-subcell and Γ_k is the area of those faces. One of the advantages of the FV method, as compared to other methods, is the fact that the variables in integral form are intrinsically conserved over the entire domain and also on the individual *fv*-cell. On applying numerical integration, the mean values can be approximated,

$$\int_{\Omega_i} \varsigma(x)\, d\Omega_i \approx \sum_{i=0}^{nc} \varphi_i \varsigma_i(x), \tag{3.10}$$

where $\varphi_i \geq 0$ are weights, and nc is the number of nodes of the numerical integration. Surface integrals are calculated as:

$$\int_{\Gamma_k} \mathbf{f}\cdot\mathbf{n}_k d\Gamma_k \approx \sum_k F_k, \tag{3.11}$$

[1] One must note that here, cell-vertex FV approximation is used on triangular cells

In relation (3.11), F_k is an approximation of $\mathbf{f}\cdot\mathbf{n}_k$ and as already mentioned, k is the number of faces of the *fv*-cell.

The discretised form of equation (3.7) is made up of the summation of all such approximations over each finite volume cell in representing the total domain. Consequently, a system of algebraic equations can be generated for which the solution is sought, in a manner similar to that above. One notes that a distinct advantage of the FV discretisation is the efficient and direct solution available (equivalent to an explicit FE time-discretisation).

3.2 Problem Specification

A physical model for the isothermal incompressible flow of a viscoelastic fluid, having no volumetric forces, is defined by the following governing system of equations,

$$\nabla\cdot\mathbf{u}=0,$$

$$Re\left(\frac{\partial\mathbf{u}}{\partial t}+\mathbf{u}\cdot\nabla\mathbf{u}\right)=-\nabla p+\nabla\cdot\boldsymbol{\tau}+\beta\nabla^2\mathbf{u}.$$

In addition to this system of governing equations, a constitutive equation must be introduced in order to incorporate the stress-behaviour of a particular fluid. The non-dimensional form of the Oldroyd-B model is,

$$We\overset{\nabla}{\boldsymbol{\tau}}+\boldsymbol{\tau}=2(1-\beta)\mathbf{D}. \tag{3.12}$$

where (β) is equivalent to the solvent viscosity, $(1-\beta)$ is a polymeric viscosity contribution and $\mathbf{D}$ is the rate of deformation tensor. Also, the non-dimensional quantities $Re=\frac{\rho U\ell}{\mu}$, $We=\frac{\lambda U}{\ell}$ are Reynolds number and Weissenberg number, respectively (refer to Chapter 2). If other models are specified, then {3.12} is replaced by the selected model equations.

In order to correctly specify the flow problem in question, one must apply appropriate boundary and initial conditions. Generally, the boundary conditions may be of mixed forms,

$$\mathbf{u}_{\Gamma_1} = \mathbf{g}_1, \qquad (\boldsymbol{\sigma}\cdot\mathbf{n})_{\Gamma_2} = \mathbf{g}_2, \qquad \boldsymbol{\tau}_{\Gamma_3} = \mathbf{g}_3, \tag{3.13}$$

where $\Gamma_{k=1,2,3}$ are non-overlapping subsections of the boundary Γ encompassing the domain Ω, $\boldsymbol{\sigma}$ is the Cauchy stress and $\mathbf{n}$ is the outward unit normal vector to the boundary. In the present study, a two-dimensional flow is used for the analysis. Moreover, no-slip conditions applied at the boundary-walls. To satisfy fully-developed flow conditions, imposing velocity profiles of the Oldroyd-B model, sufficiently large inlet/outlet channel section must be established. Additionally, inlet stress conditions must be imposed as well.

Simulation at low elasticity levels (usually $We = 0.1$) begins from some initial state in all the variables, usually assumed as at rest. Subsequently, an increase in We number is introduced to advance to higher levels of elasticity. Upon using the solution at the previous level as the initial condition for the next We-step. These initial conditions can be expressed as:

$$\mathbf{u}_{(\mathbf{x},t_0)} = \mathbf{u}^0{}_{(\mathbf{x})}, \qquad \nabla\cdot\mathbf{u}^0 = 0, \qquad \mathbf{T}_{(\mathbf{x},t_0)} = \mathbf{T}^0{}_{(\mathbf{x})}, \tag{3.14}$$

Here, the superscript "0" specifies estimation at time $t = t_0$.

3.3 Time Discretisation

Taylor series expansion is the basis of the time-stepping procedure. Through a two-step Lax-Wendroff approach, accuracy may be improved. This may be elucidated by considering a one-dimensional problem,

$$\frac{\partial u}{\partial t} + \frac{\partial}{\partial x} f(u) = 0. \tag{3.15}$$

Here, x and t are independent spatial/temporal variables, and $u(x,t)$ is a scalar field dependent solution variable. u^{n+1} and u^n are function of the u at time levels t_{n+1} and t_n, respectively.

The two-step Lax-Wendroff procedure, over time-step $t \in \left[t_n, t_{n+\frac{1}{2}}\right]$ and $t \in \left[t_n, t_{n+1}\right]$, is given by:

$$u^{n+\frac{1}{2}} = u^n + \tfrac{1}{2}\Delta t\left[-\frac{\partial}{\partial x} f(u)\right]^n, \tag{3.16}$$

$$u^{n+1} = u^n + \tfrac{1}{2}\Delta t\left[-\frac{\partial}{\partial x} f(u)\right]^{n+\frac{1}{2}}. \tag{3.17}$$

In these equations, and in the remainder of this chapter, the terms with n indicate evaluation at a specific time step.

Following van Kan's ideas [3.17], an approximation of $O(\Delta t^2)$ may be derived by applying these predictor-corrector-equations to the momentum equation in non-dimensional form, see equation (2.44)[‡]. This will provide,

. *Step* 1: $$\mathbf{u}^{n+\frac{1}{2}} - \mathbf{u}^n = \frac{\Delta t}{2\,Re}\left[\nabla\cdot(\boldsymbol{\tau} + 2\beta\mathbf{D}) - Re\,\mathbf{u}\cdot\nabla\mathbf{u} - \nabla p\right]^n, \tag{3.18}$$

. *Step* 2: $$\mathbf{u}^{n+1} - \mathbf{u}^n = \frac{\Delta t}{Re}\left[\nabla\cdot(\boldsymbol{\tau} + 2\beta\mathbf{D}) - Re\,\mathbf{u}\cdot\nabla\mathbf{u} - \nabla p\right]^{n+\frac{1}{2}}. \tag{3.19}$$

The pressure term ($\nabla p^{n+\frac{1}{2}}$) in equation (3.19) may be approximated by,

---

[‡] Equation (2.44) can also be expressed as $Re\left(\frac{\partial \mathbf{u}}{\partial t} + \mathbf{u}\cdot\nabla\mathbf{u}\right) = -\nabla p + \nabla\cdot(\boldsymbol{\tau} + 2\beta\,\mathbf{D})$.

$$p^{n+\frac{1}{2}} = \theta p^{n+1} + (1-\theta)\, p^{n}, \tag{3.20}$$

where $\left(p^{n+1} - p^{n}\right)$ represents the pressure difference on a single time-step $\left(t_{n+1} - t_{n}\right) = \Delta t$. For the explicit scheme, the weighting parameter is set to $\theta = \frac{1}{2}$ (Crank-Nicolson) the temporal discretisation error is $O\left(\Delta t^{2}\right)$; otherwise, the error is $O\left(\Delta t\right)$. Equation (3.19) can be re-written in the form,

$$\mathbf{u}^{n+1} - \mathbf{u}^{n} = \frac{\Delta t}{Re}\left[\left(\nabla \cdot [\boldsymbol{\tau} + 2\beta\mathbf{D}] - Re\,\mathbf{u}\cdot\nabla\mathbf{u}\right)^{n+\frac{1}{2}} - \theta\nabla p^{n+1} - (1-\theta)\nabla p^{n}\right]. \tag{3.21}$$

In order to implement the incompressibility constraint of equation (2.43), a supplementary variable $\mathbf{u}^{*}$ may be introduced, which is non-divergence free velocity (non-solenoidal), satisfying relation (3.22):

$$\mathbf{u}^{*} = \mathbf{u}^{n} + \frac{\Delta t}{Re}\left[\left(\nabla \cdot [\boldsymbol{\tau} + 2\beta\mathbf{D}] - Re\,\mathbf{u}\cdot\nabla\mathbf{u}\right)^{n+\frac{1}{2}} - \nabla p^{n}\right]. \tag{3.22}$$

Subtracting (3.21) from (3.22), the velocity at the proceeding time-step becomes:

$$\mathbf{u}^{n+1} = \mathbf{u}^{*} + \theta\frac{\Delta t}{Re}\nabla\left(p^{n+1} - p^{n}\right). \tag{3.23}$$

Taking the divergence of $\mathbf{u}^{n+1}$ and applying continuity, the pressure increment on the time-step may be obtained through the divergence of,

$$\nabla^{2}\left(p^{n+1} - p^{n}\right) = \frac{Re}{\theta\Delta t}\nabla\cdot\mathbf{u}^{*}, \tag{3.24}$$

Therefore, this pressure-correction scheme embodies a multiple-time fractional-staged method, where stage 1 {Equation 3.22} introduces a non-divergence free velocity term $\mathbf{u}^{*}$ for velocity, and pressure at stage 2 {Equation 3.24} solves directly

for pressure difference $\left(p^{n+1}-p^{n}\right)$, whilst stage 3 {Equation 3.23} corrects the velocity $\mathbf{u}^{n+1}$, to a divergence-free end of time-step velocity.

The Taylor-Galerkin pressure-correction algorithm embraces velocity, pressure and stress equations in the governing system of equations through the following fractional stages:

- ***Stage 1a:***

$$\frac{2\,Re}{\Delta t}\left[\mathbf{u}^{n+\frac{1}{2}}-\mathbf{u}^{n}\right]=\left(\left(\nabla\cdot\mathbf{T}-Re\,\mathbf{u}\cdot\nabla\mathbf{u}\right)^{n}+\nabla p^{n}\right), \tag{3.25}$$

$$\frac{2\,We}{\Delta t}\left[\boldsymbol{\tau}^{n+\frac{1}{2}}-\boldsymbol{\tau}^{n}\right]=\left(f\boldsymbol{\tau}+We\left(\mathbf{u}\cdot\nabla\boldsymbol{\tau}-\boldsymbol{\tau}\cdot\nabla\mathbf{u}-\boldsymbol{\tau}.\left(\nabla\mathbf{u}\right)^{\mathrm{T}}\right)-2\left[1-\beta\right]\mathbf{D}\right)^{n}, \tag{3.26}$$

- ***Stage 1b:***

$$\frac{Re}{\Delta t}\left(\mathbf{u}^{*}-\mathbf{u}^{n}\right)=\left(\left(\nabla\cdot\mathbf{T}-Re\,\mathbf{u}\cdot\nabla\mathbf{u}\right)^{n+\frac{1}{2}}-\nabla p^{n}\right), \tag{3.27}$$

$$\frac{We}{\Delta t}\left[\boldsymbol{\tau}^{n+1}-\boldsymbol{\tau}^{n}\right]=\left(f\boldsymbol{\tau}+We\left(\mathbf{u}\cdot\nabla\boldsymbol{\tau}-\boldsymbol{\tau}\cdot\nabla\mathbf{u}-\boldsymbol{\tau}.\left(\nabla\mathbf{u}\right)^{\mathrm{T}}\right)-2\left[1-\beta\right]\mathbf{D}\right)^{n+\frac{1}{2}}, \tag{3.28}$$

- ***Stage 2:***

$$\nabla^{2}\left(p^{n+1}-p^{n}\right)=\frac{Re}{\theta_{2}\,\Delta t}\nabla\cdot\mathbf{u}^{*}. \tag{3.29}$$

- ***Stage 3:***

$$\frac{Re}{\theta\Delta t}\left(\mathbf{u}^{n+1}-\mathbf{u}^{*}\right)=\nabla\left(p^{n+1}-p^{n}\right). \tag{3.30}$$

Stage 1 in this three-stage structure solves the velocity and stress components of the momentum and constitutive equations at half time step $\left(n+\frac{1}{2}\right)$ from data obtained at time step (n). Note, the retention of a velocity gradient component here, introduces temporal differences in pressure across the stages and gives the scheme its second-order characteristics. Stage 2 uses the $\mathbf{u}^*$ on its right-hand side, via a Poisson equation over a full time step $(n,n+1)$ to solve the pressure difference $\left(p^{n+1}-p^n\right)$. Then, stage 3 corrects for the non-divergence free velocity field to gather $\mathbf{u}^{n+1}$, using $\mathbf{u}^*$ and $\left(p^{n+1}-p^n\right)$ data, applied through a Jacobi iteration method. These three-stages must be solved over each time-step, $\left[t^n,t^{n+1}\right]$ until temporal convergence is obtained in deriving a limiting steady-state solution.

3.4 Spatial Discretisation

In the present study, the numerical scheme employed is that from a class of hybrid methods. The spatial domain of the problem is discretised into a finite number of triangular elements. The velocity and extra-stress are computed at the vertex and mid-side nodes, and pressure at vertex nodes. In particular, spatial discretisation for velocity and pressure is performed through a Galerkin finite element method, whilst for the stress equation (3.26) and (3.28), a cell-vertex finite volume scheme is implemented.

3.4.1 Finite Element Scheme

In the finite element scheme, scalar velocity components and pressure fields are approximated by:

$$u(x,t)=\phi_j(x)\,U_j(t), \qquad p(x,t)=\psi_j(x)\,P_j(t), \tag{3.31}$$

where $U_j(t)$, $P_j(t)$ are nodal values of velocity and pressure; the set of shape functions $\phi_j(x)$ is that of piecewise quadratic basis functions for velocity, and $\psi_j(x)$ are linear basis functions for pressure. Triangular parent elements are used in the *fe*-implementation, with velocity calculated at vertex and mid-side nodes (6-nodes), and pressure only at vertex nodes (3-nodes). The exterior parent triangle in Figure 3.1a represents a typical finite element, indicating the information calculated at each node. The problem statement in fully-discrete matrix-vector form may be expressed as:

- ***Stage 1a***

$$\left(\frac{2\,Re}{\Delta t}\mathbf{M}+\tfrac{1}{2}\beta\mathbf{S}\right)\left[\mathbf{U}^{n+\frac{1}{2}}-\mathbf{U}^{n}\right]=\left(-\left[\beta\mathbf{S}+Re\,\mathbf{N}(\mathbf{U})\right]\mathbf{U}-\mathbf{BT}\right)^{n}+\mathbf{L}^{T}\mathbf{P}^{n}. \qquad (3.32)$$

- ***Stage 1b***

$$\left(\frac{Re}{\Delta t}\mathbf{M}+\tfrac{1}{2}\beta\mathbf{S}\right)\left[\mathbf{U}^{*}-\mathbf{U}^{n}\right]=\left(-\left[\beta\mathbf{S}+Re\,\mathbf{N}(\mathbf{U})\right]\mathbf{U}-\mathbf{BT}\right)^{n+\frac{1}{2}}+\mathbf{L}^{T}\mathbf{P}^{n}. \qquad (3.33)$$

- ***Stage 2***

$$\mathbf{K}\left(\mathbf{P}^{n+1}-\mathbf{P}^{n}\right)=-\frac{Re}{\theta_2\,\Delta t}\mathbf{L}\mathbf{U}^{*}. \qquad (3.34)$$

- ***Stage 3***

$$\frac{Re}{\Delta t}\mathbf{M}\left(\mathbf{U}^{n+1}-\mathbf{U}^{n}\right)=\tfrac{1}{2}\mathbf{L}^{T}\left(\mathbf{P}^{n+1}-\mathbf{P}^{n}\right). \qquad (3.35)$$

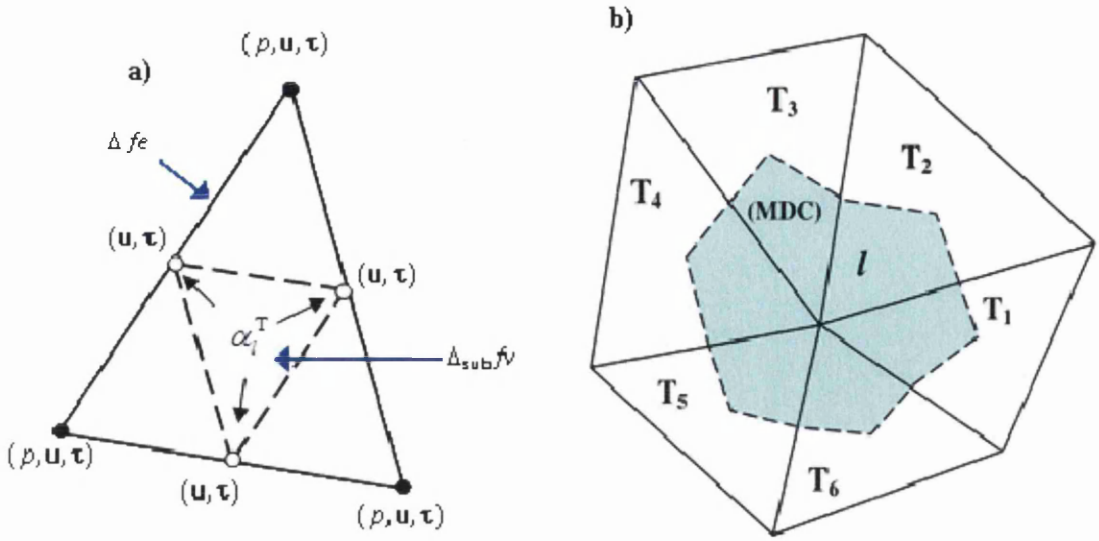

Figure 3.1. Spatial discretisation; a) *fe*-parent triangle with *fv*-subcells, b) *fv*-control volme for node *l*, with median-dual-cell configuration.

In equations (3.32) and (3.33) the weighting parameter θ_1 has been set to zero. $\mathbf{U}$, $\mathbf{T}$, and $\mathbf{P}$ are solution nodal vectors for velocity, stress and pressure. The weighting shape functions may be manipulated to give the matrix-vector terms,

$$M_{ij} = \int_{\Omega} \phi_i \phi_j \, \mathrm{d}\Omega, \qquad K_{ij} = \int_{\Omega} \frac{\partial \psi_i}{\partial x} \frac{\partial \psi_j}{\partial x} \mathrm{d}\Omega, \qquad S_{ij} = \int_{\Omega} \frac{\partial \phi_i}{\partial x} \frac{\partial \phi_j}{\partial x} \mathrm{d}\Omega,$$

$$B_{ij} = \int_{\Omega} \frac{\partial \phi_i}{\partial x} \phi_j \, \mathrm{d}\Omega, \qquad \left(L_k\right)_{ij} = \int_{\Omega} \psi_i \frac{\partial}{\partial x_k} \phi_j \, \mathrm{d}\Omega, \tag{3.36}$$

$$N_{ij}(\mathbf{U}) = \int_{\Omega} \phi_i \left(\phi_k \mathrm{U}_k \frac{\partial \phi_j}{\partial x} + \phi_k \mathrm{V}_k \frac{\partial \phi_j}{\partial y} + \phi_k \mathrm{W}_k \frac{\partial \phi_j}{\partial z} \right) \mathrm{d}\Omega,$$

3.4.2 Finite Volume Scheme

In order to represent flow problems with the FV method, an appropriate split of the flux ($\mathbf{R}$) and source ($\mathbf{Q}$) residuals must be made to the vertices of each *fv*-triangle. With cell-vertex methods, nodal variables are located at the vertices of the *fv*-cell. Values at any other position must be obtained by interpolation. In contrast, rates-of-changes (or fluctuation) of flow variables are integrated over each *fv*-cell (surface flux or volume integrals). This implies that fluctuation must be adequately distributed to the *fv*-cell vertices. The hybrid *fe/fv* algorithm employed in this study, utilizes fluctuation distribution (FD) procedures to achieve this.

The FV method mesh is generated by partitioning, at the midside nodes of each finite element (parent) triangle, into four triangular *fv*-subcells (see Figure 3.1a for clarification). The type of *fv*-algorithm employed is a *cell-vertex scheme*[2], which is employed to obtain values for stress at each node, similar to the treatment for velocity in the *fe*-scheme.

The constitutive model can be rewritten under the FV method implementation in terms of flux and source terms as,

$$\frac{\partial}{\partial t}\boldsymbol{\tau} = -\mathbf{R} + \mathbf{Q}, \tag{3.37}$$

with expressions for the flux ($\mathbf{R}$) and source ($\mathbf{Q}$) term, defined as,

$$\mathbf{R} = \mathbf{u}\cdot\nabla\boldsymbol{\tau}, \tag{3.38}$$

$$\mathbf{Q} = \frac{1}{We}\left(2[1-\beta]\mathbf{d} - \boldsymbol{\tau}\right) + \left(\nabla\mathbf{u}\right)^{\mathrm{T}}\cdot\boldsymbol{\tau} + \boldsymbol{\tau}\cdot\nabla\mathbf{u}. \tag{3.39}$$

---

[2] With its inherently superior accuracy of piecewise linear interpolation, over that of piecewise constant interpolation for cell-centred approximations, see [3.21-3.23].

Integration of equations (3.37)-(3.39) for each scalar component of the stress τ, yields the associated residuals. These must be evaluated over each full *fv*-cell and/or over its derived median-dual-cell (MDC), associated (Figure 3.1b) with each given node l. The MDC for any node is formed by taking the area constituting all nearest-neighbour points to that node, making up one third of each triangular cell containing that node,

$$\int_{\hat{\Omega}_l} \frac{\partial}{\partial t} \tau \, \mathrm{d}\Omega = -\int_{\Omega_T} R \, \mathrm{d}\Omega + \int_{\hat{\Omega}_l} Q \, \mathrm{d}\Omega . \tag{3.40}$$

Time discretisation is shown in equations (3.26) and (3.28), ***stages 1a*** and ***1b***, respectively. The proportion of contribution to the cell-vertex l for each *fv*-cell (T) from the evaluation of source and flux integrals is controlled by fluctuation distribution coefficients (α_l^T, see Chandio [3.15] and Chandio et al. [3.18]). The update for node l is constructed by summing contributions from its control volume Ω_l, formed by all *fv*-triangles sharing that node. For this purpose, Aboubacar et al. [3.19, 3.20] proposed a generalised area-weighting stencil for such schemes, of the form,

$$\left[\sum_{\forall T_l} \delta_T \, \alpha_l^T \, \Omega_T + \sum_{\forall MDC_l} (1-\delta_T) \hat{\Omega}_l^T \right] \frac{\Delta \tau_l^{n+1}}{\Delta t} = \sum_{\forall T_l} \delta_T \, \alpha_l^T \, b^T + \sum_{\forall MDC_l} (1-\delta_T) b_l^{MDC} \tag{3.41}$$

where $b^T = (-R_T + Q_T)$, $b_l^{MDC} = (-R_{MDC} + Q_{MDC})^l$. Here, Ω_T is the area of the *fv*-triangle T, whilst $\hat{\Omega}_l^T$ is the area contribution of the same triangle to the median-dual-cell. In equation (3.41), the parameter δ_T directs the balance taken between the contributions from the median-dual-cell and the triangle T. This completes the necessary detail for the *fe*- and *fv*-discretisations used.

References

[3.1] F.P.T. Baaijens, *Mixed finite element methods for viscoelastic flow analysis: a review*, J. Non-Newtonian Fluid Mech **79** (1998) 361-385.

[3.2] R.G. Owens, T.N. Phillips, *Computational Rheology*, Imperial College Press, London, (2002).

[3.3] K. Walters, M.F. Webster, *The distinctive CFD challenges of computational rheology*, International Journal for Numerical Methods in Fluids **43** (2003) 577-596.

[3.4] P. Townsend, M.F. Webster, *An algorithm for the three-dimensional transient simulation of non-Newtonian fluid flows.* In: NUMETA 87, Vol. 2:T12/1, Martinus Nijhoff, Dordrecht, 1987.

[3.5] J. Donea, *A Taylor-Galerking method for convective transport problems*, International Journal for Numerical Methods in Engineering **20** (1984) 101-119.

[3.6] R. Temam, *Theory and Numerical Analysis of the Navier-Stokes equations*, North-Holland, (1977).

[3.7] A.J. Chorin, *Numerical solution of the Navier-Stokes equations*, Mathematics of Computation **22** (1986) 745-762.

[3.8] J.v. Kan, *A second-order-accurate pressure-correction scheme for viscous incompressible flow*, SIAM Journal on Scientific and Statistical Computing **7** (1986) 870-891.

[3.9] D.M. Hawken, H.R. Tamaddon-Jahromi, P. Townsend, M.F. Webster, *A Taylor-Galerkin-based algorithm for viscous incompressible flow*, International Journal for Numerical Methods in Fluids **10** (1990) 327-351.

[3.10] E.O.A. Carew, P. Townsend, M.F. Webster, *A Taylor-Petrov-Galerkin algorithm for viscoelastic flow,* J. Non-Newtonian Fluid Mech **50** (1993) 253-287.

[3.11] A. Baloch, P. Townsend, M.F. Webster, *On the simulation of highly elastic complex flows*, J. Non-Newtonian Fluid Mech **59** (1995) 111-128.

[3.12] T.J. Chung, *Finite Element Analysis in Fluid Dynamics*, McGraw-Hill, (1978).

[3.13] M.J. Crochet, A.R. Davies, K. Walters, *Numerical Simulation of Non-Newtonian Flow*, Vol. **1**, Elsevier, (1984).

[3.14] O.C. Zienkiewicz, K. Morgan, *Finite elements and approximation*, Wiley, New York, (1983).

[3.15] M.S. Chandio, *Numerical Study of Model, Industrial and Free-Surface Flows. In: Computer Science*, Vol. Philosophiae Doctor, University of Wales, Swansea, Swansea, U.K., 2002, p. 208.

[3.16] C. Hirsch, *Numerical Computation of Internal and External Flows: Fundamentals of Numerical Discretization*, Vol. **1**, Wiley, (1988).

[3.17] D.M. Jones, K. Walters, P.R. Williams, *On the extensional viscosity of mobile polymer solutions*, Rheological Acta **26** (1987) 20-30.

[3.18] M.S. Chandio, K.S. Sujatha, M.F. Webster, *Consistent hybrid finite volume/element formulations: model and complex viscoelastic flows*, International Journal for Numerical Methods in Fluids **45** (2004) 945-971.

[3.19] M. Aboubacar, T.N. Phillips, H.R. Tamaddon-Jahromi, B.A. Snigerev, M.F. Webster, *High-order finite volume methods for viscoelastic flow problems*, Journal of Computational Physics **199** (2004) 16-40.

[3.20] M. Aboubacar, M.F. Webster, *A cell-vertex finite volume/element method on triangles for abrupt contraction viscoelastic flows*, J. Non-Newtonian Fluid Mech. **98** (2001) 83-106.

[3.21] K.W. Morton, P.I. Crumpton and J.A. Mackenzie, *Cell vertex methods for inviscid and viscous flows*, Computers & Fluids **22** (1993) 91-102.

[3.22] P. Wapperom and M.F. Webster, *A second-order hybrid finite element/ volume method for viscoelastic flows*, J. Non-Newtonian Fluid Mech **79** (1998) 405-431.

[3.23] P. Wapperom and M.F. Webster, *Simulation for viscoelastic flow by a finite volume/element method*, Computer Methods in Applied Mechanics and Engineering **180** (1999) 281-304.

Science is beautiful when it makes simple explanations of phenomena or connections between different observations.

Stephen Hawking

Chapter 4

Modified Bautista-Manero (MBM) Modelling for Hyperbolic Contraction-Expansion Flows (Squeezed Flows)

In this study, modelling of network-structured material flow is considered through a rounded-corner, hyperbolic 4:1:4 contraction-expansion geometry, under an axisymmetric configuration. Three representative constitutive models are adopted to represent networked behaviour and to investigate the flow of wormlike micellar fluids. This includes the *MBM* model (for base thixotropic properties), some newly proposed micellar models (*NM_*τ_p & *NM_T*; for advanced thixotropic modelling), and the *EPPT* model (for contrast against non-thixotropic properties). In this

configuration, emphasis is paid to interpret the flow behaviour of these constitutive models, against their response in simple rheometrical flows (through characterization of their material function response). Here, the flow is considered under laminar, isothermal, and incompressible flow conditions. To determine the factors that contribute to *epd*-prediction, a supplementary study has also been constructed, contrasting current findings against those reported earlier in Lopez-Aguilar et al. [4.1], for abrupt axisymmetric, rounded-corner, 4:1:4 contraction-expansion flow.

4.1 Introduction

The viscoelastic surfactant (wormlike micellar) solutions are currently used in a wide range of industrial applications including examples within oil fields as fracturing-fluids (enhanced-oil-recovery), and in hydrodynamic engineering as drag-reducing agents [4.2, 4.3]. Moreover, the flow through a contraction-expansion configuration has more recently become established as a standard benchmark problem in experimental and computational rheology [4.4].

This work is devoted to solve numerically the hyperboilc 4:1:4 rounded-corner contraction-expansion flow of worm-like micellar systems using the MBM model approach [4.5-4.7]. The specific geometry selected closely represents the typical shape of a bottle-neck of industrial interest, which may be filled or emptied of personal care products, such as shampoos. The unique rheological properties of these types of non-Newtonian complex viscoelastic fluids have led to their varied application such as rheological modifiers (as in cosmetics, health care products). They also prove important in a wide range of industrial applications, namely inkjet printing and enhanced oil recovery (EOR).

In the linear viscoelastic region, these fluids behave as ideal Maxwell fluids and demonstrate shear-banding response in steady shear measurements. However, any variation in geometry throughout the processing of a non-Newtonian fluid (wormlike micelle solutions) introduces an extensional component to the flow, making the extensional measurements an important factor in demonstrating complex flow behaviour such as through a contraction-expansion configuration. Wormlike micelles are self-assembling materials, capable of changing their morphological internal structure, through breakdown and formation of their polymer chains, under large

elastic stress. Therefore, they may self-select their rheological properties to suitably fit to change in alternative deformation settings [4.8]. The rheology and applications for wormlike micelle solutions is the subject of several excellent review articles [4.9-4.13]. Many approaches have been pursued to model the behaviour of wormlike micellar flow; such as MBM [4.5-4.7 and 4.14] and VCM model [4.15-4.17]. The contraction–expansion flow is a complex flow, yet standard benchmark in experimental and computational rheology [4.4], containing regions of strong shear near the walls, alongside inhomogeneous extension along the centreline [4.18], and mixed shear-extension elsewhere.

The first point on which to focus is the precise prediction of excess pressure-drop (*epd*). Such an extra pressure loss is observed in axisymmetric contraction-expansion flows, for constant-viscosity Boger fluids (and some shear-thinning) elastic liquids, over that presented by an equivalent Newtonian fluid of similar viscosity. Results from a recent numerical simulation, Nyström et. al. [4.19], reveal how reasonably constant and maximum extensional viscosity can be extracted from particular geometry choices by avoiding the creation of vortices. These authors showed that the hyperbolic contraction is that best-suited to generate constant uniaxial extension in the measuring system, and in minimizing the impact of shear at the flow centre-line. There, flows of Newtonian and constant-viscosity viscoelastic Boger fluids (FENE-CR model) were investigated, through several different axisymmetric contraction configurations, offering comparative analysis of strain and shear-rate profiles, pressure drops and N_1 profiles.

Taking the knowledge gained in our previous work on modelling of wormlike micellar solutions through abrupt contraction-expansion configurations [4.1], this chapter demonstrates the influence of geometric shape-choice and its effect on *epd* prediction. The capability of new models is examined in their prediction of enhanced *epd.* Fuller detail covering the various rheological model parameters used in this study are presented below.

4.2 Constitutive models

For an incompressible and isothermal flow, the governing equations in their non-dimensional forms may be written as follows (Equations 2.43 and 2.44),

$$\nabla \cdot \mathbf{u} = 0, \quad \textit{Continuity equation} \tag{4.1}$$

$$Re\frac{\partial \mathbf{u}}{\partial t} = \nabla \cdot \mathbf{T} - Re\mathbf{u} \cdot \nabla \mathbf{u} - \nabla p. \quad \textit{Momentum equation} \tag{4.2}$$

Hereafter, three types of constitutive equations are utilised - these include the MBM model, some newly proposed micellar models (NM_τ_p & NM_T) and an EPPT model. A generalised constitutive equation may then be defined, covering all three such possibilities and in dimensionless differential form [4.20], viz.

$$We\frac{\partial \boldsymbol{\tau}_p}{\partial t} = 2(1-\beta)\mathbf{D} - f\boldsymbol{\tau}_p - We\left(\mathbf{u}.\nabla\boldsymbol{\tau}_p - \nabla\mathbf{u}^T.\boldsymbol{\tau}_p - \boldsymbol{\tau}_p.\nabla\mathbf{u}\right) \tag{4.3}$$

By identifying the functional f, for each model considered here (tabulated in Table 4.1), the constitutive equations may be enforced into this general framework. The f-function for the EPTT specified as,

$$f(\boldsymbol{\tau}) = exp\left(\frac{\varepsilon_{PTT}}{1-\beta}WeTr(\boldsymbol{\tau})\right). \quad \textit{(EPTT)} \tag{4.4}$$

In the case of the MBM model, and upon appealing to a scale-factor $f = \left(\eta_{po}/\eta_p\right)$, the kinetic structure equation can be reorganize into the following form, hence determining the relevant f-functional,

$$\frac{\partial f}{\partial t} = \frac{1}{\omega}(1-f) + \xi_{\eta_{po}}\boldsymbol{\tau}_p : \mathbf{D}^{1}. \quad \textit{(MBM)} \tag{4.5}$$

Upon introducing elastic effects, through the destruction term (second term on rhs) in the construction-destruction kinetics equation for the original MBM, can be considered either only by polymeric energy-dissipation (NM_τ_p model), or from both contributions of polymeric and solvent energy-dissipation (NM_T model). Thus, the

[1] ($\xi_{\eta_{p0}} = (k/\eta_\infty)\eta_{p0}(\eta_{p0}+\eta_s)U/L$) is the destruction dimensionless parameter for MBM.

structure equation for these new micellar models [4.1], which are driven by phenomenological observation, can be defined as,

$$\frac{\partial f}{\partial t}=\frac{1}{\omega}(1-f)+\xi_{G_0} We\boldsymbol{\tau}_p:\mathbf{D}, \qquad (NM\_\tau_p) \qquad (4.6)$$

$$\frac{\partial f}{\partial t}=\frac{1}{\omega}(1-f)+\xi_{G_0} We\mathbf{T}:\mathbf{D}. \qquad (NM\_T) \qquad (4.7)$$

where ($\omega=\lambda_s U/L$) is the structural-construction dimensionless parameter and $\xi_{G_0}=(k/\eta_\infty)G_0(\eta_{p0}+\eta_s)$ is the new and replaced structural-destruction dimensionless parameter, with $\eta_{p0}=G_0\lambda_1$.

Finally, to accomplish high elasticity predictions for micellar fluids, a new convoluted approach has been designed and introduced in [4.1] – this draws upon combinations of *f*-functionals from EPTT and micellar models. The corresponding *f*-functional (with other alternatives are also tabulated in Table 4.1) for the convoluted (EPTT/MBM) model is then given by:

$$f(\boldsymbol{\tau})=\left(1+\omega\xi_{\eta_{po}}\boldsymbol{\tau}_p:\mathbf{D}\right)exp\left(\frac{\varepsilon_{PTT}}{1-\beta}WeTr(\boldsymbol{\tau})\right), \qquad (EPTT/MBM) \qquad (4.8)$$

Rheometrical functions predicted by the above mentioned non-convoluted models are plotted in Figure 4.1. For comparison purposes, the rheological model parameters and the solvent ratio β={1/9,0.9}, representing highly-polymeric and solvent dominated-fluid, respectively, are chosen to match those of Lopez-Aguilar et al. [4.1] (see Table 4.2). The EPTT model parameters selected for study are ε_{PTT}={0.25, 0.02}, to cover *Moderate Hardening* (*MH*) and *Severe Hardening* (*SH*) scenarios. These correspond to predicted flow behaviour of many common polymer melts and dilute polymer solutions, respectively [4.21]. Material functions for the micellar models, that match peaks in extensional viscosity for EPTT configurations, realise *structure-construction* ω-parameter values of ω=4.0 for *MH*, and ω=0.28 for *SH* fluids. In contrast, the *structure-destruction* ξ-parameter undertakes different values for each micellar model option. The rheometrical functions for the convoluted models are plotted in Figure 4.2 for β=1/9 and *MH* response. Here, Figure 4.2a,

demonstrates that the extensional and shear viscosity curves, under these specific parameter choices, lie closer to those for EPTT.

The numerical simulations reported in this chapter are obtained with the time-marching hybrid finite element/finite volume (*fe/fv*) scheme as outlined in chapter 3 (also, see [4.1]).

4.3 Numerical procedures and problem specification

Hybrid finite element/finite volume scheme

The numerical simulations reported in this study are obtained with the time-marching semi-implicit incremental pressure-correction hybrid finite element/finite volume (*fe/fv*) scheme, as employed elsewhere in partner studies (see [4.1, 4.22, 4.23]). Hence, a brief summary only is provided here. The scheme base is that of two-step Lax-Wendroff form within a Taylor series approximated up to $O(\Delta t^2)$. The pressure is incremented through a Pressure-Correction strategy (TGPC) [4.22], rendering a three-stage scheme structure. A spatial Galerkin *fe* discretisation is applied for the momentum equation in stage 1, the pressure-correction in stage 2, and the incompressibility constraint in stage 3. The constitutive equation for stress in stage 1 is solved through a cell-vertex finite volume scheme (see below). At stage 2, a Poisson equation is solved for the pressure difference. Stage 3 uses the pressure-difference to compute a solenoidal velocity field completing the time-step cycle for velocity components. Under *fe* discretisation, the momentum diffusive term is treated in a semi-implicit manner to improve stability; an element-by-element Jacobi iteration method is used to solve for the velocity at steps 1 and 3; and a direct Choleski-decomposition method is employed for the pressure solution stage at step 2.

Finite volume cell-vertex scheme for stress

Cell-vertex *fv*-schemes applied to stress are based upon an upwinding fluctuation distribution technique, which distributes triangular control volume residuals to construct nodal solution updates [4.22]. The objective is to evaluate the flux ($\boldsymbol{R} = \mathbf{u}.\nabla\boldsymbol{\tau},$) and source ($\boldsymbol{Q}$) variations of the stress equation over each *fv*-triangle (a sub-triangle within the parent *fe*-triangle). Here, the choice of fluctuation distribution scheme is that of Low Diffusion B (*LDB*): linearity preserving (necessary for high

accuracy at steady-state), but non-positive (so as to avoid imposing this property upon source terms, that deteriorates accuracy). The fundamentals of such a finite volume cell-vertex scheme may be explained as follows: The nodal stress update is obtained by summing all contributions from its control volume Ω_l, composed of all *fv*-triangles surrounding node (l). The flux and source residuals may be evaluated over two separate control volumes, Ω_T the area of *fv*-triangle T and $\hat{\Omega}_l^T$ the area of its median-dual-cell (*MDC*), both associated with a given node (l) within the *fv*-cell T. This generates a fluctuation distribution contribution governed over the *fv*-triangle T, (R_T, Q_T), and that subtended over the median-dual-cell zone, (R_{mdc}, Q_{mdc}). Such a procedure requires appropriate area-weighting to maintain consistency and temporal accuracy, furnishing a generalized *fv*-nodal solution update equation per stress component of the form,

$$\left[\sum_{\forall T_l}\delta_T\alpha_l^T\Omega_T+\sum_{\forall MDC_l}(1-\delta_T)\hat{\Omega}_l^T\right]\frac{\Delta\tau_l^{n+1}}{\Delta t}=\sum_{\forall T_l}\delta_T\alpha_l^T b^T+\sum_{\forall MDC_l}(1-\delta_T)b_l^{MDC} \qquad (4.9)$$

where $b^T=\left(-R_T+Q_T\right)$, $b_l^{MDC}=\left(-R_{MDC}+Q_{MDC}\right)^l$, Ω_T is the area of the *fv*-triangle T, and $\hat{\Omega}_l^T$ is the area of its median-dual-cell (*MDC*). The weighting parameter, $0\le\delta_T\le 1$, governs the balance between contributions from the median-dual-cell and the *fv*-triangle T. This discrete stencil identifies fluctuation distribution and median dual cell contributions, area weighting and upwinding factors (α_l^T-scheme dependent). Such a scheme and parametric specification is provided in full detail in Webster *et al.* [4.24, 4.25], covering the interconnectivity of the *fv*-triangular cells (T_i) surrounding the sample node (l), the zone of *mdc*, the parent triangular *fe*-cell, and the fluctuation distribution (*fv*-upwinding) parameters (α_i^T), for i = l, j, k on each *fv*-cell.

Problem specification

The geometrical configuration used in the present study, that of the axisymmetric rounded-corner hyperbolic 4:1:4 contraction-expansion, is presented in Figure 4.3 (symmetry assumed, half-domain representation). Here, the standard finite element mesh used has 1776 elements and 3791 nodes with 23754 degrees of

freedom. No-slip boundary conditions are imposed at the wall. Symmetry conditions apply along the centreline (no shear), and due to axial symmetry, solution is conducted only over half of the flow domain (steady flow assumed). Then, a pressure-driven Poiseuille deformation flow is applied at entry and exit; specifying entry stress level boundary conditions. In this study, flow response is studied through solutions at continuously elevating elasticity, in terms of Weissenberg number (*We*). Simulations commence from a relatively low-level of *We*=0.1, in which internal-domain initial conditions for stress and velocity are from rest; then, solutions are generated subsequently in incremental continuation steps of *We*, until a critical level of *We* (We_{crit}) is reached (Table 4.3). All solutions are described under steady-state conditions, where the relative maximum difference between solution approximations over sequential time steps falls below a set threshold (10^{-6} in this study) to ensure convergence.steps falls below a set threshold (10^{-6} in this study) to ensure convergence.

Pressure-drop calibration

Under contraction-expansion flow, the total pressure drop ($\Delta p = p_{inlet} - p_{exit}$) is the sum of the fully-developed (*fd*) Poiseuille flow contribution (Δp_{fd}) plus an extra loss caused by the presence of the contraction-expansion, referred to as 'entry correction' (Δp_{en}). Excess Pressure Drop (*epd*), for a Boger fluid with constant shear-viscosity and strain-hardening property, is defined in terms of normalised entry correction by Binding et al. [4.26], as,

$$P = \frac{\left(\Delta p - \Delta p_{fd}\right)_{Boger}}{\left(\Delta p - \Delta p_{fd}\right)_{Newt}} = \frac{\left(\Delta p_{en}\right)_{Boger}}{\left(\Delta p_{en}\right)_{Newt}}, \qquad \Delta p_{fd} = \Delta p_u L_u + \Delta p_d L_d \tag{4.10}$$

Here, Δp is the total pressure difference between the inlet and outlet, sampled along the geometry centerline, Δp_u and Δp_d represent the fully developed pressure gradient in the upstream and downstream region respectively, and, L_u, L_d are the distances from an inlet point to mid-plane constriction and from that mid-plane to the exit, respectively. The pressure at the exit of the geometry is fixed to be zero.

4.4 Results and discussions

Firstly under rising *We*, the relationship is explored between pressure-drop and the material functions involved. This exercise is then systematically treated in turn for other variables of interest, such as: first normal stress difference (N_1), along the symmetry line (in pure extension, variable); N_1 along the boundary wall (in pure shear, variable); and strain rate across the geometry.

4.4.1 Excess pressure-drop (epd), β= {1/9, 0.9}

As mentioned above and displayed in Figure 4.4, at low-levels of elasticity (We→0), the MBM (micellar model) is found to inconsistently predict epd–values; as opposed to consistent findings for the network-based EPTT alternative. Here, the MBM data-curve underpredicts the epd values within the Stokesian limit by {40%, 10%} for both {MH, SH} highly-polymeric fluids (high-solute content, β=1/9). To overcome such an epd shortfall at low deformation rates (equivalent to low We), a correction to the MBM formulation has been proposed that introduces elastic effects into the structure equation (via the destruction contribution) [4.1]. In this context, two variants have been proposed; namely: (i) a model which uses the energy dissipated by the polymer to break down the structure of the material (NM_τp model); and (ii) an option that considers the polymeric plus solvent dissipation in its structure dynamics (NM_T model).

Firstly, discussion is initiated on pressure-drop findings for the main flow-geometry of interest, hyperbolic 4:1:4 contraction-expansion, before proceeding to comparison against our earlier results derived for the abrupt rounded-corner 4:1:4 geometry flow [4.1].

a) epd, β= {1/9, 0.9}, MH response, non-convoluted models

In Figure 4.5(a-b), normalized *epd* predictions for the non-convoluted EPTT, MBM, NM_τ_p and NM_T models are contrasted under moderate strain-hardening response and β={1/9, 0.9} solvent fraction levels. A significant improvement in *epd* estimation is obtained with the NM_τ_p and NM_T, in contrast to that with MBM; thus confirming the regathering of consistent *epd*-estimation at low elasticity levels, as addressed in [4.1]. Under such consistent trends, NM_τ_p and NM_T *epd* data-

curves now drop from the unity reference line, as demanded in theory. Moreover, an initial declining trend in *epd* data-curves with increasing elasticity is observed for all models, irrespective of the polymer concentration level, β= {1/9, 0.9}. For the *highly-polymeric fluids* (β=1/9) and at low levels of *We* (Figure 4.5a), both thixotropic NM_τ_p and NM_T *epd*-data provide an initial rapidly decaying trend, similar to that observed with the EPTT model, up to their split and separation around *We*~1. At this point, a change in slope is observed between the non-thixotropic EPTT and the thixotropic new micellar data-curves. The micellar *epd*-data soften their slope earlier as *We* rises, tending to a slightly larger asymptote (lower limiting plateau) of NM-*epd*~0.2, as opposed to the EPTT-*epd* asymptote of ~0.1. This difference may be attributed to the stronger N_1 functionality displayed by EPTT in simple shear flow for larger limiting deformation rates (Figure 4.1b). Notably as shear rate rises, monotonic rise is apparent in EPTT-N_1, whilst MBM and NM_τ_p forms plateau at moderate-to-high rates; with even ultimate decline found with NM_T. Recall the competing roles between *epd*-diminishing N_1 and pseudoplasticity, and *epd*-enhancing extensional viscosity [4.27]. Here, the lower *epd*-curve declines under the NM_τ_p model compared with NM_T *epd*-predictions; this leads to a higher limit in We_{lim} (=195) for NM_τ_p.

For solvent-dominated fluids (β=0.9) (see Figure 4.5b), again there is similar significant impact detected in initial sharp decay rate, and the limiting level of *epd*-data is now enhanced over (β=1/9). The reasoning behind such enhanced *epd*-(β=0.9)-predictions, is related to the comparative amounts of solvent-to-polymer concentration in these materials. The solvent fraction level fixes a second *epd* reference line (lower than unity, first Newtonian reference line) - this corresponds to the dimensionless second Newtonian viscosity plateau in simple shear flow, observed at high shear rates. In particular, with the highly-polymeric fluids (β=1/9), this reference line is fixed at *epd*=1/9 unit, whilst the solvent-dominated materials (β=0.9) have a second reference line at *epd*=0.9 unit. Associated with these two reference levels, different interesting responses can be described at high deformation rates. Here, *epd*-curves for all models and highly-polymeric fluids (β=1/9; Figure 4.5a) asymptote to their respective We_{lim} *above* the second Newtonian high-rate reference line. In contrast, for solvent-dominated fluids (β=0.9; Figure 4.5b), the EPTT data-curve crosses this second Newtonian limit at *We*~100 (losing its elastic

properties). Likewise, as already observed in more sudden contraction geometries [4.1], NM_T provides a minimum in its *epd*- data-curve around *We*~50, from which a rising trend is observed (consistent with N_1-trends). In comparison, the slope for the EPTT curve almost disappears, and eventually plateaus out, as elasticity is increased (recall N_1 effects on *epd*-prediction; [27]). For NM_T results, one may argue that this finding may be related to the maximum and subsequent decline observed in simple shear N_1 as the rate is increased, whilst EPTT findings provide a monotonic rising trend (Figure 4.1b). Interestingly, in the range of $0<We<50$, and contrasting NM_T in comparison to EPTT predictions, the NM_T *epd*-curve reveals relatively lower *epd*-values with respect to EPTT data. Alternatively, for highly-polymeric instances, the NM_T *epd*-curve lies above that for EPTT; and such observations apply uniformly throughout the complete *We*-range analysed. Finally, the MBM *epd*-curve follows the general micellar plateauing trend as *We* rises, lying above that of NM_τ_p *epd*-data, whilst navigating towards its We_{lim} (=53).

b) epd, β={1/9, 0.9}, SH response, non-convoluted models

Next to identify with more severe extensional response, *epd*-data plots in Figure 4.5(c-d) are provided for non-convoluted EPTT, MBM, NM_τ_p and NM_T models with *strong strain-hardening* (*SH*) properties, again covering the two instances of solvent fraction levels of $\beta=\{1/9,0.9\}$. Data for the highly-polymeric fluids ($\beta=1/9$) are plotted in Figure 4.5c, and reveal analogous trends as reported above for *MH* response (see Figure 4.5a). Notably, at vanishing elasticity levels, corresponding *SH*-results for MBM display a significantly smaller deviation from the unity reference line (than *MH*-results); yet, this is still prominent and around *epd*~0.9, which represent a 10% of deviation from the unity reference. This decrease in drop is due to the reduction of the construction parameter from {ω=4, MH} to {ω=0.28, SH} (Figure 4.4 a and b) and can be explained in terms of the steady *f*-functional for these micellar models (see Table 1 in [4.1]). In these expressions, the dissipation function is scaled by the product of the construction (ω) and destruction ($\xi_{\eta p0}$ or ξ_{G0}) parameters (and *We* for the new micellar models). Hence, the decrement in any of these parameters, would weaken the influence of the dissipation function in its departure from Oldroyd-B behaviour ($f=1$); notably, it is this feature which ultimately provokes the display of non-linear features, such as pseudoplaticity and strain-

hardening/softening. Consistently and once more, both new micellar models (NM_τ_p and NM_T) demonstrate accurate capture for *epd*-prediction at low-levels of *We* (elasticity/flow-rate). The NM_τ_p-*epd*-curve exhibits a close pattern to that for NM_T (Figure 4.5c), up to its limiting We_{lim} (=39.6). In contrast, EPTT *SH*-results follow a smooth declining trend to *MH*-results, with signs of plateauing at *epd*~0.2 prior to attaining its We_{lim}=350. For solvent-dominated fluids (β=0.9; Figure 4.5d), the same trends described above for *MH*-fluids hold (see Figure 4.5b), with the main difference being that for *SH*-response, the EPTT-*epd*-curve now does not cross the second-lower Newtonian reference line.

c) epd, β= {1/9, 0.9}, MH response, convoluted models

Attention now switches to the interrogation of convoluted micellar model performance. Hence, *epd*-data with increasing *We* is presented in Figure 4.6 (a,b), contrasting the conventional EPTT against its convoluted micellar counterparts (EPTT/MBM, EPTT/NM_τ_p, EPTT/NM_T). Here, for the sake of brevity and to avoid repetition, only the moderate hardening scenario is reported for both levels of solvent fraction, β=1/9 (highly-polymeric) and β=0.9 (solvent-dominated).

In general and up to *We*~100, the *epd*-data recorded for all convoluted models and both β-settings, follow closely the pure-EPTT predictions-patterns (Figure 4.6a and b). Beyond this stage, for *We*>100, EPTT *epd*-response provides values slightly higher than those for convoluted models. The closeness of trends and values evidences the consequence of such convolution: the exponential nature of the EPTT *f*-functional completely dominates over the linear functionality of the micellar models (*in steady-state*). This provokes (i) a conspicuous We_{lim} elevation with respect to the non-convoluted micellar models; and (ii) and EPTT-like *epd*-response for the convoluted models. The We_{lim}-elevation is due to the relatively stronger *f-We* explicit relationship for these models (as true for pure-EPTT also) [4.1].

Comparison of *epd*-results across solvent fraction level β={1/9,0.9}, illustrates the differences in the level of *epd*-prediction reached (similar to the non-convoluted cases). The initial rate of decline and subsequent marked change in slope (*We*~25) are common features across all model findings, irrespective of polymer concentration level. Interestingly, this change in slope occurs at *epd*~{0.15,0.92} for

solvent fractions of β={1/9,0.9}. For larger elasticity levels (*We*>100), a slight gap appears between EPTT and convoluted *epd*-predictions, being sustained subsequently and more prominent with β=0.9. Then, the high-rate limiting-slopes for these curves remain invariant whilst approaching their We_{lim}. As noted above with non-convoluted results, the trend in *epd* for highly-polymeric fluids (β=1/9), is to asymptote and plateau out to a level slightly above the second Newtonian *epd* reference-level (thus, non-intersecting). In contrast, for solvent-dominated fluids (β=0.9), these *epd*-curves intersect the Newtonian second reference line at *We*~75.

4.4.2 *Strain-rate ($\frac{\partial u_z}{\partial z} = \hat{\varepsilon}$) results along the symmetry line, β={1/9, 0.9}, MH & SH fluids*

Here, the ultimate goal is to establish a relationship between the pressure drop and extensional deformation-rate ($\hat{\varepsilon} = \frac{\partial u_z}{\partial z}$) along the symmetry-line. Figures 4.7-4.8, show the evolution of the strain-rate ($\hat{\varepsilon}$) along the geometry centreline, for each choice of solvent fraction level β={1/9,0.9} across the various models (EPTT, MBM, NM_ τ_p and NM_T), for both *MH* and *SH* response, and at both levels of low and high limiting *We*.

a) Highly-polymeric β=1/9 fluids; MH & SH response

In Figure 4.7a (β=1/9, MH) and at the low level of *We*=0.1, the extension rate is observed to smoothly rise in $\hat{\varepsilon}$ up to its maximum of $\hat{\varepsilon}$~0.12 units (true for all models), located at the start of the hyperbolic contraction zone (z=0), that plateaus for EPTT and non-convoluted models (NM_τ_p & NM_T). In contrast, with the MBM model a declining trend is recorded, to the level of $\hat{\varepsilon}$ ~0.08 units located, just in front of the contraction mid-plane (z=15). Then at z=15, a sudden drop to negative values is observed, to approach its minimum ($\hat{\varepsilon}$ ~-0.12) by the end of the hyperbolic contraction zone (z=30). Finally, beyond z>30 entry conditions are reflected, to finally recover fully-developed straight-channel flow conditions.

Instructive in ***highly-polymeric*** *high-level We* interrogation is the realisation of pending numerical instability and solution breakdown. This data also reveals how far one is removed from constant strain-rate plateaus under such setting. Increasing *We*

to critical levels (We_{lim}) (shown in Figure 4.7b) is reflected in a higher level of strain-rate before the mid-plane in the contraction region for all micellar models (MBM, NM_τ_p and NM_T). A shift in maxima-location is observed to just before the mid-plane, associated with the thixotropic MBM model ($\hat{\dot{\varepsilon}}$ ~0.3 units); whilst a minima is relocated after the mid-plane, towards the end of the hyperbolic exit-contraction zone (z=30) in NM_T/MBM solutions. The MBM results characterize the trends, for which the We_{lim}=82 solution provides a shift in location of extension-rate maximum, from the region at the start of the hyperbolic contraction zone (z=0, low *We*), to the region adjacent to the mid-plane (z=15, high *We*). In contrast, solutions for {NM_τ_p, NM_T} at We_{lim} ={195,110}, now display overshoots, with local maxima (larger, around z~0) and minima (smaller, around z~15) across the hyperbolic entry-contraction zone (0≤z≤15). A similar position arises across the hyperbolic exit-contraction zone (15≤z≤30), but also where patterns of oscillatory form are now detected in all micellar model solutions at We_{lim}; these persist towards the end of the hyperbolic exit-contraction zone (z=30, causing the local minima), and beyond this station towards domain exit (disrupting subsequent solution continuation in *We*). Noticeably, such complex behaviour is not observed in EPTT solutions, for which the strain-rate profile is relatively much smoother and more symmetrical, with maximum and minimum values of $\hat{\dot{\varepsilon}}$ ~{0.12,-0.12} across the contraction region. Such smooth EPTT-behaviour may be attributed to its superior numerical stability properties, gathered through its high level of We_{lim} =1000* attained.

Switching next to consideration of strong hardening (*SH*) response (Figure 4.7c), similar behavioural trends are recorded in all *SH*-cases at low *We*=0.1 to that for *MH*-cases, with a constant level of maximum and minimum strain-rate ($\hat{\dot{\varepsilon}}$ ~0.12 units), located on both sides of the contraction mid-plane. With the new micellar variants at low *We*, *SH*-plateau levels are now observed to be flatter here (*improved solutions*) than for *MH*-response (Figure 4.7c vs Figure 4.7a). When elasticity is increased to We_{lim}, once more overall trends for *SH*-cases repeat those for *MH*-cases. In {NM_τ_p, NM_T} solutions at We_{lim} ={39.6,55}, no overshoots are apparent (as above), with simple monotonic rise in strain-rate across the hyperbolic entry-contraction zone 0≤z≤15. The maxima-peak is located just before the mid-plane for all model solutions (Figure 4.7d), with the sharpest peak occurring for MBM data ($\hat{\dot{\varepsilon}}$ ~0.5 units), followed then by NM_T and NM_τ_p ($\hat{\dot{\varepsilon}}$ ~0.2 units), and finally by EPTT

($\hat{\varepsilon}$ ~0.1 units). Notably, EPTT solutions attain the highest We_{lim} (=350). Note, that the maxima-peak MBM strain-rate is considerably larger than that for other models; about five times that of EPTT and twice as large as for the other micellar models. In consequence, MBM attains the lowest We_{lim}=45 amongst other alternative models. It is the region beyond the mid-plane where significant solution oscillation can be distinguished. This is a flow zone of stable numerical solution for EPTT representation, whilst instability in micellar solutions is manifest - through detection of local minima-maxima, with the local-minima located towards the end of the hyperbolic exit-contraction zone (z=30).

b) Solvent-dominated β=0.9 fluids; MH & SH response

The above high-solute findings may be contrasted against the solvent-dominated situation upon adjusting the solvent fraction to β=0.9 (increasing solvent concentration, approaching Boger fluid composition). Then, at the *low level setting of We=0.1*, and considering both *MH* and *SH* response (Figures. 4.8a and 4.8c, respectively), solutions for all non-convoluted models are found to produce similar flat symmetric profile form about the contraction mid-plane, with strain-rate maxima and minima of $\{\hat{\varepsilon}_{max}, \hat{\varepsilon}_{min}\}$~{0.12,-0.12} units. This is the key deformation outcome sought in such a hyperbolic flow geometry design – achieving the desired constant plateau-level strain-rate throughout the hyperbolic sections, reflected in sign for entry and exit zones. This scenario renders useful data upon which extensional viscosity estimation may be made (see below to counterpart N_1 calculation in pure-extension).

Here even at critical elastic levels (We_{lim}), and with the added benefit of stabilising high solvent contributions, these smooth profile patterns are now only slightly adjusted (see Figures 4.8b and 4.8d; *unlike above*). Slight highly-localised undershoot-overshoots are captured in the micellar solutions, around z={0, 15, 30} in *MH*-response, with minor oscillatory form across the hyperbolic exit-contraction zone (15≤z≤30) (as in Figure 4.8b); these influences are simply amplified under *SH*-response (Figure 4.8d).

4.4.3 *Normal stress difference (N_1) results along the symmetry line (in extension) and the boundary wall (in shear), β={1/9, 0.9}, MH & SH fluids*

In keeping with the above, here, the same settings in terms of the models and solvent fractions have been considered. Accordingly, the normal stress difference (N_1) response along the symmetry line (N_1 in extension) and the boundary wall (N_1 in shear) are shown in Figures 4.9-4.12. Once more, both *MH* and *SH* cases are covered and both low and high (critical) *We*-levels are reported.

a) Highly-polymeric β=1/9 fluids; MH & SH response

Figure 4.9 (a-d) for {β=1/9, *MH*} case, presents N_1 in pure extension along the symmetry line and N_1 in pure shear along the boundary wall. At the low level of *We*=0.1 (Figure 4.9a) all models provide similar sharp rise (overshoot) in N_1 around the start of the hyperbolic contraction (z=0) up to N_1~0.1 units developed, followed by an abrupt drop to the level of N_1~0.06 units. Then, beyond that point, a rising trend is observed in N_1 up to the location before the mid-plane (z=15), with the faster rate-of-rise for EPTT followed by that for non-convoluted models (NM_τ_p & NM_T). This rise in N_1 is less visible for the MBM model. Viewing Figures 4.7a and 4.9a, corresponding to strain-rate ($\hat{\varepsilon}$) and stress (N_1) along the symmetry line respectively, such peaks in strain-rate and stress correlate to the same location. Here, a stress (N_1) minimum occurs just beyond the mid-plane (z=15), followed by a rise towards the end of the contraction (z=30), which then recovers to inlet-value levels. Additional features arise of local N_1-maxima on entry at z=4 units, and on exit at z=(30-4) units; these are more conspicuous in the *highly-solvent case* and are commented upon below. One notes in passing here, that the *highly-solvent* N_1-profiles (below) in contrast to these *highly-polymeric* alternatives are much more amenable to rheological characterisation, specifically to extensional viscosity determination.

Results in Figure 4.9b at the critical *We*, for N_1 in pure extension along the symmetry line, indicate that in the case of the MBM model with We_{lim}=82 a large stress (N_1~22 units) is developed around the constriction mid-plane which is responsible for the increasing trend in excess pressure-drop (*epd*) when compared to other corresponding models (see Figure 4.5a). For non-convoluted models (NM_τ_p & NM_T), this peak in stress is located at the same position, but with much smaller

scale (N_1~3 units). Contrasting EPTT-response at the highest level of We_{lim} (=1000*) - this is practically flat through the entire geometry and directly corresponds with the smooth strain-rate response (see Figure 4.7b).

Figure 4.9 (c,d) (β=1/9, MH) presents corresponding findings on the normal stress difference along the boundary wall (N_1 in shear). At low elasticity level (We=0.1) and for all models, the same decline is observed to a negative value for N_1, in two entrance and exit hyperbolic contraction regions. Here (Figure 4.9c), N_1 exhibits a peak-value around the mid-plane (z=15), with the sharpest peak and highest value of N_1 for EPTT (N_1~3 units), followed then by NM_T and NM_τ_p (N_1~1.8 units), and lastly by MBM (N_1~0.4 units).

Upon increasing We up to critical levels (We_{lim}), a major increase in N_1–magnitude up to ~95 units is observed. This corresponds to the N_1-MBM solution (We_{lim}=82), whilst the N_1-EPTT (We_{lim} =1000*) displays a reduction to zero (Figure 4.9d). In general, at critical We levels, the largest values of N_1 are predicted by the micellar MBM, and smallest values by the EPTT model. This is clear in symmetry line N_1-values of (Figure 4.9b) and boundary wall N_1-values of (Figure 4.9d). Hence, it can be concluded by association that the value of N_1 (in shear and extension) is directly related to the attainable elasticity number (We_{lim}). The dependency of We_{lim} over N_1-value is established through: lowest We_{lim}(=82) with MBM model, highest We_{lim}(=1000*) with EPTT model. Moreover, as a direct consequence, it is also observed that lowering N_1 allows predictive capability to reach much greater levels of critical elasticity. The position on findings with N_1-SH for (β=1/9) of Figure 4.10 are taken below in comparative form versus Figure 4.9 for N_1-MH, and also against solvent-dominated (β=0.9) results.

b) Solvent-dominated β=0.9 fluids; MH & SH response

In the high-solvent fraction (β=0.9) context and for *low We=0.1*, the profile trends in pure extension (variable) along the symmetry line for N_1 of Figures (4.11a-*MH*, 4.12a-*SH*) are *extremely close* under any given settings (*MH* and *SH*), displaying near symmetrical patterns about the domain mid-plane. This is informative indeed, as a relationship may thus be established for N_1(z) versus axial-distance (z), in both contraction-entry and expansion-exit zones (appears almost

piecewise-linear, in two sub-sections; split at local maxima points of z=4 units in the hyperbolic entry-zone and z=(30-4) units in the hyperbolic exit-zone). Having established relatively constant levels of strain-rate ($\hat{\varepsilon}$) across these same zones above, this provides a direct measure of the functional variation of extensional viscosity across the geometry, $\eta_e(z)$. As an indication, average measures of $\eta_e(\bar{z})$ may be established for each piecewise-linear sub-section (same on either entry or exit). Overall, one seeks to link this zonal data (reflected about the mid-plane) to pressure-difference(z) for each *We*-solution; from which, and at different *We*-values, a general trend may be sought for N_1 (or η_e) verses *epd* (or Δp).

The maximum and minimum of such N_1- *low We*-data on the symmetry line are located in the same positions per (*MH* and *SH*)-setting, with the maximum shifted downstream of the start of the hyperbolic contraction (z=4 units, entry; reflected in exit zone) and minimum next to the mid-plane. This is the same realisation as for β=1/9 cases. Across *solvent-fraction variation*, significant reduction is noted in N_1:- *under MH* of one-fifth, from N_1 (~0.1 units) for β=1/9 to (~0.02 units) for β=0.9 (see Figures 4.9a and 4.11a); and *under SH* of one-tenth, from N_1 (~0.18 units) for β =1/9 to (~0.02) for β =0.9 (see Figures 4.10a and 4.12a).

Likewise, at *critical We* for both *MH* and *SH* scenarios, Figures (4.11b, 4.12b) again contrast N_1 along the symmetry line (in extension). Associating *MH*-results presented in Figures (4.9b, 4.11b), would indicate that, for either solvent-fraction setting of β=(1/9, 0.9), the peak in stress (N_1) lies at the same location around the contraction mid-plane; with a much lower value in scale for β=0.9 setting. This outcome is now completely different to that under the low *We* situation discussed above; unfortunately, at such *critical We* the counterpart strain-rates are much more variable, so that any measure of constancy is rendered rather meaningless. Considering next the *SH* response at We_{lim}, for both β (=1/9, 0.9) sets of Figures (4.10b, 4.12b): in the case of β=1/9 (Figure 4.10b), the N_1-peak is located before the mid-plane for non-convoluted models (NM_T and NM_τ_p) and EPTT; whilst for MBM, this peak is shifted to just beyond the mid-plane, with the sharpest peak for the MBM (N_1~18 units), followed then by NM_T and NM_τ_p, and finally by EPTT (N_1~1 units). This concurs with the results corresponding to strain-rate ($\hat{\varepsilon}$), shown in Figure 4.7d. For the β=0.9 of Figure 4.12b and for all micellar models, N_1 peak-

values are aligned at the centreline with a minor shift in location; these are considerably lowered in value when compared to β =1/9 results of Figure 4.10b.

As counterpart to the above, but along the boundary wall in shear (variable), for solvent ratio (β=0.9) and between low to critical *We*, N_1-results are provided in Figures 4.11(c, d)-*MH* and Figures 4.12(c, d)-*SH*. In Figure 4.11c, N_1-max-*MH* values at low *We*, decline across models from EPTT (0.3), to NM_τ_p (0.2), to NM_T (0.1),to MBM (0.05); under *SH*-setting of Figure 4.12c, N_1-max-*SH* values at low *We*, group around (0.35)-value for (EPTT, NM_τ_p) and around (0.2)-value for (NM_T, MBM).

Comparing and contrasting wall-*MH*-results between β=1/9 and β=0.9 instances, first at low elasticity level (*We*=0.1) (see Figures. 4.9c and 4.11c), the same overall trends are observed but with significantly lower N_1-values for β=0.9. For instance, the level of EPTT-N_1 value, with sharpest and largest value, shrinks from N_1 (~3 units, β=1/9) to (~0.3 units, β=0.9). A similar reductive trend can be detected under *SH*-response likewise (see Figures 4.10c and 4.12c). It is difficult to make any conclusive statements over wall-shear-findings at critical *We* levels, either across solvent fractions or (*MH*, *SH*)-settings, as the levels of *We* involved themselves vary. In this respect, one may quote for insight the extrema in MBM results, with N_1-max-***MH*** value of 18 units at We_{lim}=60 in Figure 4.11d, as compared to the N_1-max-***SH*** value of 110 units at We_{lim}=42 in Figure 4.12d. Here, the *MH* to *SH*-switch at comparable We_{lim}-levels, would appear to make a significant contribution (hence, in shear).

In summary for each model employed and over the two selected levels of elasticity, lowest *We*=0.1 and critical *We*, the elevation of solvent-fraction β from 1/9 to 0.9, produces a significant reduction in N_1–maxima along the symmetry line (in extension) and boundary wall (in shear). Switching between *MH* to *SH*-setting, also has its consequences with elevation in N_1–maxima for wall-shear conditions. Moreover, at critical levels (We_{lim}), not only is there N_1-magnitude reduction to observe, but also a downstream distortion in N_1-pattern.

4.5 Conclusion

This study has revealed some interesting results concerning hyperbolic contraction flows for thixotropic and non-thixotropic materials. Pressure-drops are seen to strongly adopt shear-thinning characteristics, falling rapidly at early levels of Weissenberg number to the second Newtonian plateau levels. Both highly-polymeric fluids and solvent-dominated (*mimicking Boger*) fluids follow such trends, each ultimately asymptoting around the corresponding second Newtonian plateau level. Here, there are differences picked up at high deformation rates (elasticity) and with convoluted models (with *MH*-setting), in that ***epd*** for solvent-dominated fluids ultimately falls below the level of the second Newtonian plateau, whilst for highly-polymeric fluids, ***epd*** lies above the same plateau.

Relatively constant strain-rates throughout the hyperbolic-entry/exit regions have been well recovered for solvent-dominated fluids and at low elasticities (all models; *MH* or *SH*-settings). For highly-polymeric fluids, this property is degraded for thixotropic forms; and even more so in the *MH*-setting. In this regard, the non-thixotrpoic EPTT strain-rates are less variable (hence, more reliable).

Following on from above, first normal stress-difference (N_1) data are instructive. Data from the pure-extension centreline zone, for solvent-dominated fluids and at low elasticities, reveals tractable results (all models; *MH* or *SH*-settings), from which useful measures may be derived on extensional viscosity. In addition, maxima in shear wall N_1-data, provide the link to successful numerical convergence and indication of pending numerical breakdown. These maxima become large towards critical levels of *We*, and particularly so under *SH*-setting.

References

[4.1] J.E. López-Aguilar, M.F. Webster, H.R. Tamaddon-Jahromi, O. Manero, *A new constitutive model for worm-like micellar systems - Numerical simulation of confined contraction-expansion flows.* J. Non-Newtonian Fluid Mech. **204** (2014) 7-21.

[4.2] J. Yang, *Viscoelastic wormlike Micelles and their Applications*, Curr. Opin. Colloid Interface Sci. **7**, 276 - 281 (2002).

[4.3] M.J. Rosen, M. Dahanayake, *Industrial Utilization of Surfactants: Principle and Practice*, Champaign, Illinois, AOCS Press (2000).

[4.4] K. Walters, M.F. Webster, *The distinctive CFD challenges of computational rheology*, Int. J. Numer. Meth. Fluids **43** (2003) 577–596.

[4.5] F. Bautista, J.M. de Santos, J.E. Puig, O. Manero, *Understanding thixotropic and antithixotropic behavior of viscoelastic micellar solutions and liquid crystalline dispersions. I. The model.* J. Non-Newtonian Fluid Mech.**80** (1999) 93-113.

[4.6] O. Manero, F. Baustista, J.F.A. Soltero, J.E. Puig, *Dynamics of worm-like micelles: the Cox-Merz rule.* J. Non-Newtonian Fluid Mech. **106** (2002) 1-15.

[4.7] E.S. Boek, J.T. Padding, V.J. Anderson, P.M.J. Tardy, J.P. Crawshaw, J.R.A. Pearson, *Constitutive equations for extensional flow of wormlike micelles: stability analysis of the Bautista-Manero model.* J. Non-Newtonian Fluid Mech.**106** (2002) 1-15.

[4.8] E.S. Boek, A. Jusufi, H. Löwen, G.C. *Maitland, Molecular design of responsive fluids: molecular dynamics studies of viscoelastic surfactant solutions*, Journal of Physics: Condensed Matter **14** (2002) 9413-9430

[4.9] Anderson, V J, Pearson, J R A and Boek, E S, *The Rheology of Worm-Like Micellar Fluids*, in *Rheology Reviews*, D.M. Binding and K. Walters, Editors. 2006, The British Society of Rheology. p. 217-253.

[4.10] Zakin, J L, Lu, B and Bewerdorff, N W, *Surfactant drag reduction.* Rev. Chem. Eng., **14**(45) (1998) 253-320.

[4.11] Dreiss, C A, *Wormlike micelles: where do we stand? Recent developments, linear rheology and scattering techniques.* Soft Matter, **3** (2007) 956-970.

[4.12] Cates, M E and Fielding, S M, *Rheology of giant micelles.* Adv. Phys., **55**(7-8) (2006) 799-879.

[4.13] Yang, J, *Viscoelastic wormlike micelles and their applications.* Current Opinion in Colloid and Interface Sci., **7** (2002) 276-281.

[4.14] F. Bautista, J.F.A. Soltero, J.H. Pérez-López, J.E. Puig, O. Manero, *On the shear banding flow of elongated micellar solutions*. J. Non-Newtonian Fluid Mech. **94** (2000) 57-66.

[4.15] P.A. Vazquez, G.H. McKinley, L.P. Cook, *A network scission model for wormlike micellar solutions I. Model formulations and viscometric flow predictions*, J. Non-Newtonian Fluid Mech.**144** (2007) 122-139.

[4.16] M. Cromer, L.P. Cook, G.H. McKinley, *Pressure-driven flow or wormlike micellar solutions in rectilinear micro-channels*, J. Non-Newtonian Fluid Mech. **166** (2011) 180-193.

[4.17] L. Zhou, L.P. Cook, G.H. McKinley, *Probing shear banding transitions of the VCM model for entangled wormlike micellar solutions using large amplitude oscillatory shear (LAOS) deformations,* J. Non-Newtonian Fluid Mech. **165** (2010) 1462-1472.

[4.18] J.P. Rothstein and G.H. McKinley, *The axisymmetric contraction-expansion: the role of extesional rheology on vortex growth dynamics and the enhanced pressure drop*. J. Non-Newtonian Fluid Mech.**98** (2001) 33-63.

[4.19] M. Nyström, H.R. Tamaddon-Jahromi, M. Stading and M.F. Webster, *Numerical simulations of Boger fluids through different contraction configurations for the development of a measuring system for extensional viscosity,* Rheol Acta. **51** (2012) 713-727

[4.20] H.A. Barnes, J.F. Hutton, K. Walters, *An Introduction to Rheology*, Elsevier, (1989).

[4.21] R. Tanner, *Engineering Rheology*, second ed., Oxford, Oxford, 2000.

[4.22] P. Wapperom, M.F. Webster, *A second-order hybrid finite-element/volume method for viscoelastic flows*, J. Non-Newtonian Fluid Mech. **79** (1998) 405-431.

[4.23] F. Belblidia, H. Matallah, M.F. Webster, *Alternative subcell discretisations for viscoelastic flow: Velocity-gradient approximation*, J. Non-Newtonian Fluid Mech. **151** (2008) 69-88.

[4.24] M.F. Webster, H.R. Tamaddon-Jahromi, M. Aboubacar, *Transient viscoelastic flows in planar contractions*. J. Non-Newtonian Fluid Mech. **118**, (2004) 83-101.

[4.25] M.F. Webster, H.R. Tamaddon-Jahromi, M. Aboubacar, *Time-dependent algorithms for viscoelastic flow: Finite element/volume schemes*, Numer. Meth. Part. Differ. Eq. **21** (2005) 272-296.

[4.26] D.M. Binding, P.M. Phillips, T.N. Phillips, *Contraction /expansion flows: the pressure drop and related issues*, J. Non-Newtonian Fluid Mech.**137** (2006) 31–38.

[4.27] K. Walters, H.R. Tamaddon-Jahromi, M.F. Webster, M.F. Tomé, S. McKee, *The competing roles of extensional viscosity and normal stress difference in complex flows of elastic liquids*, Korea-Aust. Rheol. J. **21** (2009) 225-233.

Model	*f*-function
Oldroyd-B	$f = 1$
EPTT	$f = \exp\left(\frac{\varepsilon}{1-\beta} Wetr\underline{\underline{\tau}}_p\right)$
MBM	$f = 1 + \omega\xi_{\eta_{p0}} \underline{\underline{\tau}}_p : \underline{\underline{D}}$
NM_τ_p	$f = 1 + \omega\xi_{G_0} We\underline{\underline{\tau}}_p : \underline{\underline{D}}$
NM_T	$f = 1 + \omega\xi_{G_0} We\underline{\underline{T}} : \underline{\underline{D}}$
EPTT/MBM	$f = \left(1 + \omega\xi_{\eta_{p0}} \underline{\underline{\tau}}_p : \underline{\underline{D}}\right)\exp\left(\frac{\varepsilon}{1-\beta} Wetr\underline{\underline{\tau}}_p\right)$
EPTT/NM_τ_p	$f = \left(1 + \omega\xi_{G_0} We\underline{\underline{\tau}}_p : \underline{\underline{D}}\right)\exp\left(\frac{\varepsilon}{1-\beta} Wetr\underline{\underline{\tau}}_p\right)$
EPTT/NM_T	$f = \left(1 + \omega\xi_{G_0} We\underline{\underline{T}} : \underline{\underline{D}}\right)\exp\left(\frac{\varepsilon}{1-\beta} Wetr\underline{\underline{\tau}}_p\right)$

Table 4.1. Steady-state *f*-function expressions

Model	β=1/9		β=0.9	
	MH	**SH**	**MH**	**SH**
EPTT	ε=0.25	ε=0.02	ε=0.25	ε=0.02
MBM	ω=4.0 $\xi_{\eta 0}$=0.1	ω=0.28 $\xi_{\eta 0}$=0.1	ω=4.0 $\xi_{\eta 0}$=0.1	ω=0.28 $\xi_{\eta 0}$=0.1
NM_τ_p	ω=4.0 ξ_{G_0}=0.1125	ω=0.28 ξ_{G_0}=0.1125	ω=4.0 ξ_{G_0}=1.0	ω=0.28 ξ_{G_0}=1.0
NM_T	ω=4.0 ξ_{G_0}=0.1030	ω=0.28 ξ_{G_0}=0.1100	ω=4.0 ξ_{G_0}=0.1500	ω=0.28 ξ_{G_0}=0.5800
EPTT/MBM	ε=0.25 ω=4.0 $\xi_{\eta 0}$=0.0010	-	ε=0.25 ω=4.0 $\xi_{\eta 0}$=0.010	-
EPTT/NM_τ_p	ε=0.25 ω=4.0 ξ_{G_0}=0.0010	-	ε=0.25 ω=4.0 ξ_{G_0}=0.010	-
EPTT/NM_T	ε=0.25 ω=4.0 ξ_{G_0}=0.0010	-	ε=0.25 ω=4.0 ξ_{G_0}=0.010	-

Table 4.2. Parameter sets; highly-polymeric fluids (β=**1/9**), solvent-dominated fluids (β=**0.9**)

Model	β=1/9		β=0.9	
	MH	SH	MH	SH
EPTT	1000*	350	1000*	1000*
MBM	82	45	53	42
NM_τ_p	195	39.6	53	79
NM_T	110	55	500	350
EPTT/MBM	1000*	-	1000*	-
EPTT/NM_τ_p	1000*	-	1000*	-
EPTT/NM_T	1000*	-	1000*	-

Table 4.3. Limiting *We*; highly-polymeric fluids (β=1/9), solvent-dominated fluids (β=0.9)

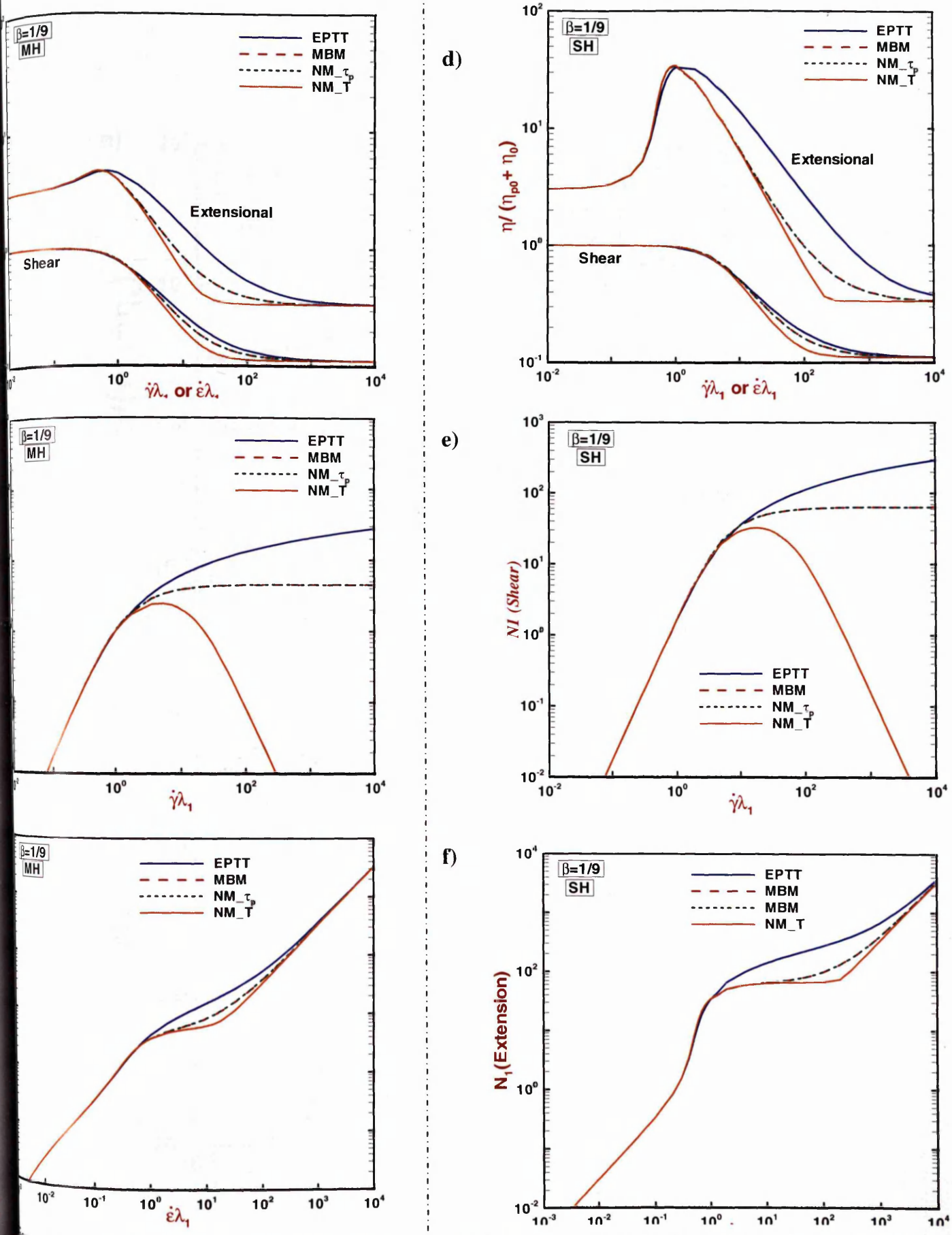

Figure 4.1. Rheometrical functions versus *We*: EPTT, MBM, NM_τ_p and NM_T models; ***β*=1/9**; ***top***-shear and extensional viscosity, ***middle***-shear N_1, ***bottom***-extension N_1; ***left*-MH** (EPTT ε=0.25, Micellar ω=4.0), ***right*-SH** (EPTT ε=0.02, Micellar ω=0.28) response

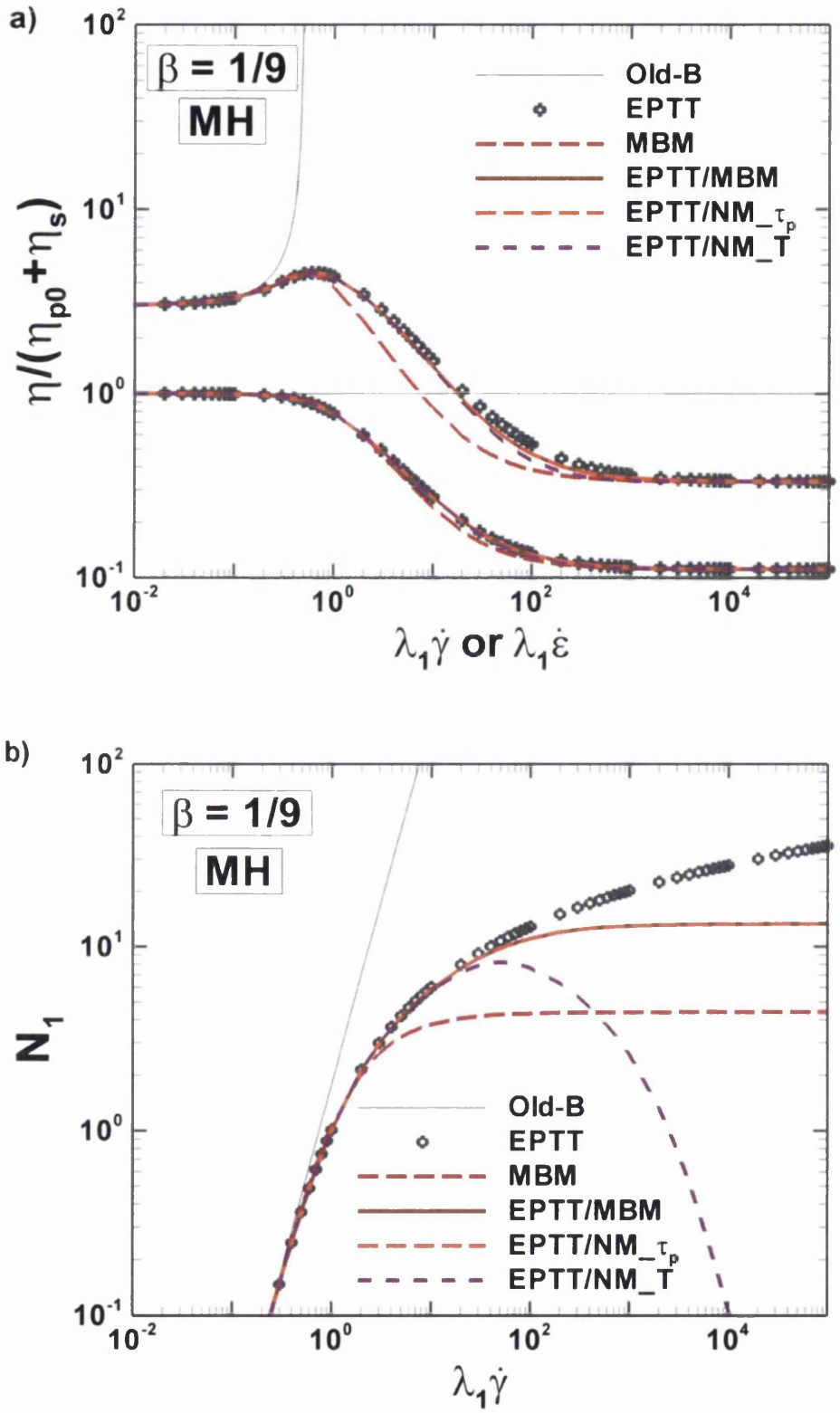

Figure4.2. Rheometrical functions versus *We*: EPTT, MBM and convoluted models; β**=1/9**; **MH**;
a) shear and extensional viscosity, b) shear N_1

Figure 4.3. Schematic diagram: rounded-corner hyperbolic 4:1:4 contraction-expansion geometry

a

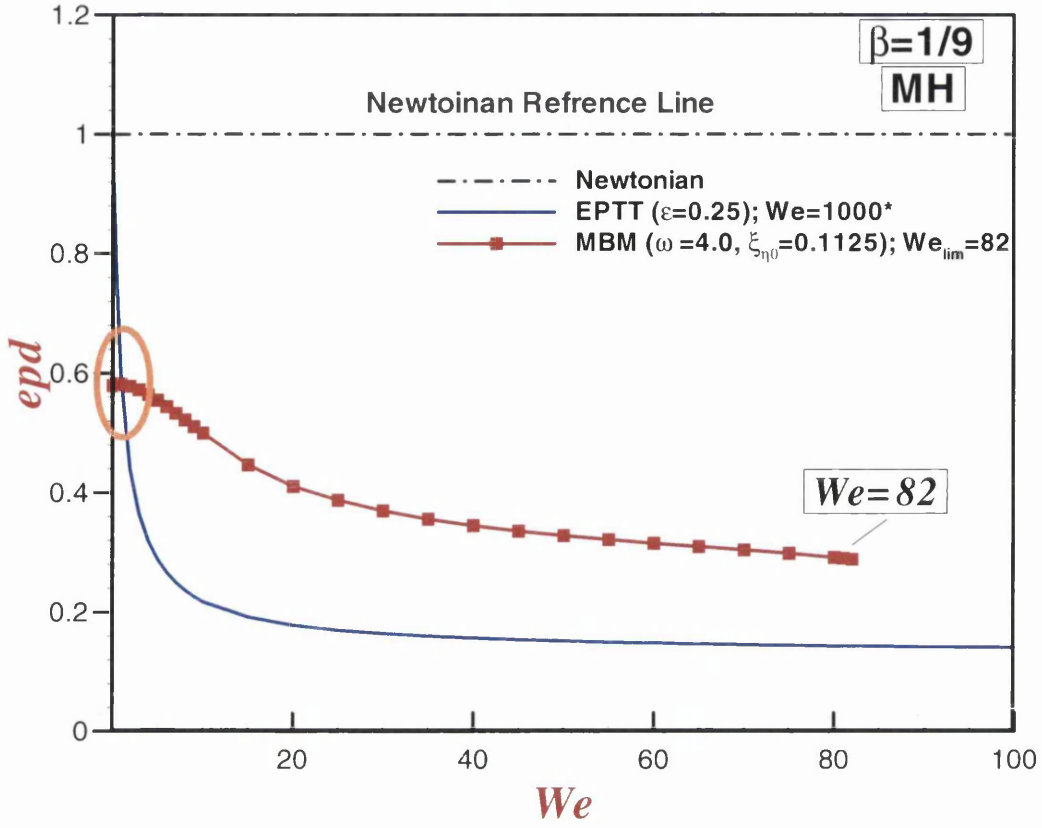

b

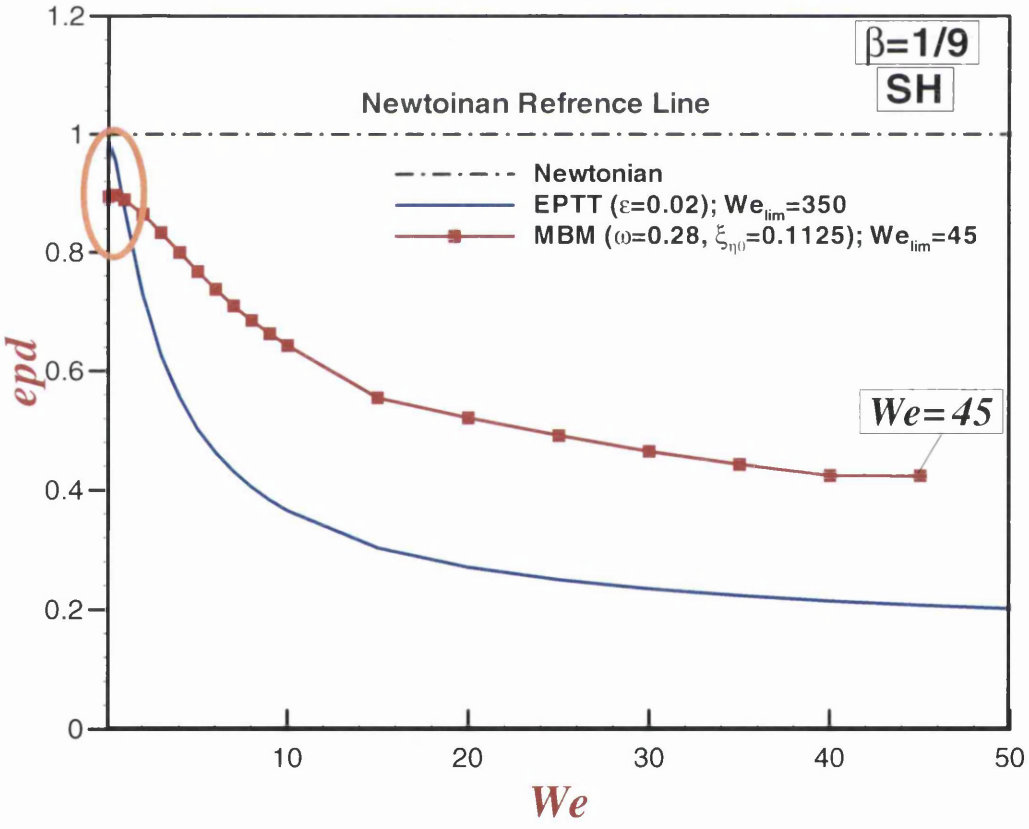

Figure 4.4. Excess pressure-drop (*epd*) vs. *We*; EPTT, Original MBM: a) moderate hardening response, b) strong hardening response; highly-polymeric (β=1/9)

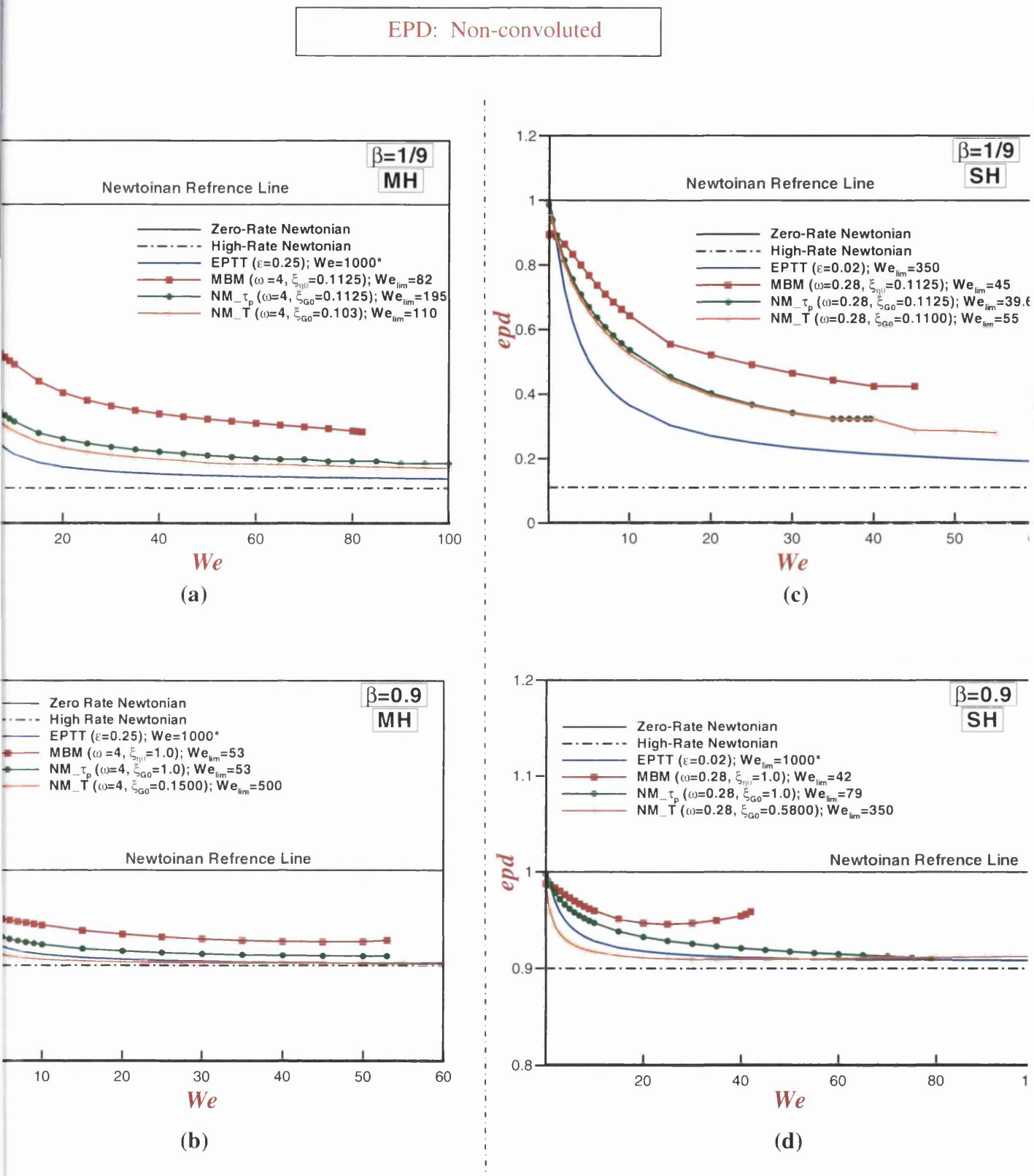

Figure 4.5. Excess pressure-drop (*epd*) vs. *We*; EPTT, Micellar-type (MBM, NM_τ_p and NM_T): **MH** response: a) β**=1/9**, b) β**=0.9**; **SH** response: c) β**=1/9**, d) β**=0.9**

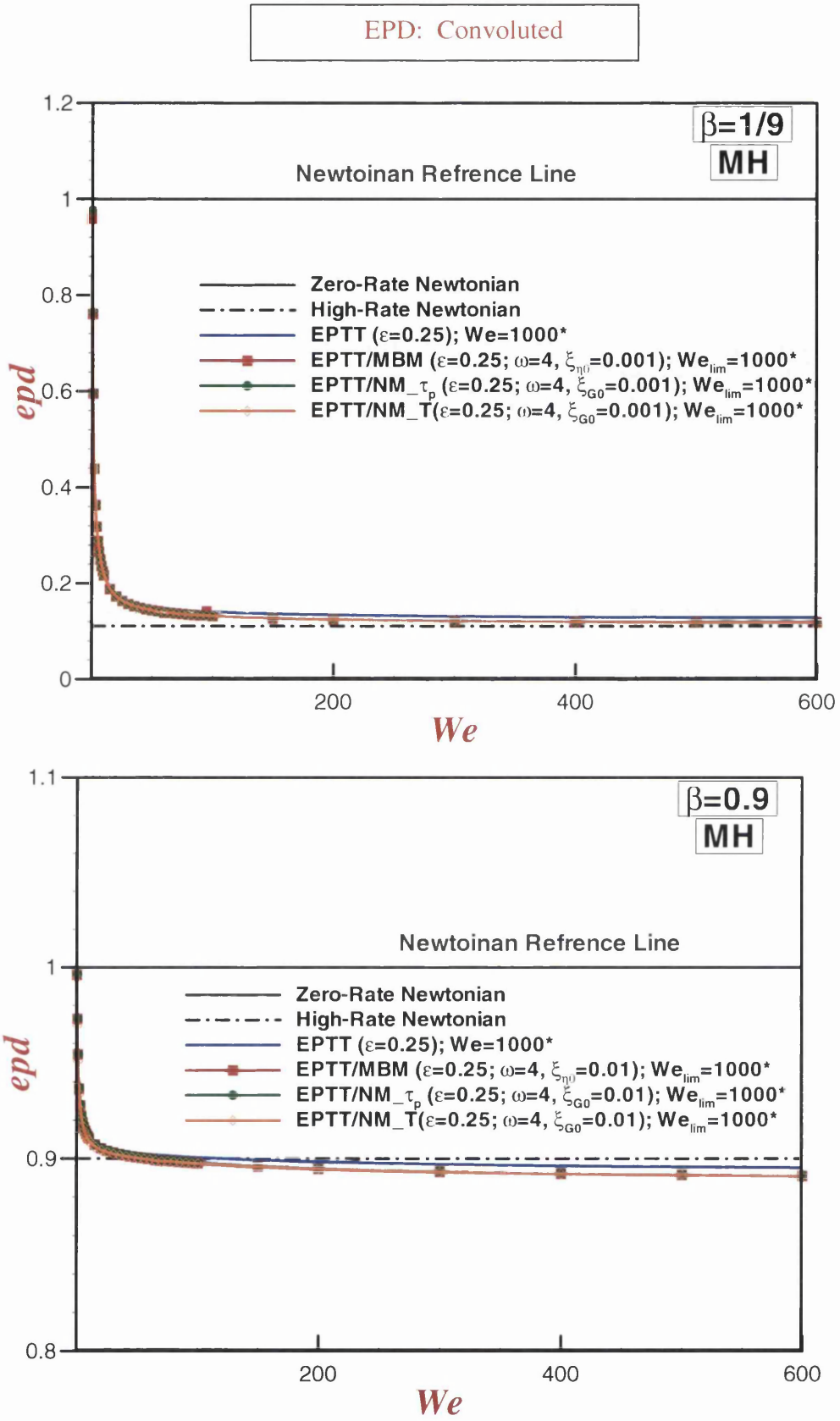

Figure 4.6. Excess pressure-drop (*epd*) vs. *We*; EPTT and convoluted models (EPTT/MBM, EPTT/ NM_τ_p and EPTT/ NM_T): a) highly-polymeric (β**=1/9**), b) solvent-dominated (β **=0.9**);

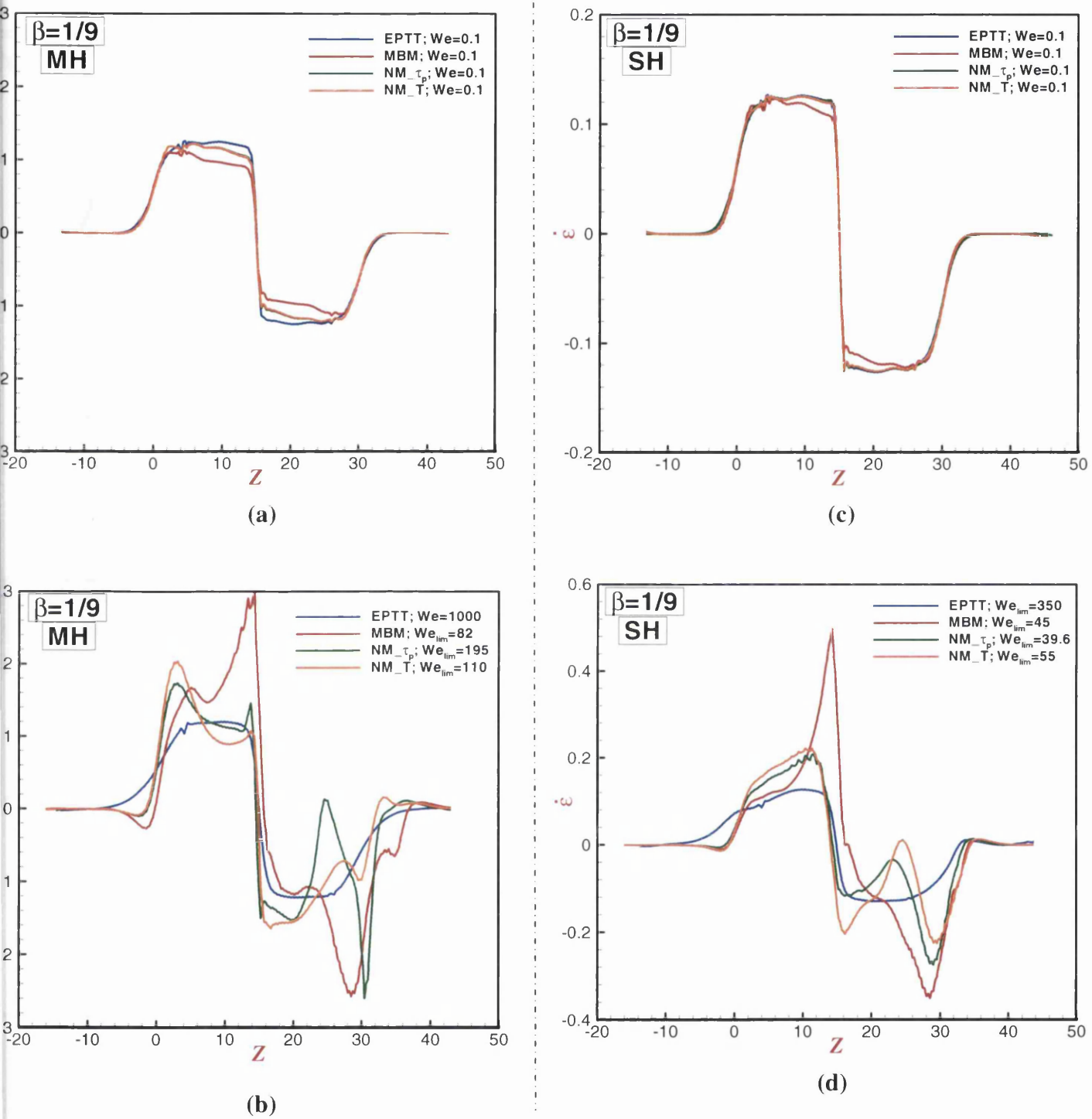

Figure 4.7. Strain rate profiles along symmetry line; EPTT, Micellar-type (MBM, NM_τ_p and NM_T): β**=1/9**; **MH** response: a) low *We*, b) high *We*; **SH** response: c) low *We*, d) high *We*

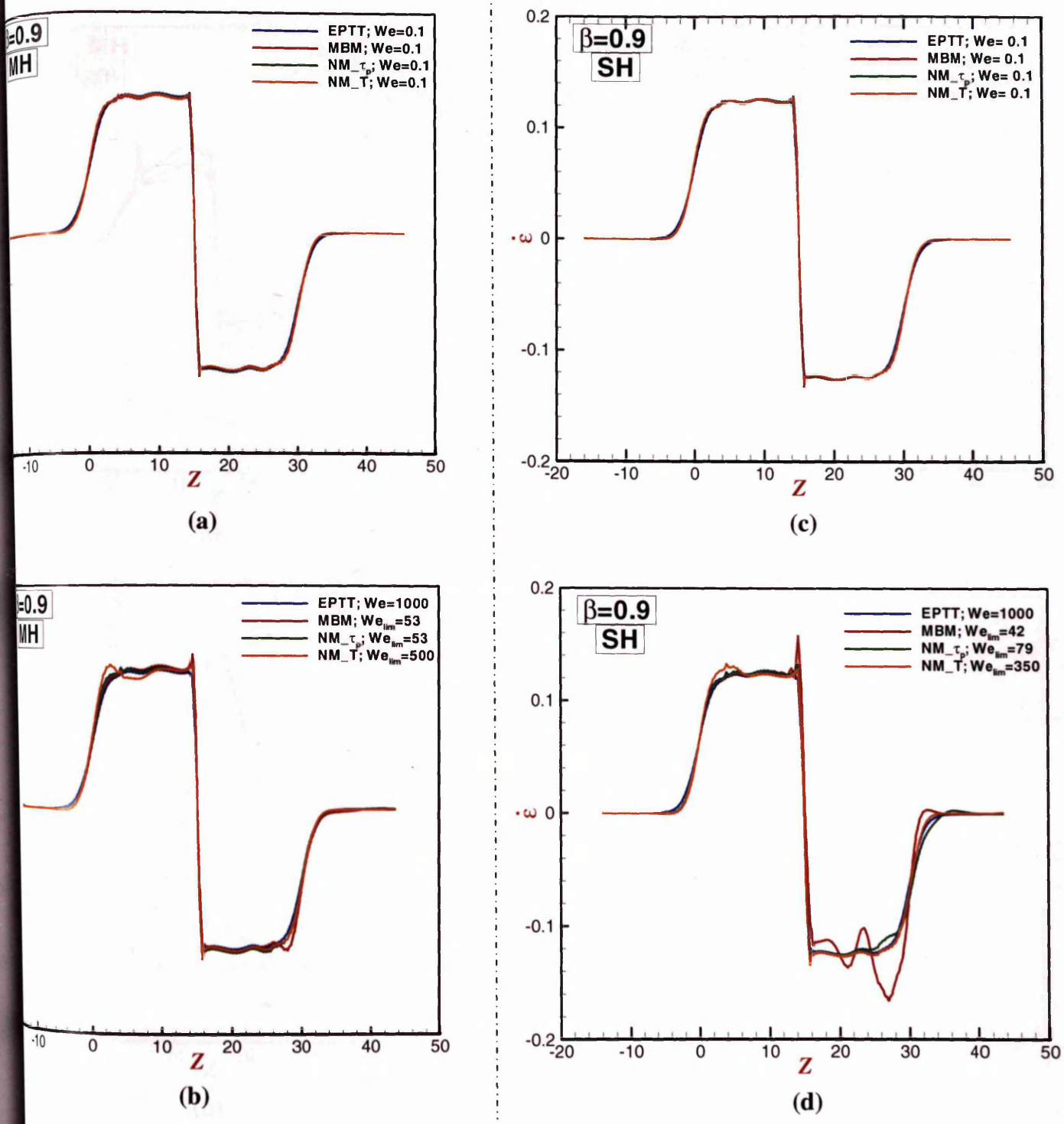

Figure 4.8. Strain rate profiles along symmetry line; EPTT, Micellar-type (MBM, NM_τ_p and NM_T): β**=0.9**; **MH** response: a) low *We*, b) high *We*; **SH** response: c) low *We*, d) high *We*

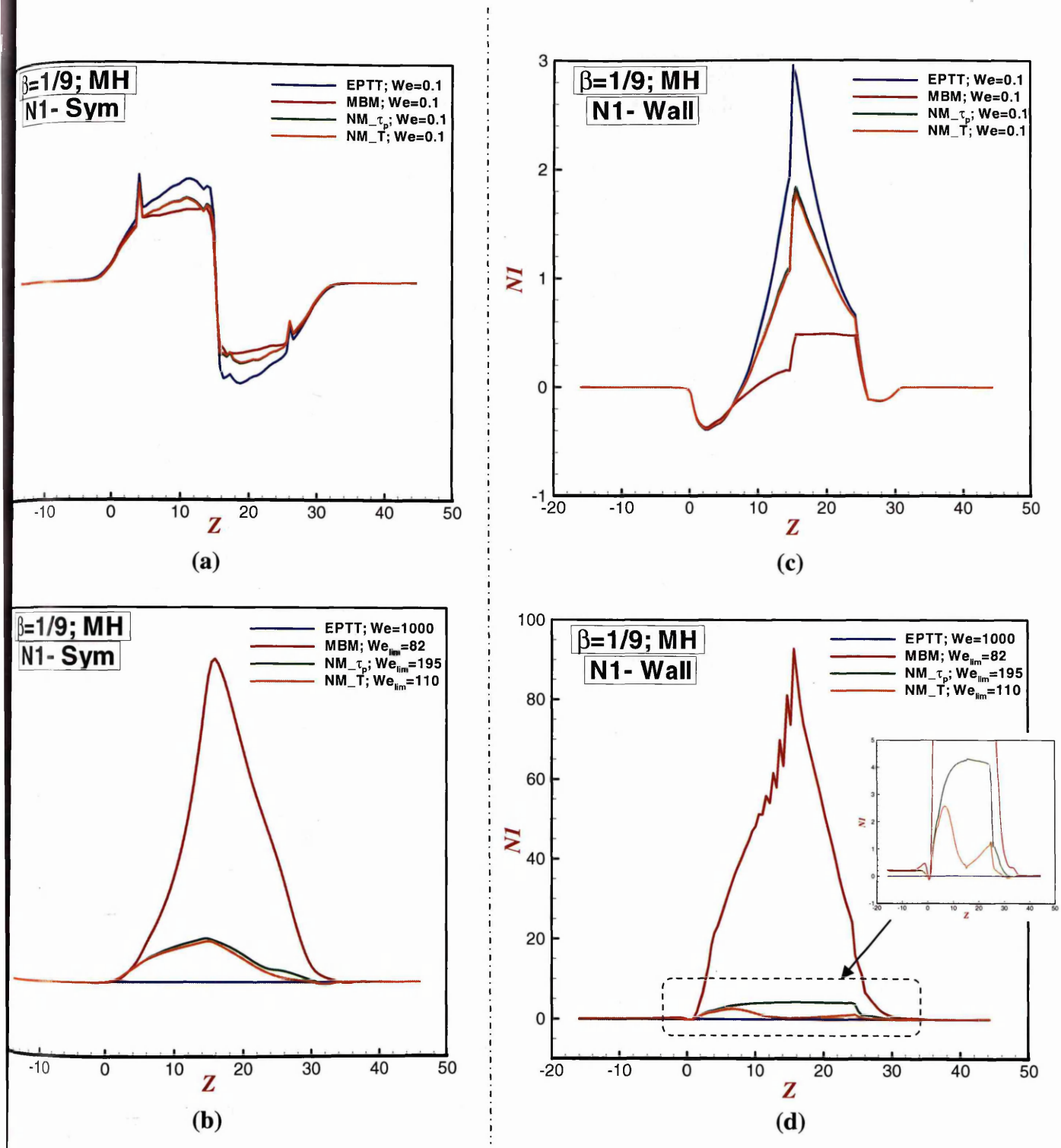

Figure 4.9. First normal stress difference (N_1) profiles; EPTT, Micellar-type (MBM, NM_τ_p and NM_T): $\boldsymbol{\beta}$**=1/9**; **MH** response; N_1 along symmetry line: a) low *We,* b) high *We;* N_1 along boundary wall: c) low *We,* d) high *We*

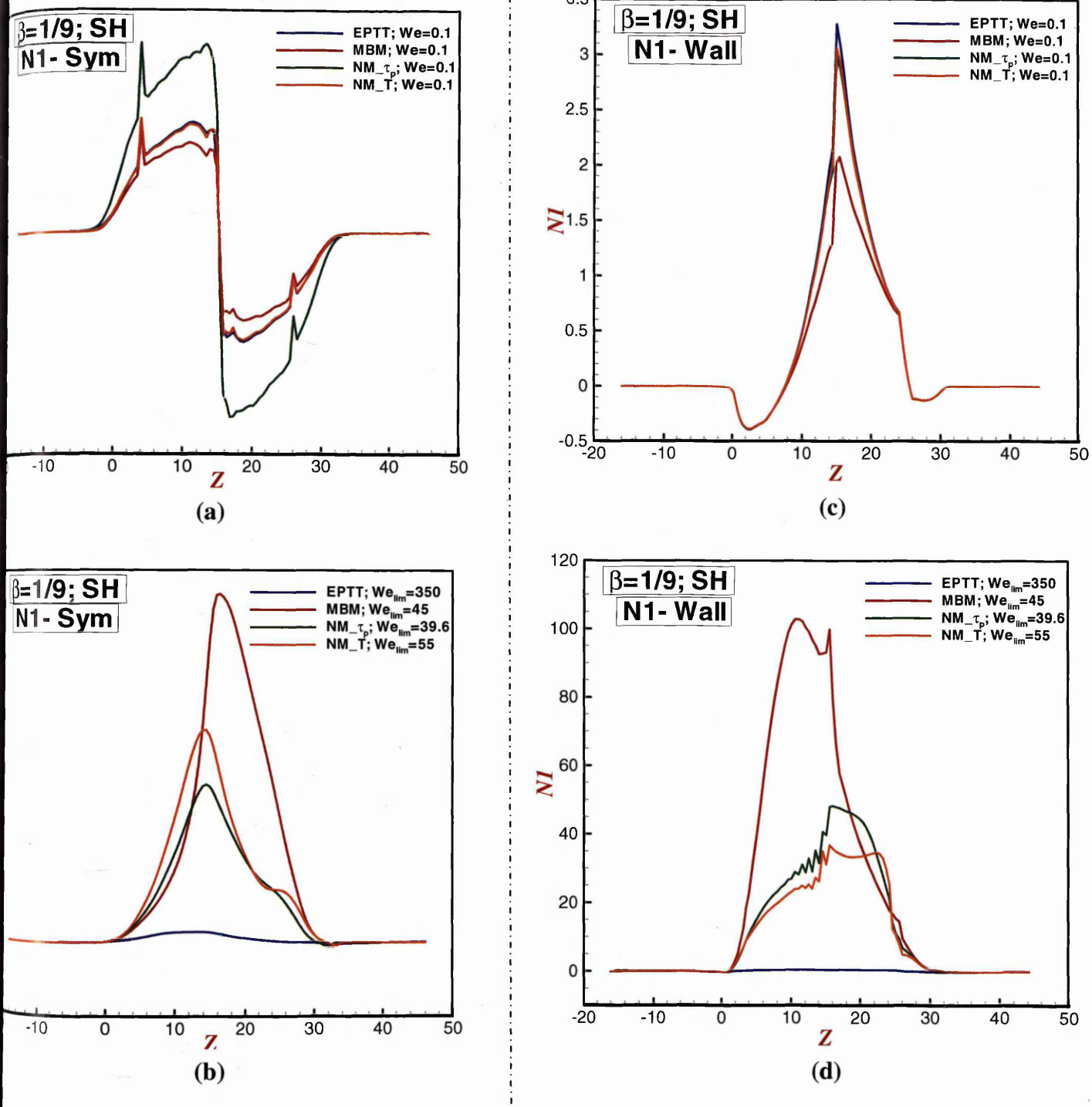

Figure 4.10. First normal stress difference (N_1) profiles; EPTT, Micellar-type (MBM, NM_τ_p and NM_T): β**=1/9**; **SH** response; N_1 along symmetry line: a) low *We,* b) high *We;* N_1 along boundary wall: c) low *We,* d) high *We*

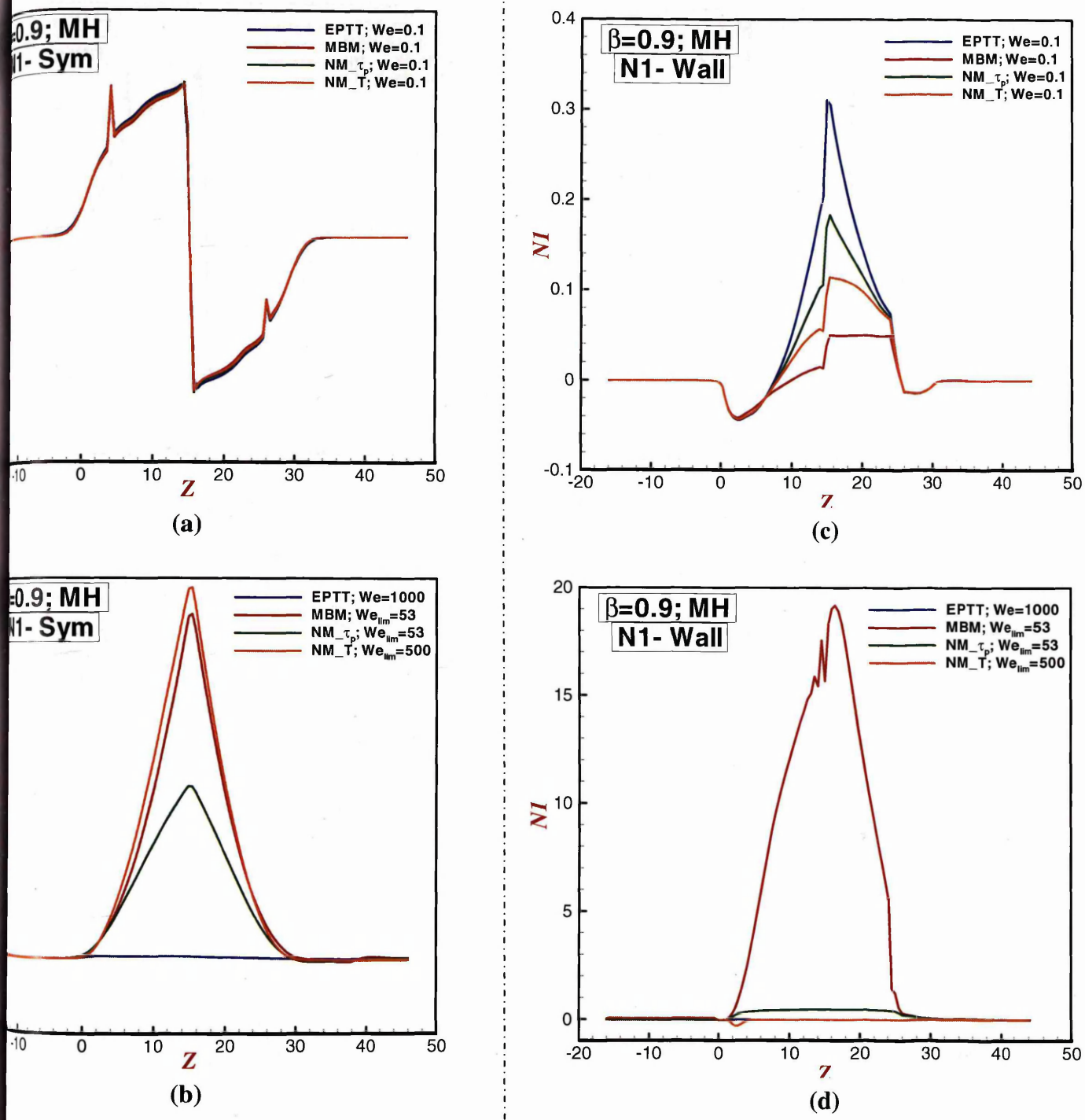

Figure 4.11. First normal stress difference (N_1) profiles; EPTT, Micellar-type (MBM, NM_τ_p and NM_T): β**=0.9**; **MH** response; N_1 along symmetry line: a) low *We,* b) high *We;* N_1 along boundary wall: c) low *We,* d) high *We*

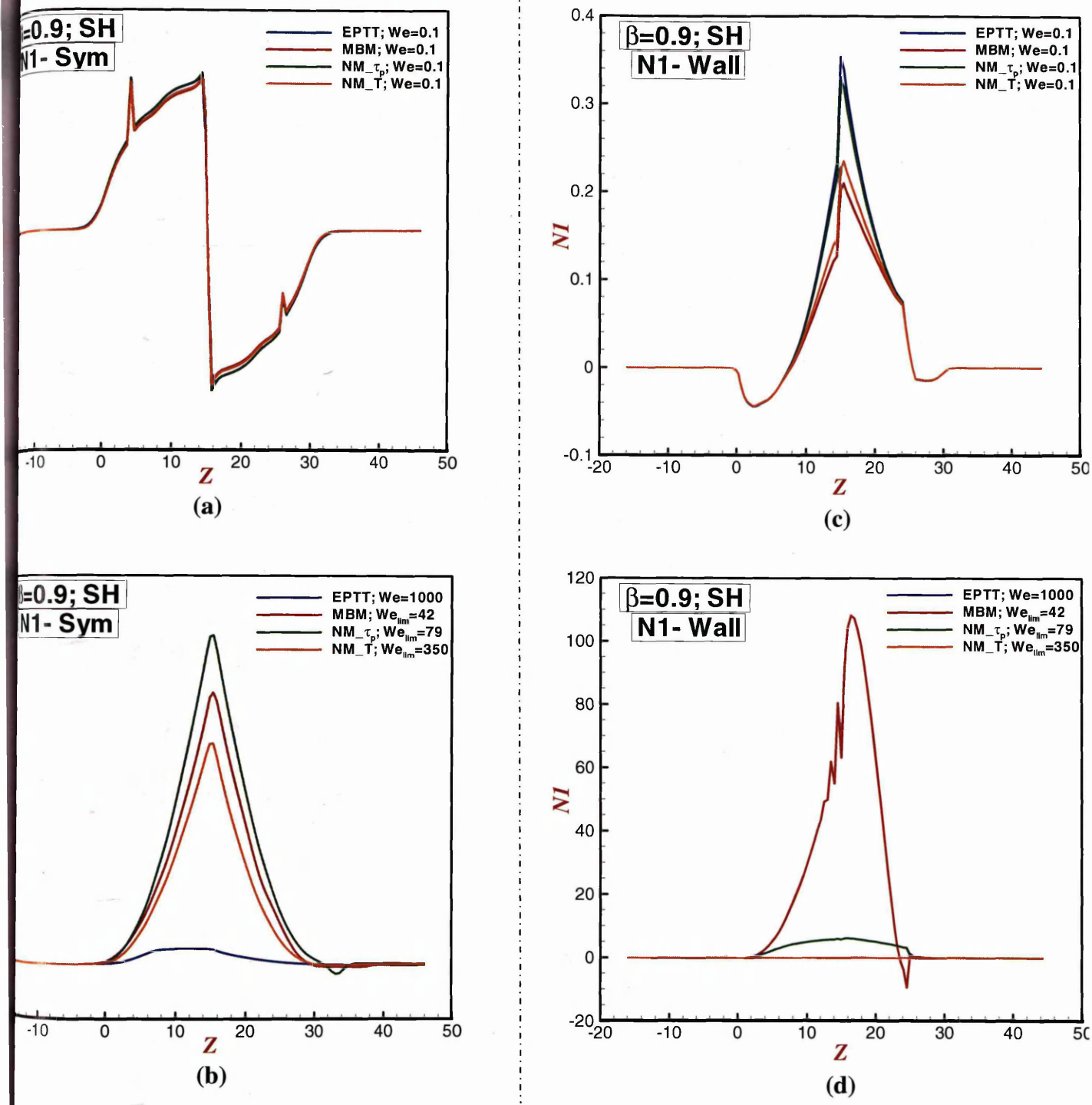

Figure 4.12. First normal stress difference (N_1) profiles; EPTT, Micellar-type (MBM, NM_τ_p and NM_T): β**=0.9**; **SH** response; N_1 along symmetry line: a) low *We,* b) high *We;* N_1 along boundary wall: c) low *We,* d) high *We*

The ultimate object is to measure something which we have already seen...to obtain a numerical estimate of some magnitude.

James Clerk Maxwell

Chapter 5

Rheological Characterization of Polymer Melts in Shear

In order to guarantee an improved processing performance one needs to appreciate and be able to control the rheology of the material within the indicated range. The knowledge of rheological behaviour of polymers (polymer melts of particular) is the key to set up an accurate process window, such as temperature and flow rates, and to the development of polymers (new materials) for smooth processing. Also, rheological information is required for process simulation, which is considered as an essential part of new process setup. Due to the sensitivity of the polymer melts to small changes of the polymer structure, using the rheometers in

linear range is a most convenient technique to rheologically characterize polymer melts.

This chapter presents the experimental work and characterisation results for three polymer-melts. This study focuses on the determination of the dynamic viscoelastic properties of High-Density Polyethylene (HDPE), Nylon 11 (Polyamide-PA11), and Poly-Vinylidene Fluoride (PVDF) melt. An advanced controlled-strain rheometer (TA Instruments ARES-G2) was used for the rheological measurements, with stationary upper-plate connected to the transducer (measuring stress/torque) and rotating lower-plate connected to the motor (applying strain or strain-rate). A uniform temperature was stablished during the experiments conducted by using a convection oven (designed for optimum temperature retention, rapid heating and cooling). This oven was mounted on either side of the test station. All the rheometrical tests were performed utilizing parallel plate geometry with plate-diameter 25mm and 1mm plate-gap separation.

The procedure followed for loading samples (in the form of pellets) into the rheometers was to place a guard-ring on top of the geometry. Then, the pellets were loaded into this ring, the oven was closed and heating activated up to the desired test temperature (220°C, 230°C, or 240°C). Shortly afterwards, the oven was opened and the guard-ring was removed, the gap was set and the normal force was observed. Finally, the sample was trimmed and the final gap was set.

Frequency sweep measurements were performed in a frequency range from 100 down to 0.1 rad/s with the strain level of 1% (in the linear regime) at temperatures of 220°C, 230°C, and 240°C, respectively. Using the Cox-Merz rule, dynamic oscillatory data (in terms of G', G'') were fitted to predictions according to the Cross model. The experimental data collected in this part of the study was used by others as characteristic material input-data to the same simulation software suite as used here (see [5.1]).

5.1 Determination of the Linear Viscoelastic Region [5.2]

In order to use Dynamic Mechanical Analysis (DMA) to accurately determine mechanical properties and develop morphological relationships, a polymeric material

must be deformed at amplitudes that lie within its linear viscoelastic (LVE) range. Then, within the LVE range (γ_L), material response is independent of the magnitude of the deformation and the material structure is maintained unbroken. At amplitudes larger than γ_L , the structure of the sample has either already been changed irreversibly, or is in fact completely destroyed. Characterization of the material within the linear regime yields a 'fingerprint' as to the structure of the polymer. Therefore, any differences in the structure of a polymer can easily be measured and interpreted through differences in the dynamic mechanical properties.

Special care should be paid when selecting the amplitude for a DMA test. The linear region can be measured for a particular material by employing an amplitude sweep test. In such a sweep test, the frequency is fixed and the amplitude is incrementally increased. To determine the LVE range, the storage modulus should be plotted against the amplitude, as the amplitude is the control variable in the DMA. To determine the extent and termination of the linear regime, a general rule-of-thumb is to locate the amplitude at which the initial value of the storage modulus changes by 5% (eg. the storage modulus at the lowest amplitude in the sweep).

When performing an amplitude sweep, the limiting value of the LVE range that is determined is valid only for the actual frequency used. Whilst performing the amplitude sweep tests, under various frequency conditions (i.e.10^2, 10, 1, and 0.1 rad/s), at the three required temperature levels (220, 230, 240° C), it became apparent that these polymers may be prone to some degree of thermal degradation, when temperatures are held for a sustained period of time (at low frequencies).

Since amplitude sweeps do not normally represent behaviour at rest, and hence, to evaluate a material in the rest-state, a frequency sweep should be performed and analysed at very low frequency values. Prior to testing samples of polymer melts and in order to avoid degradation for example, it is recommended to check thermal stability properties through the thermal stability time at the desired test temperature **(according to ISO 6721-10)**.

5.1.1 Determination of the Thermal Stability Time (Time Sweep)

A relatively straightforward test to determine if a system has time dependent rheological properties is an oscillatory time sweep. Thermal stability of all the polymer melts of interest (HDPE, PA11 and PVDF) was investigated under constant temperature and mechanical conditions. The thermal stability time is defined as that taken from the start of the test to the time station at which any of the measured values of complex shear modulus (G^*), storage modulus (G') and loss modulus (G'') have changed by as much as 5% from their initial values [5.2]. Once this time has been determined, any subsequent measurements on new specimens of the same sample at that identical temperature should be performed in a time shorter than the thermal stability time.

Using an oscillatory time sweep, both the frequency and the amplitude were kept at a constant level in each test. In this fashion, constant dynamic mechanical shear conditions are pre-set and ensured. In addition, the measuring temperature is also kept constant (isothermal conditions). The resulting thermal stability times for HDPE, PA11 and PVDF polymer melts, at the three desired temperatures, are recorded in Tables 5.1, 5.2, and 5.3, respectively. The total test time duration covers some 600 seconds.

? (rad/s)	100	10	1	0.1
220 C	Thermal independent	Thermal independent	Thermal independent	Thermal independent
230 C	Thermal independent	600 s	450 s	Under 300 s
240 C	Thermal independent	180 s	Between (88-106 s) ~90 s	--------

Table 5.1. Thermal stability time, HDPE melt
(According to ISO 6721-10)

ω (rad/s)	100	10	1	0.1
220℃	22 s	18 s	12 s	--------
230℃	16 s	17 s	--------	--------
240℃	13 s	8 s	--------	--------

Table 5.2. Thermal stability time, PA11 melt
(According to ISO 6721-10)

ω (rad/s)	100	10	1	0.1
220℃	Thermal independent	Thermal independent	Thermal independent	Thermal independent
230℃	Thermal independent	Thermal independent	Thermal independent	Thermal independent
240℃	Thermal independent	Thermal independent	Thermal independent	Thermal independent

Table 5.3. Thermal stability time, PVDF melt
(According to ISO 6721-10)

At low frequencies and high temperatures, both first (HDPE and PA11) polymers were prone to lower thermal stability times. In the case of the PA11 melt, given in Table 5.2, degradation occurs rather rapidly. The major difficulty at lower frequencies is that the experimental determination time for a single data point is large, rendering reliable and reproducible experimental data difficult to obtain. The data for PVDF would indicate little to no degradation during the tests (of time duration 600s) and excellent resistance to temperature change.

5.1.2 Determination of Time Dependent Shear Behaviour (Frequency Sweep)

Frequency sweeps are oscillatory tests performed at variable frequencies, whilst maintaining the amplitude (and the measuring temperature) at a constant level. Frequency sweeps are used to investigate time-dependent shear behaviour, since frequency is inversely related to time. Short-term behaviour is detected by rapid motion (i.e., at high frequencies) and long-term behaviour by slow motion (i.e., at low frequencies).

Thus, the dynamic response of a material may be monitored and evaluated by systematically selecting the appropriate conditions and range of parameters for all three quantities of: the control variable (a value of strain found within the linear viscoelastic regime), the frequency and the temperature of interest.

In this manner, frequency sweep tests provide the storage and loss modulus, G' and G''. In order to limit the effect of degradation, the frequency sweeps started at 100 rad/s and decreased subsequently. Only data down to about 0.1 rad/s (for HDPE and PVDF melts) and 1 rad/s (for PA11 melt) is considered to be reliable, and only that has been used in the data fitting performed below.

The method of taking data in a few intervals of frequency has been suggested to avoid problems with either long exposure time at high temperature, or with taking data in a time shorter than the thermal stability time. This approach allows for a small improvement in precision under the data acquisition. The data thus obtained has been interpreted in terms of the shear viscosities, as presented in Figures 5.1-5.3 for the HDPE melt. It is fairly apparent that a significant improvement in precision has been obtained at higher temperatures and lower frequencies.

From Figure 5.4 it can be observed that in the case of the PA11 melt, the viscoelastic properties cannot be investigated by a discrete frequency-sweep, since the substance is changing dramatically during the measurement. This renders a meaningful status description almost impossible. An alternative procedure is to speed-up the data acquisition time – known as a Multiwave test, whereby investigating the frequency dependency proves to significantly shorten the measuring time.

The Multiwave principle is based on a pre-set basic sine wave and higher frequencies modulated about that specification. Multiwave oscillation is an enhanced version of the conventional (single frequency) oscillation mode, which allows the sample material to be exposed simultaneously to multiple oscillatory frequencies. Notably, as these multiple oscillations pass through the material, they act independently of each other. As a result, the accumulated strain present in the material is the sum of the strains caused by each of the individual oscillations. (Note: the total resultant strain must lie within the materials linear viscoelastic region)[5.2].

From the outset, Multiwave measurements were made on the basic sine wave (ω=0.1 rad/s), and eight harmonic multiple sine waves were modulated about this basic value. This generated a total of nine logarithmically equidistant frequencies over two decades, to be used in the evaluation procedures. Such a test protocol reduced the measuring time from 600s to 126s; hence, offering a considerable time saving over the traditional frequency sweep test. The pre-set strain levels were selected for the Multiwave measurements so that the resulting deformations stayed within the range of 0.1 and 1% (γ=0.05%). Figure 5.5 illustrates the frequency dependency of the dynamic complex viscosity η^* during such measurements, which evidences rapid dynamic change in the response of the material. Also, the results from the frequency sweeps for the PVDF melt, in terms shear-viscosity (η^*) are provided in Figures 5.6.

In terms of the G' and G'' data, the findings for HDPE, PA11 and PVDF melts are displayed in Figures 5.7(a,b), 5.8(a,b) and 5.9(a,b), respectively. Here, in order to fit the data, one assumes that a temperature dependent discrete relaxation spectrum λ_i (T) exists, defined by:

$$G'(\omega,T)=\sum_{i=1}^{N}\frac{g_i\omega^2\lambda_i^2}{(1+\omega^2\lambda_i^2)}\,, \tag{5.1}$$

and

$$G''(\omega,T)=\sum_{i=1}^{N}\frac{g_i\omega\lambda_i}{(1+\omega^2\lambda_i^2)}\,, \tag{5.2}$$

where T represents the temperature (^{O}K) and g_i the elastic modulus (independent of temperature) correspond to λ_i . In addition, one may assume that the temperature dependence satisfies the time-temperature superposition principle, which enhances the accessible frequencies of the linear viscoelastic experiment. As such, the relaxation spectrum may be represented as:

$$\lambda_i(T) = a_T \lambda_i(T_0), \tag{5.3}$$

where T_0 is a reference temperature and a_T is a temperature-dependent shift factor. For simplicity, the shift factor is taken to conform to the common Arrhenius relationship:

$$a_T = e^{\frac{E}{R}\left(\frac{1}{T}-\frac{1}{T_0}\right)}, \tag{5.4}$$

where E is the activation energy (ev) and R is the universal gas constant (ev/K), T is the measurement temperature (^{O}K), T_0 is a reference temperature (^{O}K) and a_T is a time-based shift factor.

Thus, the fitting procedure consists of the following three steps:

1) Choose a reference temperature, T_0. In this study, 220°C (493°K) is used.
2) Determine $g_i, \lambda_i(T_0)$ by fitting the storage and loss moduli at the reference temperature, T_0, to equations (1) and (2). Six relaxation modes for HDPE, and five relaxation modes for PA11, PVDF provide a reasonable fit to the data.
3) Determine the parameter E/R in order to fit the data across other temperatures.

The resulting { g_i, λ_i } parameter sets for HDPE and PA11 melts are found to be:

	HDPE	
E/R (K)	2662	
Relaxation	g (Pa)	λ (s)

mode		
1	220100	3.58E-03
2	57104.1	0.0242068
3	25841.9	0.111604
4	10974.7	0.509666
5	4358.59	2.41874
6	1910.91	15.5448

PA11

E/R (K)	1646	
Relaxation mode	g (Pa)	λ (s)
1	587407	1.00E-03
2	57231.9	0.013587
3	16626	0.051046
4	8887.59	0.173783
5	4270.75	1.11918

PVDF

E/R (K)	9318	
Relaxation mode	g (Pa)	λ (s)
1	281530	7.11E-03
2	98957.6	0.0595669
3	50448.6	0.397239
4	24545.4	2.64045
5	13982.1	24.9029

5.2 Viscosity Measurements of Polymer Melts

For many polymers the Cox-Merz viscosity is a reliable indicator of the steady shear viscosity. An empirical relationship, termed the Cox-Merz rule, states that the

shear rate dependence of the steady state viscosity $\eta(\dot{\gamma})$ is equal to the frequency dependence of the complex viscosity $\eta^*(\omega)$, that is: $\eta(\dot{\gamma}) = |\eta^*(\omega)|$.

The usefulness of this rule, which holds well for most conventional polymers, is that while steady measurements of shear viscosity are virtually impossible for shear rates larger than $5s^{-1}$ with rotational instruments, dynamic measurements can easily be conducted up to 500 rad/s (corresponds to shear rate of $500s^{-1}$) or even higher. Thus, the full range of viscosity needed in extrusion may be covered.

The Cox-Merz rule shows excellent agreement with the oscillatory data obtained for both HDPE and PA11 polymers at 220° C and this agreement is reasonable for PVDF melt at 220° C. These data on shear viscosity are presented for HDPE, PA11 and PVDF in Figures 5.10, 5.11 and 5.12, respectively. Rheometrical equipment was not available to provide extensional viscosity data for these melts; yet much may be gathered from shear viscosity trends and levels and by cross-reference to the initial findings on PVDF, PA11 and PVDF melts.

5.2.1 Flow Data Modelling: Viscosity model for shear-thinning polymer melt

For quantitative analysis purposes, a mathematical model fit is performed to the results of the oscillatory experiments. Many commercial software packages contain curve-fitting procedures to perform this function, but a reliable model should provide both a reasonable fit to the data (in some measurable sense), and be physically realistic.

Various different models are commonly used to describe the flow behaviour of shear-thinning fluids. By fitting such a model to the experimental data set, the flow behaviour can be predicted over a wider range of shear rates than that used solely in the experimental range. Amongst such models, the *Cross model* is a suitable candidate of choice, capable of describing a constant zero shear-rate Newtonian viscosity plateau, a shear thinning viscosity, and also a transition zone between them; whilst avoiding the specification of a second limiting Newtonian plateau level at high shear-rates:

$$\eta(\dot{\gamma}) = \frac{\eta_0}{1+(\lambda\dot{\gamma})^{1-m}}, \qquad \text{Cross Model} \qquad (5.5)$$

with fitting parameters: η_0 a zero shear-viscosity, m a Power-law index, and λ a characteristic material time.

As a final observation, it should be noted that the oscillatory data cannot be represented by a single relaxation time with any reasonable accuracy. However, a pseudo-relaxation time λ may be defined by fitting the shear viscosity to a model such as the Cross model.

To be consistent with the oscillatory data, it is not unreasonable to adopt the value of the zero-shear viscosity, η_0, as:

$$\eta_0 = \sum_{i=1}^{N} g_i \lambda_i , \qquad (5.6)$$

Then, appropriate parameters derived for HDPE, PA11 and PVDF melts are:

Parameters	HDPE	PA11	PVDF
η_0 (Pa.s)	50900	8540	441000
m	0.43	0.40	0.34
λ (s)	4.91	0.28	18.04

These data are included in Figures 5.10, 5.11 and 5.12, respectively.

References

[5.1] A, Al-Muslimawi, H.R. Tamaddon-Jahromi and M.F. Webster, *Numerical computation of extrusion and draw-extrusion cable-coating flows with polymer melts.* Appl. Rheol. **24** (2014) 34188. DOI: 10.3933/ApplRheol-24-34188

[5.2] T.G. Mezger, *The Rheology Handbook: for users of rotational and oscillatory rheometers*, Vincentz Network, Hannover (2006).

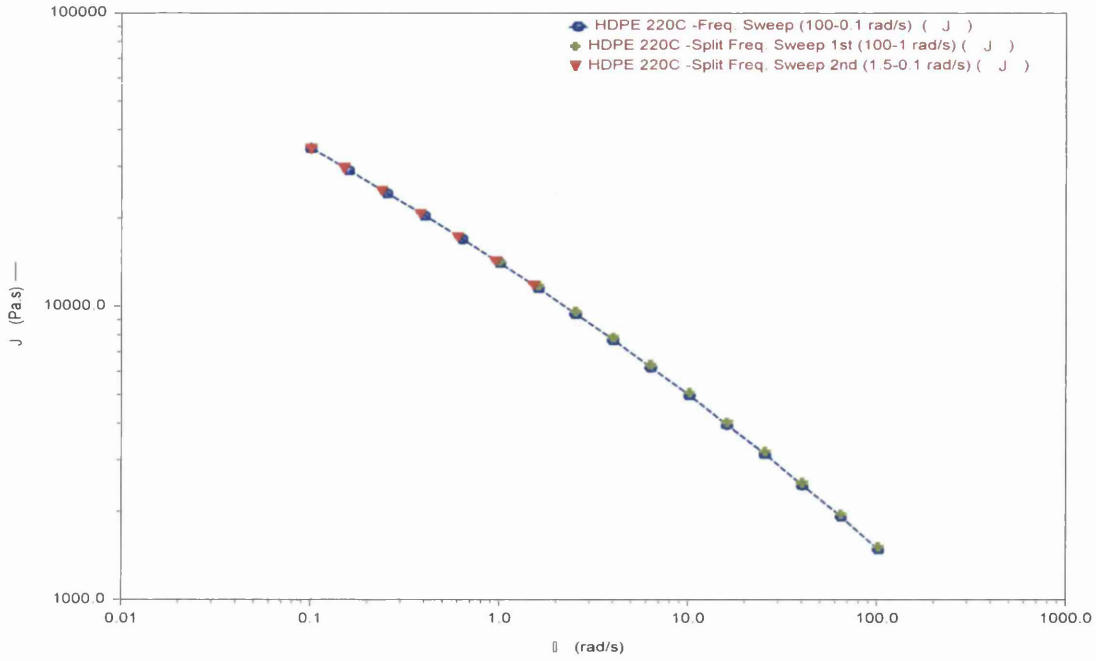

Figure 5.1. Shear viscosity vs. Angular frequency
Measuring results for Freq. Sweep and Split Freq. Sweep
HDPE at 220 °C

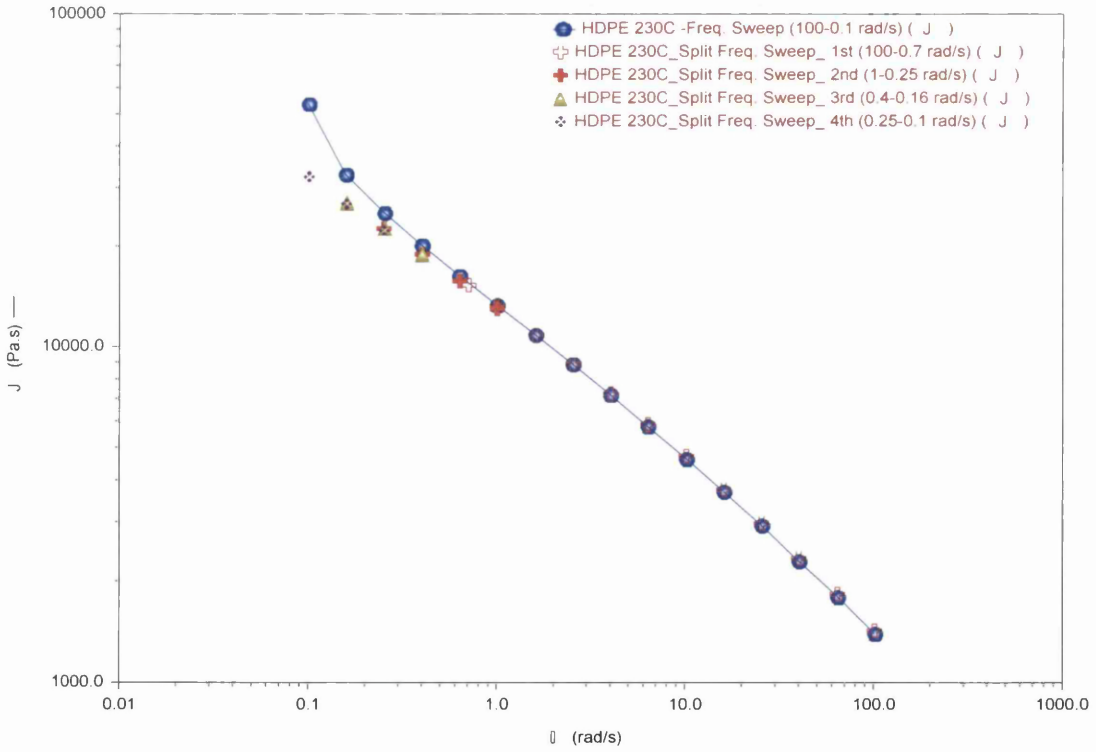

Figure 5.2. Shear viscosity vs. Angular frequency
Measuring results for Freq. Sweep and Split Freq. Sweep
HDPE at 230 °C

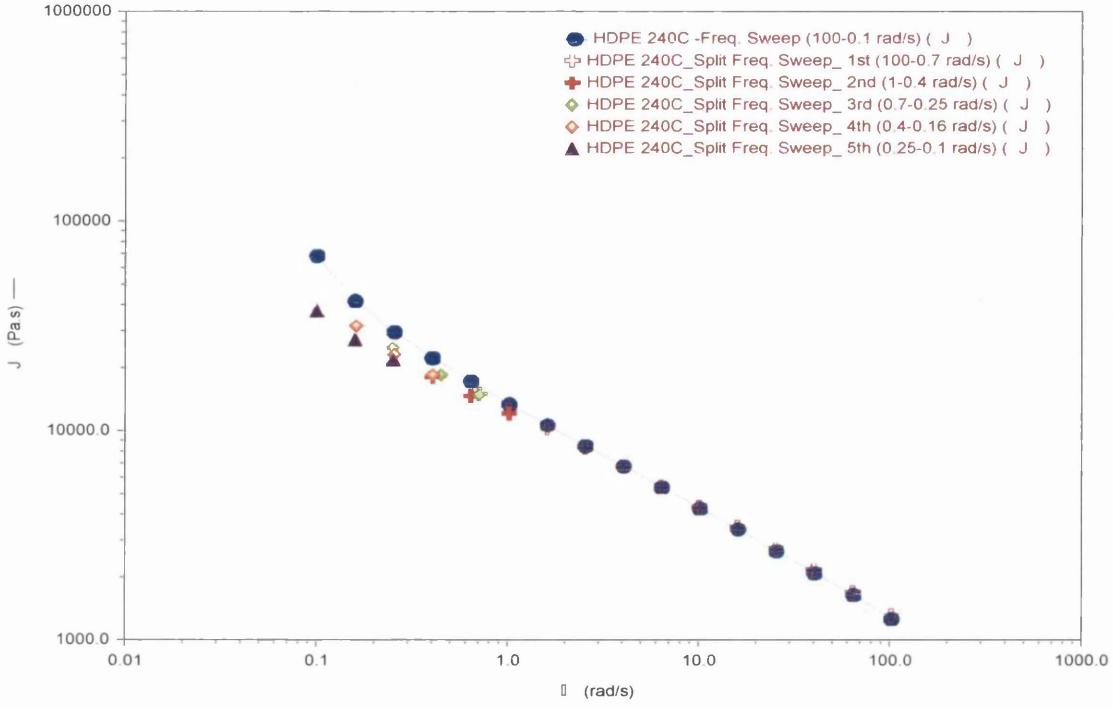

Figure 5.3. Shear viscosity vs. Angular frequency
Measuring results for Freq. Sweep and Split Freq. Sweep
HDPE at 240 °C

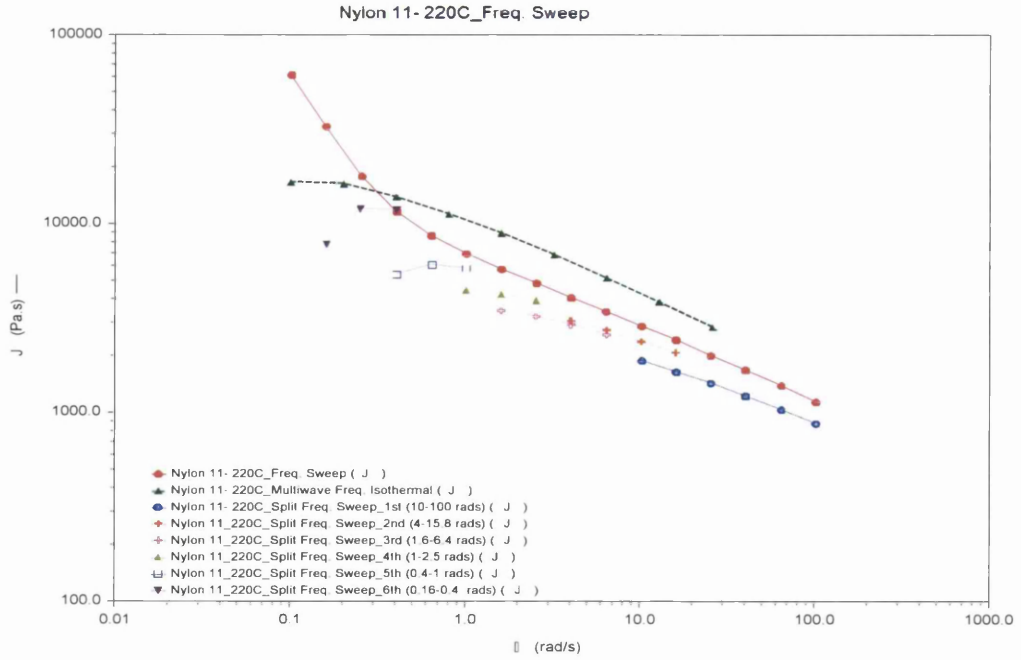

Figure 5.4. Shear viscosity vs. Angular frequency
Measuring results for Freq. Sweep and Split Freq. Sweep
PA11 at 220 °C

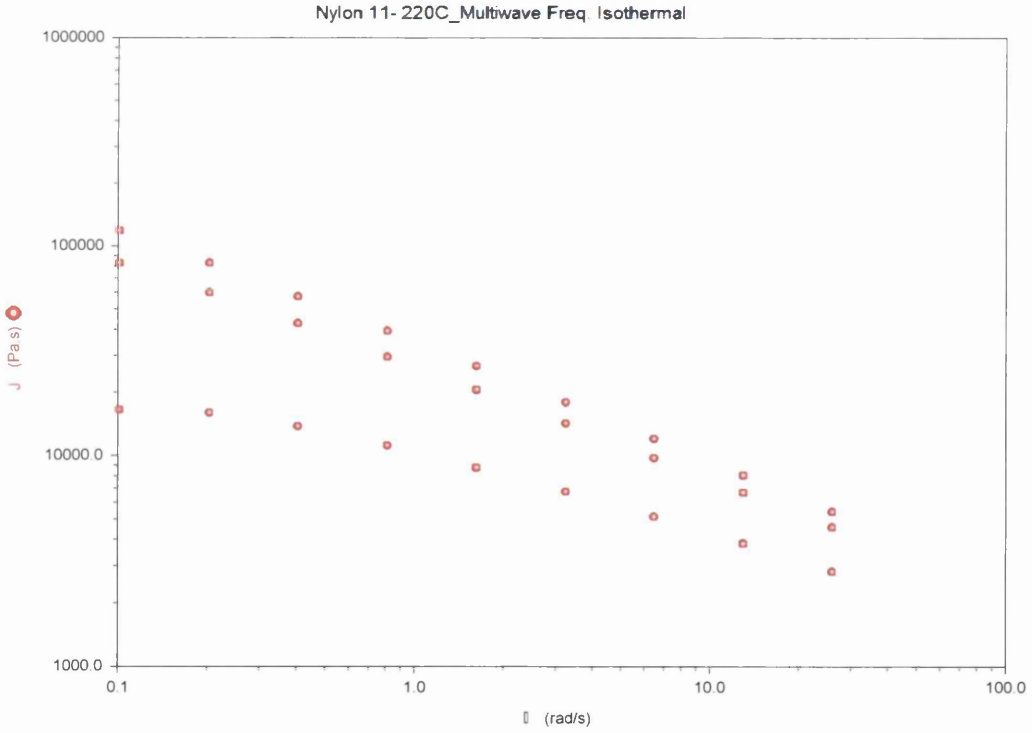

Figure 5.5. Shear viscosity vs. Angular frequency
Measuring results from Multiwave measurements
PA11 at 220 °C

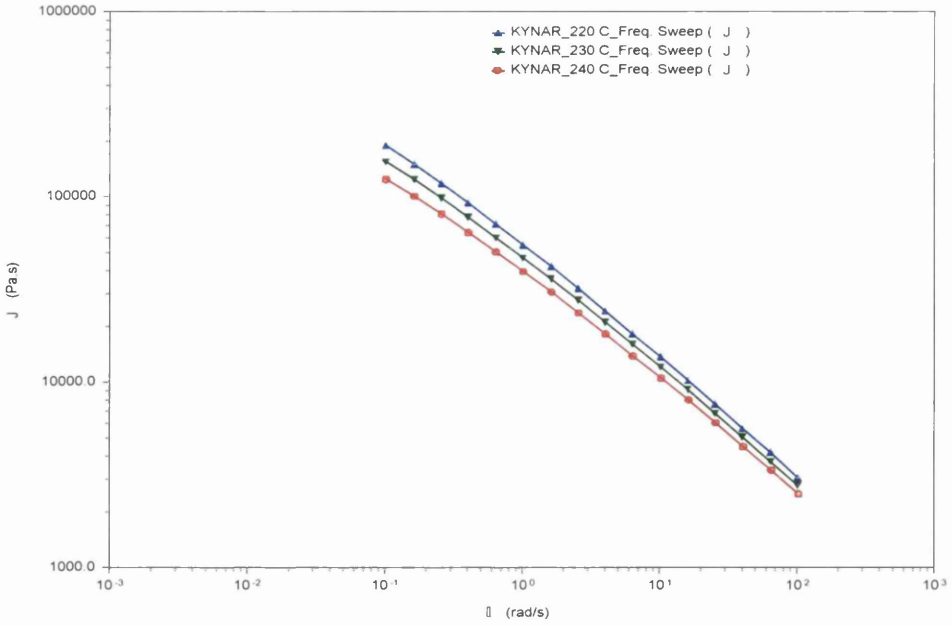

Figure 5.6. Shear viscosity vs. Angular frequency
Measuring results for Freq. Sweep
PVDF at three desired temperature (220- 240 ^{o}C)

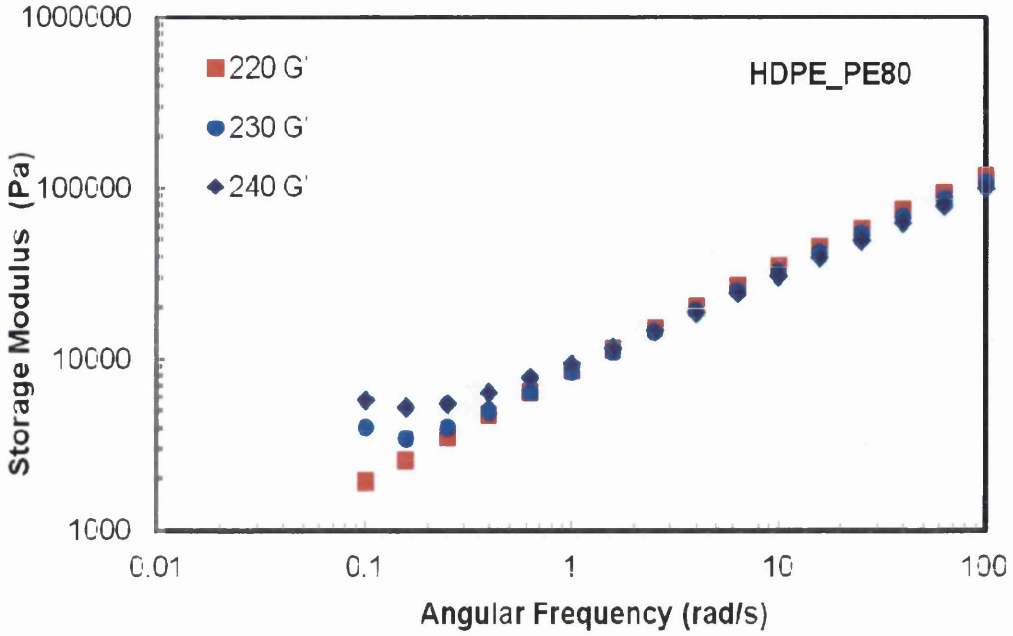

Figure 5.7a. Storage modulus vs. Angular frequency
Measuring results for Freq. Sweep
HDPE at three desired temperature (220- 240 °C)

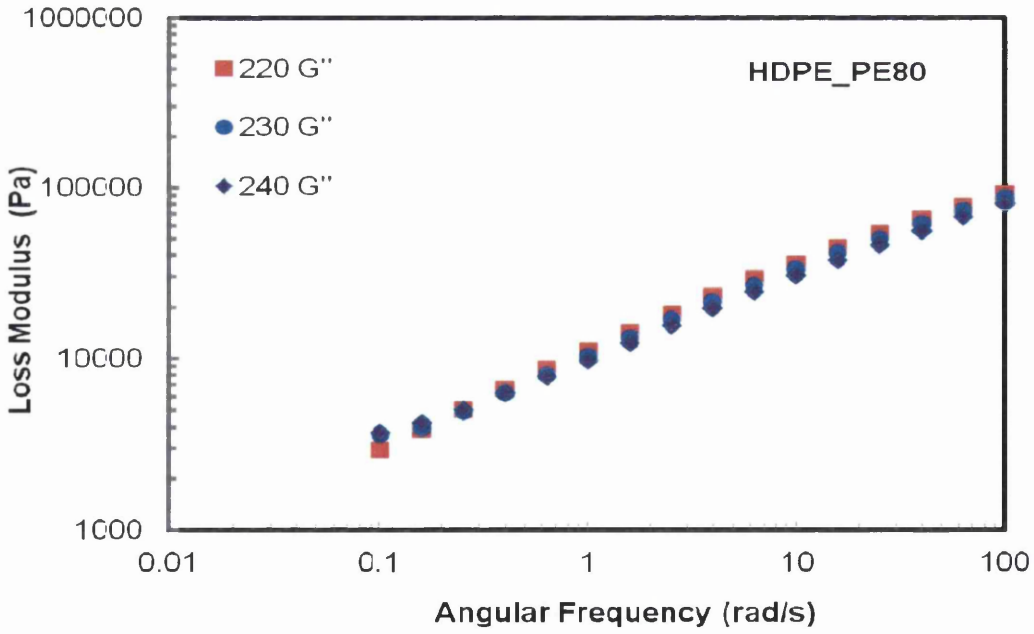

Figure 5.7b. Loss modulus vs. Angular frequency
Measuring results for Freq. Sweep
HDPE at three desired temperature (220- 240 °C)

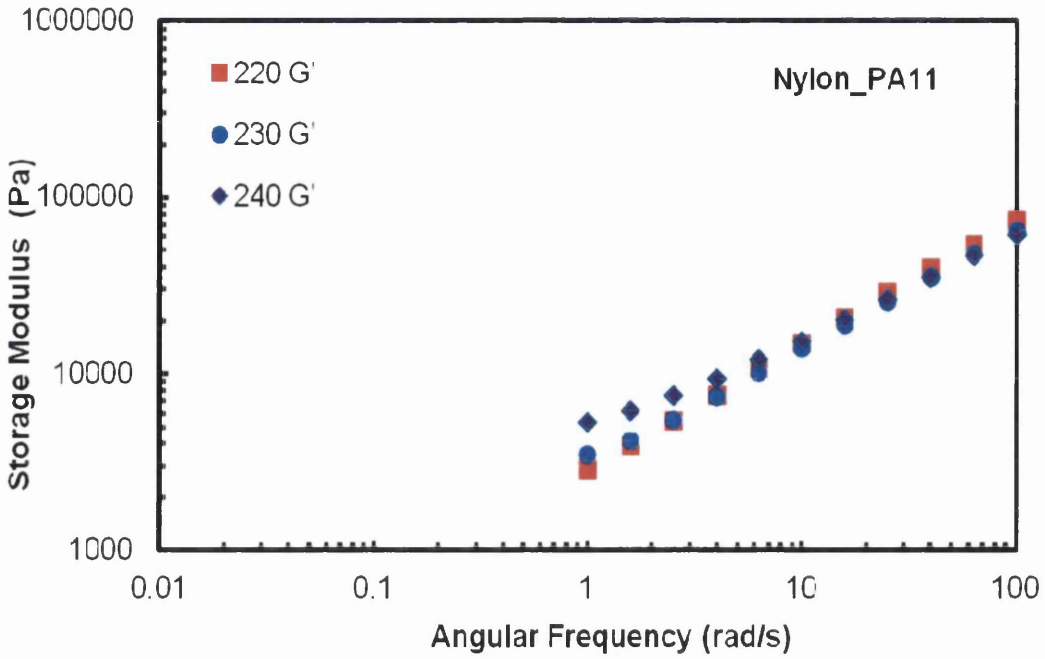

Figure 5.8a. Storage modulus vs. Angular frequency
Measuring results for Freq. Sweep
PA11 at three desired temperature (220- 240 °C)

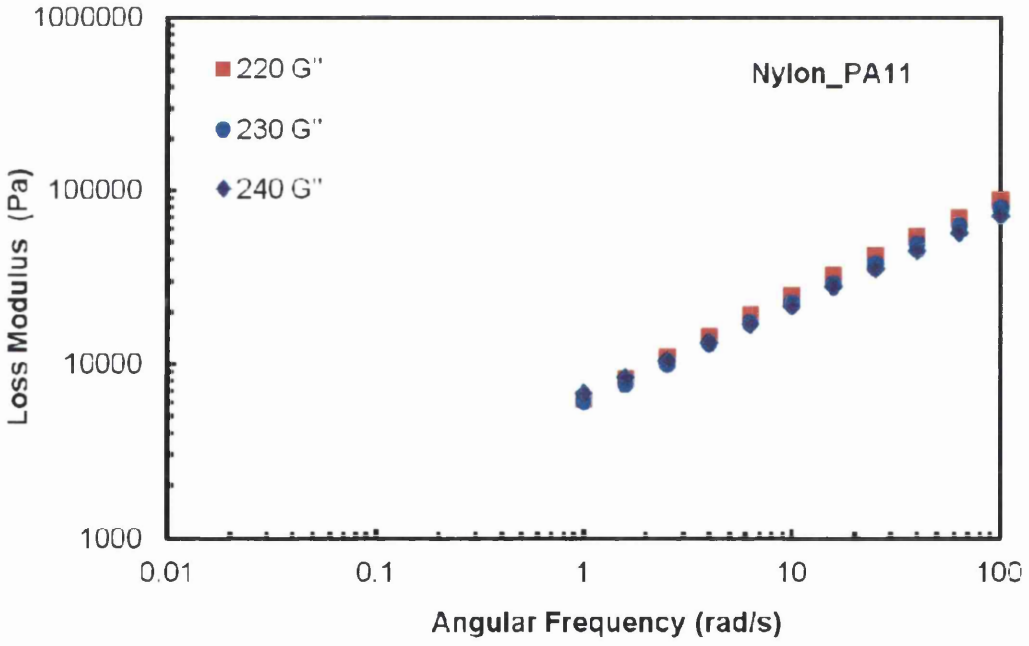

Figure 5.8b. Loss modulus vs. Angular frequency
Measuring results for Freq. Sweep
PA11 at three desired temperature (220- 240 °C)

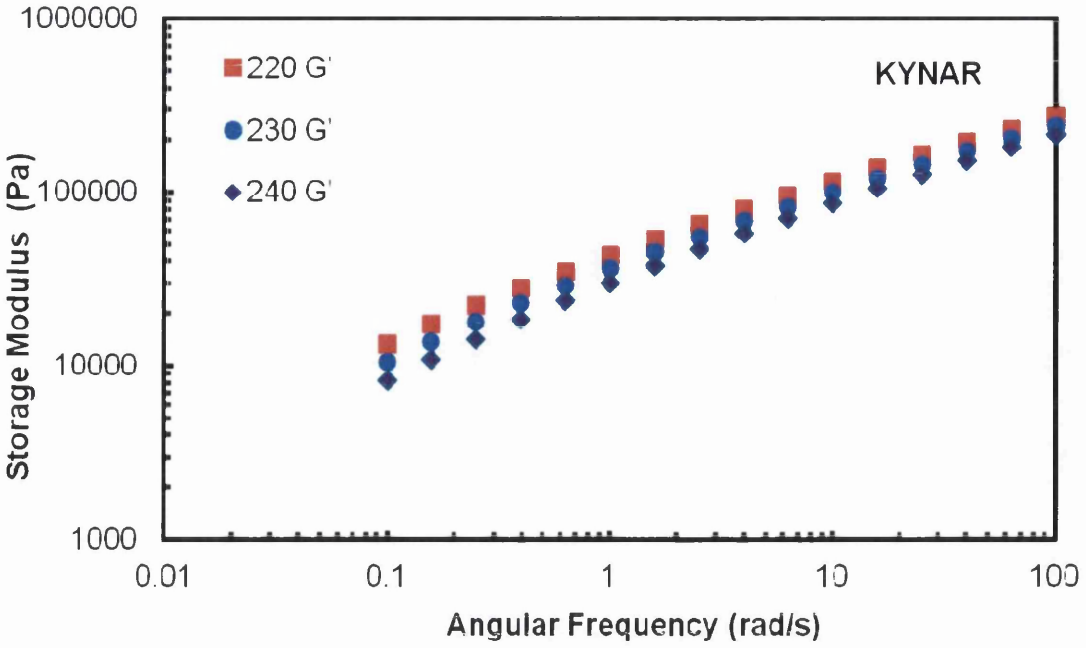

Figure 5.9a. Storage modulus vs. Angular frequency
Measuring results for Freq. Sweep
PVDF at three desired temperature (220- 240 °C)

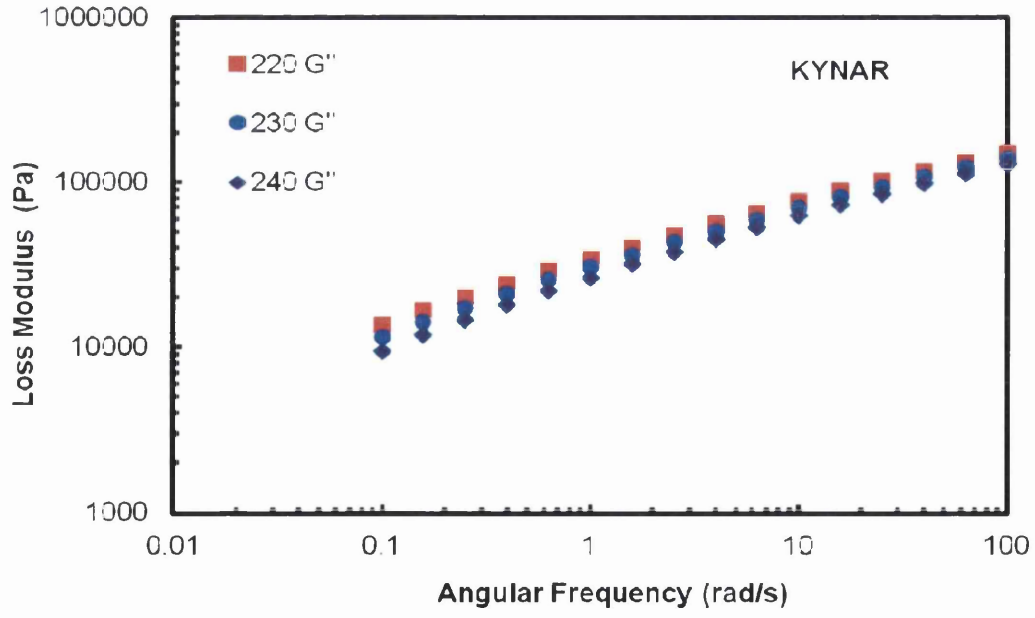

Figure 5.9b. Loss modulus vs. Angular frequency
Measuring results for Freq. Sweep
PVDF at three desired temperature (220- 240 °C)

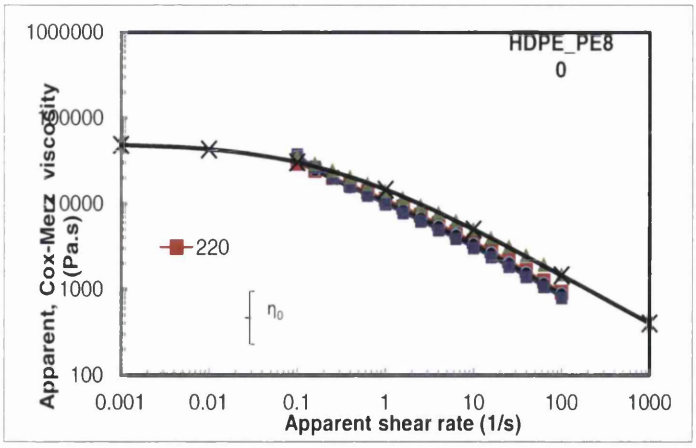

Figure 5.10. Fitting Model, HDPE at 220 °C

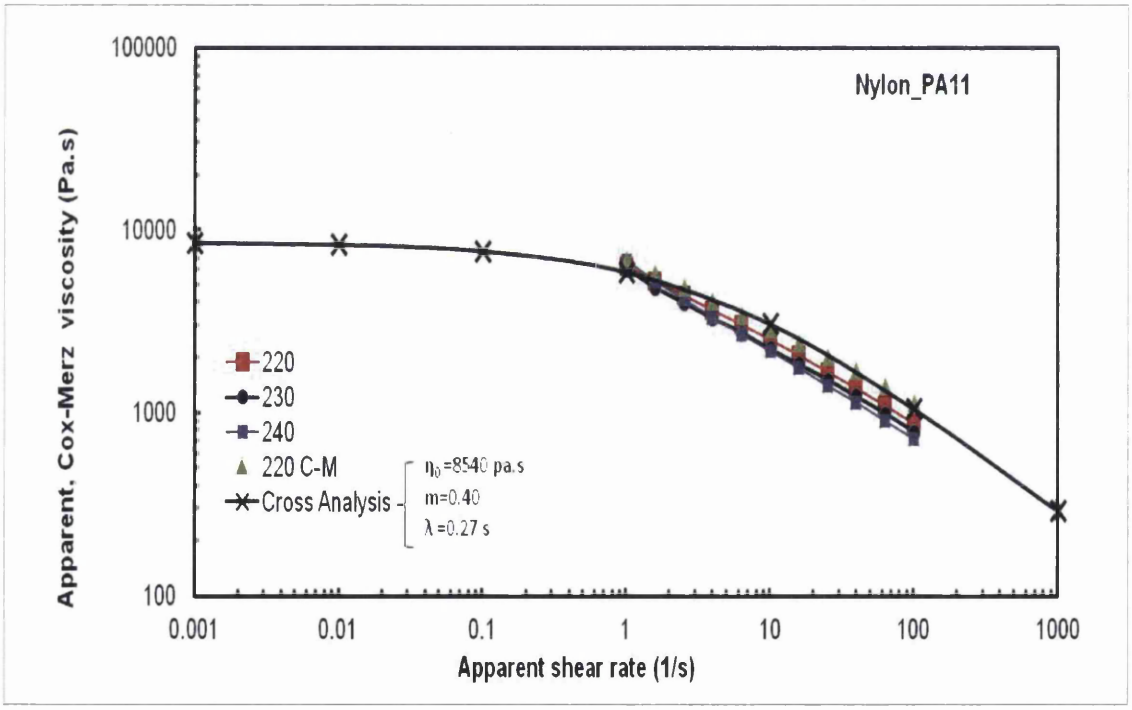

Figure 5.11. Fitting Model, PA11 at 220 °C

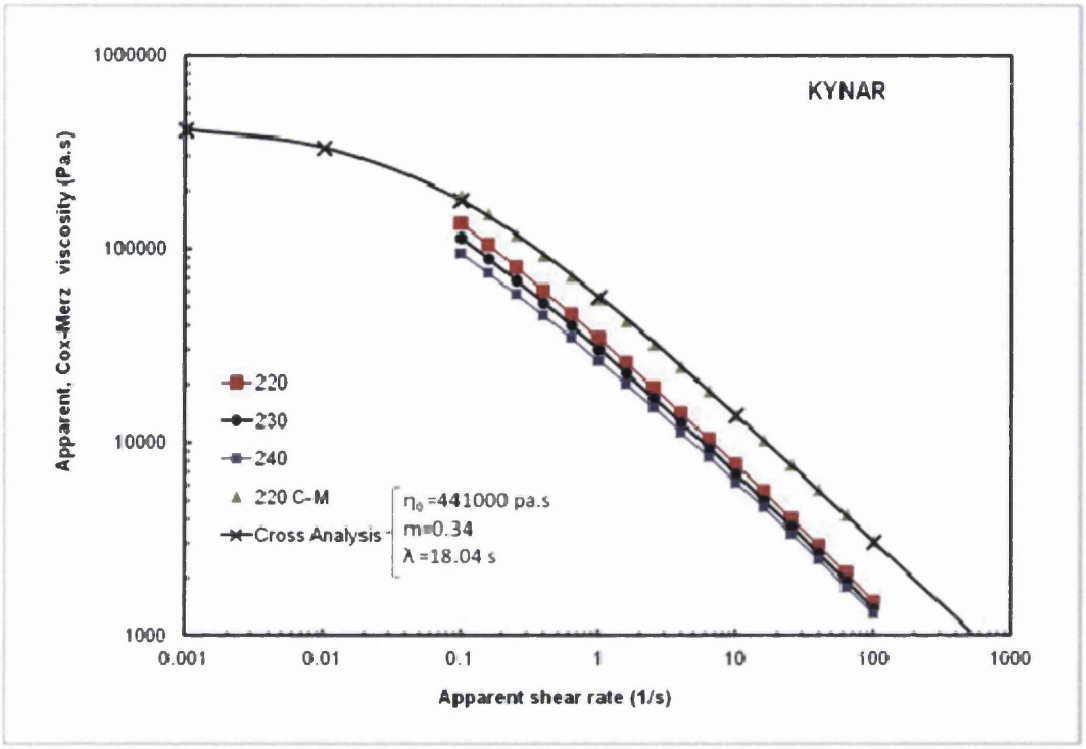

Figure 5.12. Fitting Model, PVDF at 220 °C

In any real material...rearrangement necessarily require a finite time ... [therefore] all real materials are viscoelastic.

Nicholas W. Tschoegl

Chapter 6

Rheological Characterization on Bio-fluid (Sputum); Exp. vs. Computational

The main focus of this computational modelling chapter is to determine the extensional rheological response of sputum biofluids to provide a diagnostic tool (biomarker) for experimentally-based pathological analyses and clinical practice. This may be accomplished through advanced rheological parameterisation and characterisation of sputum samples, when considering extensional deformation flow situations that mimic sputum escalator deformation in the lung-airways. Sputum samples have been collected from patients (male and female, over fifty years of age) suffering from Chronic Obstructive Pulmonary Disease (COPD) at two stages of

development: uninfected (stable or non-infective) state and infected (suffering exacerbations) state.

Samples have been tested without any pre-treatment such as mechanical homogenisation. Experimental and numerical studies of Capillary Break-up Extensional Rheometer (CaBER) have been performed, from which comparison significant correlations are presented. Typically, the dynamic development of the mid-filament diameter is monitored during the process of necking and filament-failure (break-up). The aim is to link this type of data with that emerging from experimental/clinical trials to provide a biomarker revealing insight on state of disorder and resultant treatment.

The rheology of sputum samples is represented through two rheological fluid modelling approaches: (i) a kinetic Single Extended pom-pom (SXPP) model; (ii) a time-dependent thixotropic Modified Bautista-Manero (MBM) model. These models are sufficiently rich to enable description of both network-structure and rheological properties, exhibiting viscoelastic response (memory), with strain-hardening/softening and shear-thinning properties.

6.1 Introduction

Biological materials have been the subjects of many rheological studies due to the relationship between their viscoelastic properties and their physiological function. Typically, the biorheology field covers the investigation of deformation and rheological properties of materials within biological systems. One such situation, in which the viscoelastic properties of a biomaterial is linked to a pathologic state, is via the enhanced elasticity and viscosity of sputum in patients with pulmonary disease conditions - such as, cystic fibrosis (CF), chronic obstructive pulmonary disorder (COPD), and asthma. The increased rigidity of respiratory mucus (sputum) has been proposed to be responsible for the exertion in lung clearance observed in CF patients. As such, some current treatments are directed towards decreasing the stiffness of infected sputum, and rebuilding its viscoelastic features, that are suitable for clearance. Hence, it is important to study the viscoelasticity of sputum, and its rheology in relation to physiological function, so that diagnosis and treatment of respiratory infection can be improved.

On COPD To provide some background, chronic obstructive pulmonary disorder (COPD) is the third main disease killer world-wide (fourth highest killer in UK). It is estimated that about three million people in the UK have COPD. Most patients with COPD remain undiagnosed until late in their disease history; yet, early detection can be influential. It is important to capture COPD-sufferers at an initial stage of infection to prevent possible irreversible lung-damage inflicted by intense COPD. Currently the initial diagnostic of COPD is defined according to breathing tests (such as spirometry), CT scan, electrocardiogram, chest X-ray and blood-tests. Nevertheless, these assessments are often inaccurate and involve professional analysis.

Rheometry Conventional rheometry, performed using rotational/oscillatory rheometers, reveals the shear properties of a material sample (in ideal shear flow deformation) (see chapter 2 section 2.5.1 for more details). However, most actual flows in nature (for instance those which are biologically relevant) and in technology are complex and can include both shear and extensional components. In fact, extensional flows can significantly stretch macromolecules, providing orders of magnitude increase in elastic forces and extensional viscosity. Hence, quantifying the extensional rheology properties of a material in a complex flow condition is crucial in order to fully characterize its rheological behaviour. The rheology of biological complex fluids is necessary for normal vital functions of many processes in the body. Examples of biological flows where extensional mechanism are likely to play a key role comprise blood circulation [6.1], mucus transport in the airways, tear-fluid flow in the eyes, and saliva-flow in the mouth [6.2, 6.3]. As a result, understanding the behaviour of healthy and unhealthy bio-fluids under extensional deformation could provide significant insight and medical benefits, in terms of discovering and developing novel treatments, therapies and more accurate/potential diagnostic outcomes.

Sputum – properties and measurement To understand the flow mechanism of mucus in the lungs by coughing, there have been many simulated experimental investigations (using a simulated cough machine) [6.4–6.9]. These researchers have brought several issues into focus, on the subject of the role played by rheological properties of mucus (as a viscoelastic biomaterial) [6.10–6.12]. Most of the

published data on the rheology of sputum focused in studies relating to the application of steady and oscillatory shear, considering sputum as a non-Newtonian viscoelastic material exhibiting shear-thinning and thixotropic properties [6.14].

However, for scientific reasons, many of the early rheological tests performed on sputa have been conducted under relatively large deformation and forces. The increased stiffness of infected sputum prevents its proper airway clearance. As such, therapeutic methods are often directed to reducing sputum-viscoelasticity to their normal (healthy) levels. Design of catalysts capable of altering the increased rigidity of CF sputum is a main target for treatment of this ailment, and rheological studies of these materials can shed light on the structures responsible for the shifted viscoelasticity within the diseased condition. Consequently, much of the rheological data on rheology has focused on the viscosity of the material after the primary disruption of its elastic component.

To investigate the possibility of damaging the network structures in the sputum during the shear viscosity measurements, Nielsen et al. [6.15] used a combination of oscillatory, creep-recovery and steady shear techniques. Their results suggest that measurements of elastic moduli reflects the mechanical properties of sputum in situ rather than viscosities, and those methods used to measure viscosities, may destroy part of the biopolymer structures responsible for the abnormal rheology of CF sputum. In contrast, measurements of shear elastic moduli at low strain rates appear to protect more of the original structure of the sputum and may establish superior techniques to evaluate the effects of potential mucolytic agents.

Filament stretching The filament stretching rheometer has emerged as an approved apparatus for measuring the extensional properties of moderately viscous (mobile) non-Newtonian fluids [6.16-6.22]. Under continuous stretching, the filament-stretching rheometer is operated in *FiSER*-mode; alternatively, under step-strain (*CaBER*) mode, operation is under capillary-break-up (short initial stretch) conditions[6.17, 6.18, 6.22] (see chapter 2 section 2.5.2 for specific details). In continuous stretching operation, a vertical cylindrical liquid bridge of the sample (vary in length and loading) formed between two circular end-plates is subjected to a prescribed extensional deformation. Subsequent necking leads to significant thinning and reduction of the middle-section of the filament, whilst the rigid end-plates result

in considerable shearing within the filament-foot region. In *CaBER* trials, a rapid axial step-strain of fixed magnitude is imposed on the sample, which is subsequently allowed to respond to that local conformational change, before proceeding towards break-up under the action of capillary forces (fluid self-selecting time-scale).

An extensive survey of filament stretching technology is provided by McKinley and Sridhar [6.16], covering the dynamical response of non-Newtonian fluids within filament-stretching rheometers. In the present study, it is anticipated that sputum samples demonstrate strain-hardening, requiring various representative constitutive equations to accommodate such response. An extensive experimental and numerical review on break-up for Newtonian fluid filaments and jets has been provided by Eggers [6.17]. Regarding the step-strain mode, Anna and McKinley [6.18] studied the dependency in the transient of the diameter-profile of the filament, and the time to break-up as a function of the sample molecular weight. This work included comparison against simple theory for breakup of slender viscoelastic filaments.

Typically, in either mode, the transient evolution of the mid-filament diameter profile is monitored during the process of necking and failure, from which the appropriate rheological calculations are performed. Ambitions are to link this type of data (as a rheological bio-marker), with that emerging from experimental/clinical trials to assist diagnosis and treatment-selection in the early stages of COPD advance.

Predictive CFD study The focused challenge of the present computational study relates to the advanced prediction of biofluid flows within the respiratory system. Here and under filament-stretching, the focus is principally on the analysis and influence of material parameters on the temporal-evolution of the cylindrical filament shape (R_{mid} profile). The sputum samples are collected from three COPD-suffering patients, without stimulation. These patients have donated sputum-samples that correspond to two distinct stages of disease development: uninfected (stable or non-infective) state and infected (suffering exacerbations) state. In the present context, sputum rheology may be modelled through a number of approaches, from kinetic-molecular theory (non- thixotropic pom-pom SXPP models [6.23-6.25]) and from thixotropic micellar network theory (worm-like micelles-MBM model [6.26-6.29]). Here, pom-pom parametric variation is conducted over structural network

description to explore a wide variety of topologies (entanglement, branching - molecular architecture), rheological properties (tension-hardening or softening, shear-thinning), relaxation mechanisms (backbone stretch, multiple time-scales). Under dynamic thixotropic micellar network models, parametric variation covers temporal network construction and destruction parameters.

To address the simulation and to solve the discretised system of partial differential equations involved, the basis of the present numerical strategies employed follows those implemented in our previous related studies [6.30–6.35]. This absorbs appropriate adjustments suitable to the specific problem characteristics of step–strain filament-stretching. The foundation of this semi-implicit time-stepping approach is that of a parent-subcell hybrid finite element/volume method, based on a Taylor series expansion of second-order in time, in combination with a fractional-staged incremental pressure-correction method. In addition, an Arbitrary Lagrangian Eulerian (ALE) formulation is introduced with particle tracking facilities to deal with domain and free-surface dynamic movement. Adopting this approach, spatial discretization is performed for the momentum-continuity equations through finite element procedures, whilst the finite volume method is employed for stress. Further discretisation detail is expanded upon below.

6.2 Governing Equations and Mathematical Modelling

This chapter focuses on the representation of steady incompressible viscoelastic flow problems under isothermal conditions. The associated non-dimensional continuity-momentum balance equations, whilst neglected gravitational body and inertial forces ($Re \rightarrow 0$), may now be given by:

$$\nabla \cdot u = 0 , \tag{6.1}$$

$$Re\frac{\partial u}{\partial t} + Reu \cdot \nabla u = -\nabla p + \nabla \cdot \boldsymbol{T} . \tag{6.2}$$

where the primary dependent variables of velocity, pressure and extra stress are represented by $u(V_r,V_z)$, p and $\boldsymbol{T}$, respectively, with each being a function of space (r, z) and time (t).

Here, the total stress $\boldsymbol{T}$ is split into elastic polymeric-stress ($\boldsymbol{\tau}$) and solvent-viscous stress ($2\mu_s\boldsymbol{d}$) contributions. Similarly, the total zero shear-rate viscosity (μ_0) is distinguished into solvent viscosity (μ_s) and polymeric viscosity (μ_p) contributions, so that $\mu_0 = \mu_s + \mu_p$, and hence the solvent-fraction factor β introduces, as $\beta = \mu_s / \mu_0$. The deformation rate tensor ($\boldsymbol{d}$) is expressed through the standard notation for spatial gradients and tensor transpose (velocity gradient $\boldsymbol{L} = \nabla u$) as $\boldsymbol{d} = (L + L^T)/2 = (\nabla u + \nabla u^T)/2$. Some relevant characteristic quantities are presented based on a characteristic velocity scale U (average velocity), the initial filament length (L_0) (m) as a length scale ($L=L_0$), and a viscosity scale ($\mu=\mu_0$, zero-shear rate viscosity). For the purpose of introducing dimensionless group numbers, a time-scale ($t_{scale} = L_0/U$) (s) is derived, the inverse of which defines a characteristic deformation rate and an initial stretch-rate ($\overset{g}{\varepsilon}_0 = U / L_0$) ($s^{-1}$). By considering the principal material relaxation time λ (s), constant fluid density ρ (kg/m^3) and the interfacial surface tension coefficient χ (N/m), the dimensionless group numbers of Reynolds, Deborah, Capillary and Bond can be specified, viz:

$$Re = \frac{\rho \overset{g}{\varepsilon}_0 L_0^2}{\mu_0}, \quad De = \lambda \overset{g}{\varepsilon}_0, \quad Ca = \frac{\mu_0 \overset{g}{\varepsilon}_0 L_0}{\chi}, \quad B_0 = \frac{\rho L_0^2}{\chi} g. \tag{6.3}$$

Then, the stress and pressure are non-dimensionalised with a scale of ($\mu_0 \overset{g}{\varepsilon}_0$).

Here, two strain hardening/shear thinning; the kinetic/molecular-based pom-pom and the time-dependent thixotropic MBM models are considered. A general statement of the differential constitutive model may be expressed in dimensionless form as:

$$\mathrm{f}(\boldsymbol{\tau})\boldsymbol{\tau} + De\overset{\nabla}{\boldsymbol{\tau}} + \frac{(1-\beta)}{De}\left[g(\boldsymbol{\tau})\right]\mathbf{I} + \frac{\alpha De}{(1-\beta)}\boldsymbol{\tau}\cdot\boldsymbol{\tau} = 2(1-\beta)\boldsymbol{d}, \tag{6.4}$$

where, $$\overset{\nabla}{\boldsymbol{\tau}} = \frac{\partial \boldsymbol{\tau}}{\partial t} + \mathbf{u}.\nabla\boldsymbol{\tau} - (\nabla\mathbf{u})^{\dagger}.\boldsymbol{\tau} - \boldsymbol{\tau}.(\nabla\mathbf{u}). \tag{6.5}$$

From this general formulation, and with appropriate parameter selection for governing equation (6.4), the functional f($\boldsymbol{\tau}$) and g($\boldsymbol{\tau}$) for the Single eXtended pom-

pom (SXPP) model in terms of the base parameters (q, ε_{pom}, λ_{pom}, α_{pom}) and (De, β) may be given by:

$$f(\boldsymbol{\tau})=\frac{2}{\varepsilon_{pom}}\left(1-\frac{1}{\lambda_{pom}}\right)\mathrm{e}^{\nu\left(\lambda_{pom}-1\right)}+\frac{1}{\lambda_{pom}^{2}}\left(1-\left\{\frac{De}{(1-\beta)}\right\}^{2}\frac{\alpha_{pom}}{3}\mathrm{tr}(\boldsymbol{\tau}\cdot\boldsymbol{\tau})\right); \quad (6.6)$$

and $g(\tau)=f(\tau)-1$.

Here, the free parameter v is estimated by data-fitting and found to be inversely proportional to the number of side-branch arms dangling from an end of the molecular chain-segment (v = c/q, with c taken as 2), see Blackwell et al. [6.16]. The parameter ε_{pom} is the ratio of the polymer-chain backbone stretch (λ_{0s}) to the orientation (λ_{0b}) relaxation times. With the single-equation (SXPP) approximation to the pom-pom model, representation of the back-bone stretch parameter λ_{pom}, is given as a function of trace $\boldsymbol{\tau}$ through expression:

$$\lambda_{pom}=\sqrt{1+\frac{1}{3}\frac{De}{(1-\beta)}\left|\mathrm{tr}(\boldsymbol{\tau})\right|} \quad ; \quad \varepsilon_{pom}=\frac{\lambda_{0s}}{\lambda_{0b}}, \qquad (6.7)$$

For this class of pom-pom model, the identifying parameter set (q, ε_{pom}, λ_{pom}, α_{pom}) are defined as: the number of side-branch arms to the backbone chain-segment (q), system entanglement (ε_{pom}), the stretch of the back-bone segment (λ_{pom}), and the degree of system anisotropy (α_{pom}) as well as solvent fraction (β). Here, in corresponding physical properties the implication behind the parameter settings is as follows: high-solvent ($\beta\rightarrow1$) to low-solvent ($\beta\rightarrow0$) fractions imply dilute to concentrated polymeric content; whilst highly-entangled ($\varepsilon\rightarrow0$) to mildly-entangled ($\varepsilon\rightarrow1$) network descriptions imply more cross-linking/less-mobile (polymer-melts) to less cross-linking/highly-mobile (polymer-solutions) system properties.

Considering the MBM model, its precise form is recovered from equation (6.4) when setting the Giesekus parameters $\alpha = 0$, $g(\tau)=0$ and then:

$$\mathrm{f}(\boldsymbol{\tau})=1+\omega\xi_{\eta_{p0}}\boldsymbol{\tau}_{p}:\mathbf{D}. \qquad (6.8)$$

In this micellar model, ω and $\xi_{\eta_{p0}}$ are structural construction and destruction parameters, respectively.

To summarise, the model parameters that control the material characteristic response of each fluid are then: $\{\omega, \xi_{\eta_{p0}}, \beta\}_{\text{MBM}}$ for the MBM model; and $\{ q, \varepsilon_{pom}, \lambda_{pom}, \alpha_{pom}, \beta\}_{\text{SXPP}}$ for the SXPP model. In this respect and current study, the viscometric data of relevance are reported in Figure 6.1, covering extensional viscosity response for the various system variation parameters cited above.

Viscometric functions The steady extensional viscosity material functions of the pom-pom (SXPP) and MBM models are displayed in Figure 6.1(a-b). The selected parameter values of (q, ε_{pom}, α) for SXPP and (ω, ξ) for MBM have been matched together at the peak extensional rheological response. According to Figure 6.1, the steady extensional viscosity of both models displays an initial rise to a peak with increasing extension-rate, then a decrease (sharp drop in the case of the MBM model). The plots demonstrate that, at the set parameter of (ε_{pom}=0.99, β=0.262), increasing the number of dangling arms (q) leads to a significant rise in the level of the extensional viscosity in the SXPP fluid. Whilst increasing the entanglement state of the fluid (ε_{pom}) at fixed parameters of (q=8, β=0.262), the rising trend in the level of the extensional viscosity is followed by a shifted-peak to the lower extensional rate observed.

As shown in Figure 6.1b, increasing the value of structure-construction parameter (ω), at a fixed structure-destruction value (ξ=0.028) and solvent-fraction (β=0.262), leads to significant growth in the peak-value of the extensional viscosity. Similar trend in peak extensional viscosity rise is also realised when the structure destruction (ξ) parameter is elevated, for structure-construction parameter (ω=4) and solvent-fraction (β=0.262).

At a specified parameters of (q=8, ε_{pom}=0.99) in SXPP and (ω=4, ξ=0.028) in MBM model, the peak extensional-viscosity value decreases for rising solvent fraction (from β=0.262 to β=0.915), and exhibits a lower second-plateau viscosity level at reduced levels of solvent-fraction (β=0.262).

Experimental procedure The experimental apparatus used in this study is principally that referred to in chapter 2, sections 2.5.2. Sputum samples have been collected from patients (male and female, over fifty years of age) suffering from COPD at two different stages of development: uninfected (stable or non-infective) state and infected (suffering exacerbations) state. All samples delivered by the Respiratory Medical School of Singleton Hospital, were provided with consent from the donor patients.

The basic configuration of the filament-stretching rheometer is that presented schematically in Fig. 2.9. Under present experimental protocols, test-samples were not subjected to any form of pre-treatment, such as mechanical homogenisation. The experimental procedure adopted was to load a small volume of sputum between the top and bottom rounded flat-plates, each of diameter 7 mm, and subject to a gap-width setting of 4mm. Then initially, the sample was extended rapidly by moving the top-endplate upwards, and away from the fixed bottom-endplate. This established the formation of a filament, of central uniform thickness, and proceeded to the point where the combined action of surface tension, inertia and rheological effects caused capillary break up (typically producing filament lengths of 1.5-2.5cm). The mid-plane radius of the filament, established between the two plates during and after stretching, was then monitored using a high speed camera (Photron Fastcam ultima APX). A series of such experimental runs were conducted on each sample due to the potential material limitations associated with the nature of the sputum, and problems encountered with reproducibility.

6.3 Problem Specification

Under the filament-stretching procedures of current interest, the filament is stretched between two flat circular end-plates through a controlled synchronous motion to a specific time/length, followed by a sudden halt in motion. This leads to both stress growth (FiSER) and relaxation (CaBER), followed by filament break-up. In the FiSER mode, the time-scale is inversely proportional to the initial constant stretch-rate imposed on the moving-plates. In contrast, for the CaBER mode, a self-selective (own) time-scale of material sample itself is chosen (see Figure 6.2).

Using a cylindrical coordinate system {r, θ, z}, the flow was constrained to be axisymmetric so that all flow fields are independent of the angular coordinate θ, and the simulation may be restricted to the rz-plane. The problem is axisymmetric about the axial z-axis, along the filament centreline and perpendicular to the end-plates. The origin is taken at the intersection between the filament mid-plane and this axis. The moving domain has an initial aspect-ratio ($\Lambda_0 = L_0 / R_{plate}$=0.54) and a final aspect-ratio ($\Lambda_f = L_f / R_{plate}$=$2L_f/D_{plate}$), where L_f and R_{plate} represent the final filament lengths and plate-radius, respectively.

The filament stretching problem involves a free-surface determination, where capillary forces act upon the liquid-gas free-surface to determine its displacement. The force balance on this interface may be expressed in dimensional terms, for a fluid with surface tension coefficient χ, as a function of the Cauchy stress ($\boldsymbol{\sigma}$), ambient surrounding pressure (p_a), principal radii of curvature (R_1 and R_2) [6.36] and normal vector ($\boldsymbol{n}$) to the free-surface,

$$\boldsymbol{\sigma}\cdot\boldsymbol{n} = -p_a\boldsymbol{n} - \chi\left(\frac{1}{R_1}+\frac{1}{R_2}\right)\boldsymbol{n}. \tag{6.9}$$

Based on the initial imposed stretch-rate ($\dot{\varepsilon}_0$), the appropriate corresponding boundary conditions are those of no-slip on the end-plates, under specific axial velocity component, $V_z = \dot{\varepsilon}_0 L(t)$, where $L(t) = \pm 0.5 L_0 \exp(\dot{\varepsilon}_0 t)$. Here, the notation of positive/negative L(t) are assigned to upper and lower halves of the filament.

Background theory that links evolution of filament mid-plane radius (R_{mid})(t) to rheometric functions, such as apparent extensional viscosity (μ_{app}), and principal relaxation time (λ), requires the satisfaction of certain base assumptions. Here, in pure uniaxial extensional deformation, one seeks the formation of a cylindrical filament shape, persistent in symmetry about the mid-plane, on which constant state of stress/deformation-rate applies at any particular time. Then, during the thinning-down stress-growth process under CaBER trials, evolution of the filament mid-plane radius, R_{mid}(t), can be measured and related to extensional viscosity. Hence, both such quantities are governed by a force balance on the filament, determined through

viscous, elastic and capillary forces. The extensional viscosity may be expressed dimensionally as [6.37],

$$\mu_{app} = \frac{-\chi}{2(dR_{mid} / dt)}, \tag{6.10}$$

where centre-plane extension-rate for a slender filament may be interpreted through the evolution of filament radius, R_{mid}(t), as [6.25].

$$\dot{\varepsilon}(t) = -\frac{2}{R_{mid}} \frac{dR_{mid}(t)}{dt} . \tag{6.11}$$

Here, the problem of data correlation is tackled directly, by avoiding extraction of temporal gradients on (R_{mid})(t), as this is a perennial error prone process (secondary data); instead, preferring to retain raw R_{mid}-data in both experimental measurement and numerical assessment. From this R_{mid}-data quality of match may be inferred therefore on extensional viscosity. From the simulations, and with knowledge of the N_1 and extension-rate on the centreline, one may cross-check this evidence. Then, in addition, dimensional time for thinning-down and stress-growth (λ_g), taken to be related to the principal relaxation time (λ), can be estimated from the counterpart relationship,

$$\frac{R_{mid}(t)}{R_0} = (\frac{GR_0}{2\chi})^{1/3} \exp(\frac{-t}{3\lambda_g}), \tag{6.12}$$

where G=$\frac{\eta_p}{\lambda}$ is the elastic modulus of the material. For more details, readers are referred to [6.37].

6.4 Results and Discussion

6.4.1 Experimental Data

Beyond the limitations inherent to specific rheological measurement techniques, current rheological characterization of sputum is largely hampered by the difficulty

of collecting sputum in sufficient quantities to facilitate single or reproducible measurements.

The experimental time evolution of the midpoint of the filament is given in Figure 6.3. What one is seeking here is to derive a correlation between R_{mid} data (for sputum, which relates to rheological properties) and the relative state of health of the donor-samples. Anomalies that may arise between data for patient-individuals, and also day-to-day for a single individual, may tie in to those noted in rheological properties (R_{mid}).

It is necessary to adopt appropriate criteria, in order to analyse these experimental data with their broad distribution, seeking consistency in trends on infected versus uninfected data across three patient-samples. In this manner, three different criteria have been proposed and Figure 6.4 plots comparison of the results against each criteria. Under the first criteria, only the median is considered, between highest and lowest value, in both infected and uninfected results, for all three patient-cases. From Figure 6.4a and in all three test cases, it can be seen that R_{mid} evolution for infected states were longer in time compare to their uninfected counterparts. On the other hand, there is *no consistency in* R_{mid} *starting-value*, between the behaviour of the uninfected state when compared to the infected state, taken across each patient-case. To address this issue, a second criteria is proposed: choosing the longest-time to break-up for infected sputum, and for uninfected sputum - the average of {higher, lower starting value} around the infected state (see Figure. 6.4b). Here, the figure for all cases displays the characteristic feature of an increased filament life-time for infected sputum, suggesting larger extensional viscosity when compared to uninfected sputum. Hence, a third and more appropriate criteria (see Figure 6.4c), has been developed: seeking the longest-time to break-up, as well as the larger extensional viscosities (η_e) amongst the infected data. Here, in the comparison and for the uninfected state, the closest R_{mid} starting-value to the infected state is adopted (equivalencing their initial Hencky-strain at the start of CaBER-mode). In addition, larger extensional viscosity (η_e), is defined relatively in terms of greater R_{mid}–values for infected states compared to uninfected states.

6.4.2 *Computational Predictions*

***Extensional response across models: pom-pom and MBM*:** One aspect of this work has been to compare and contrast the behaviour in complex flows of both pom-pom (kinetic-based) and MBM (thixotropic) models in their predictive capacity to represent that of the test bio-fluid sputum. In this respect, we configure matching peak extensional rheological response for the pom-pom model against that for the MBM model. This allows us to independently match over extensional viscosity (η_e) covering three scenarios of strain-hardening for pom-pom and MBM models. The relevant selected parameter values of (q, ε_{pom}, α) for pom-pom and (ω, ξ) for MBM, along with terminating Hencky-strain (FiSER) and the step-strain duration times (time-to-break up for CaBER), are tabulated in Table 6.1 for each model. We have observed that commencing from various alternative *starting positions* (in R_{mid}, end of FiSER, start of step-strain) can significantly influence subsequent flow response. To demonstrate this aspect, hence the practical implications of variation in final (FiSER) filament aspect-ratios, we have investigated three choices of filament length: diameter ratio, L/D= {1.6, 1.8 and 2} (see Figure 6.5), each relevant to the FiSER-phase.

Findings are reported comparatively across the two models and three samples, in terms of R_{mid}-profiles (see Figures. 6.6, 6.7 and 6.8) and their corresponding first normal stress difference (N_1) fields (see Figures 6.9, 6.10 and 6.11). In terms of mid-filament time-evolution, this analysis reveals that numerical predictions starting at Hencky-strain 2 best match (in pattern) to the experimental results. For all three levels of strain-hardening trialled and at the higher aspect-ratio, equivalent to a starting Hencky-strain of 2, it is observed that the pom-pom fluid filament takes longer-time to reach its break-up phase compared to that for MBM. For lowest aspect-ratio (ε_{Hencky} =1.6) there is no differences between pom-pom and MBM predictions.

6.4.3 R_{mid}-*Profiles:*

Variation in aspect-ratio (Λ_f=L_f/R_{plate})

A primary objective in selecting an appropriate final filament aspect-ratio (L/D variation), is to establish a substantial and sustainable necking-down filament column

at its core (undisturbed cylindrical structure). Under FiSER protocol, trends in R_{mid} development as a function of Hencky-strain (Figure 6.5), confirm that both model-predictions follow similar patterns over the early stages of stretching. As the level of stretch (aspect-ratio) increases, slight departure between model-predictions in R_{mid} becomes apparent. At the elevated Hencky-strain level of ε=2, this departure between pom-pom and MBM predictions for the highly-polymeric (β=0.262) choice is indeed quite significant.

Aspect-ratios (ε_{Hencky})=1.6 & 1.8: Figure 6.6(a-c) demonstrate for both models and for three patient-samples, the variation of R_{mid} as a function of time, starting at Hencky-strain 1.6. Inspection of Figure 6 indicates only slight variation in R_{mid}-profiles between model-predictions, in which R_{mid} for the highly-polymeric fluid (β=0.262) lies slightly above those with lower-polymeric contribution. The predictions of R_{mid} in highly-polymeric (β=0.262) instances, for both pom-pom and MBM models, show imperceptible oscillation at earlier times, up to around t=1 unit.

Figure 6.7(a-c) displays the position for the same fluids at a larger aspect-ratio (L/D=1.8). Comparing results for the MBM model with solvent-fraction β=0.262 at two alternative aspect-ratios {1.6, 1.8}, see Figures. 6.6 and 6.7, identifies a significant change in rate-of-decrease in R_{mid}-profile. In this instance, increase in Hencky-strain level from 1.6 to 1.8 yields steeper decrease in the R_{mid}-profile.

Aspect-ratio (ε_{Hencky})=2: As above, Figure 6.8(a-c) shows data starting at Hencky-strains 2, with comparison between experimental observations for three sputum patient-samples and numerical predictions for both models. Here, the variation of R_{mid} (scaled by R_0, initial radius at onset of step-strain) provides close agreement with equivalent experimental sputum-data, commending Hencky-strain 2 as the superior choice. With the pom-pom model, the time to break-up for the filament is observed to increase upon rise in the level of strain-hardening. In contrast, under the MBM model, R_{mid}-profiles demonstrate a decreasing trend in time-to-break up at higher-rates with increased level of hardening. The pom-pom fluid filament thins at the slowest rate, compared to the other model alternatives, and takes a longer time to reach its break-up phase.

Comparison of pom-pom (q=4, ε_{pom}=0.99, α=0) and MBM (ω=4, ξ=0.242); β=0.915; Both model-predictions follow similar trends in R_{mid}(t) up to the level of t=5 units (t≈50 sec). Beyond this time-stage, the declining evolution of pom-pom R_{mid}(t)-profile begins to depart, at a slightly lower rate in comparison to that for MBM model-predictions. Having relatively higher rate of filament-thinning under MBM model-prediction, causes the slightly shorter time to break-up at t=2.8 time units, when compared to t=3.2 time units for the pom-pom fluid. This result is consistent with the viscometric data, as one might expect greater stability to be retained by the pom-pom variant.

Comparison of pom-pom (q=8, ε_{pom}=0.99, α=0) and MBM (ω=4, ξ=0.082); β=0.915; Once again, both pom-pom and MBM filaments neck-down in similar fashion up to t=5 time units (at t≈50 sec). Subsequently, the necking-down process under MBM model-prediction is more rapid, and the filament breaks-up at t=2.2 time units; whilst under pom-pom prediction, the filament has a smoothly declining trend to break-up at t=3.6 time units.

Comparison of pom-pom (q=4, ε_{pom}=0.99, α=0) and MBM (ω=4, ξ=0.028); β=0.262; Over the relatively short and early process period $2 \le t \le 4$, the MBM filament profile displays more rapid thinning and necking-down at filament-core. No temporal oscillations/fluctuations are detected under MBM prediction, and the process terminates earlier (t_f=0.6 units, Figure 6.8) than for the corresponding pom-pom model with t_f=4 units. This is due to the rapid and excessive necking when stress levels rise sharply; see Figure 11-N_1 profiles. The reason for such differences in flow response may well originate in the respective viscometric properties of these fluid models at the relevant levels of strain-hardening sustained.

pom-pom data comparison: *β=0.262 (solid red); β=0.915 (solid blue) (q=4, ε_{pom}=0.99, α=0)*; Here, we discuss the consequences of switching between the polymeric viscosity ratios, from high (β= 0.262) to low (β=0.915). In particular, for pom-pom model (q=4, ε_{pom}=0.99, α=0), on the resulting filament deformation profile (Figure 6.8), and at a selected aspect-ratio of L/D=2. The variation in R_{mid}(t) for pom-pom with β=0.262 departs from that of β=0.915 around t=1 unit (at t≈5 sec); subsequently, the high-polymeric fluid filament thins at a lower rate compared to the

low-polymeric case. There is a slight hint here of local minima and maxima formation over 0≤t≤1.5 units (0≤t≤15sec) in the highly-polymeric scenario (β=0.262) profile. After t=1.5 units, this profile enters long-time behaviour up to t=4 units. In the low-polymeric scenario (β=0.915), lesser extension, experienced at filament mid-plane, causes greater thinning in filament mid-plane radius. Under such β-change, and due to variation in strain-hardening, the time-to-break-up reduces from O(4 units) for the high-polymeric (β=0.262) fluid, to O(3.2 units) for the low-polymeric fluid (β=0.915).

MBM data comparison: *ξ=0.242 (dashed blue); ξ=0.082 (dashed green) (ω=4, β=0.915)*: Solutions are presented for the MBM model with a fixed solvent-fraction of β=0.915 and at a selected aspect-ratio *L/D*=2. The structure-construction parameter used is ω=4.0; with two different structure-destruction parameters of ξ=0.242 and ξ=0.082. Note that, as the ξ (structural destruction parameter) decreases, the micellar model system will exhibit greater level of strain-hardening. Temporal trends in response are shown in the trace of R_{mid}-profiles of Figure 6.8, where the fluid is observed to break-up earlier at ~2.2 time units (at t≈23 sec) for ξ=0.082 (higher level of strain-hardening), compared to 2.8 units (at t≈29.5 sec) for ξ=0.242 (lower level of strain-hardening). The higher resistance of the fluid to break-up is observed to arise in the filament with larger network-destruction parameter (ξ=0.242). This outcome would appear to oppose that observed under pom-pom predictions.

Numerical results vs. experimental data: In Figure 6.8(a-c), the experimental results were selected from the third criteria listed earlier, as this gave rise to improved correlation between experiments and numerical predictions. Both model-predictions under pom-pom and MBM with β=0.262 reflect the properties of sputum more closely. It is apparent that, in general, pom-pom R_{mid}-predictions (with q=4, ε_{pom}=0.99, α=0 and β=0.262) follow similar patterns to those recorded for infected sputum test-cases 1 and 3, but are less good for test-case 2. For uninfected sputum test-cases, measured R_{mid}-profiles show reasonably good agreement with R_{mid}–predictions for MBM (ω=4, ξ=0.028 and β=0.262) in cases 2 and 3. Nonetheless, considering the practical shortcomings that lead to uncertainties associated with the experimental data, the agreement between $R_{mid(measured)}$ and $R_{mid(predicted)}$ is held to be a fairly close match, and hence, encouraging.

The results on uninfected-sputum data for candidate-one reflect similar behaviour to the infected-state up to t=5 time units; and then, the R_{mid}-curve declines sharply for a short time, terminating at t≈6 time units. For the infected-state, the R_{mid}-profile is barely changing over the time of the experiment (Figure 6.8a). In the case of patient-two and the uninfected-state, the R_{mid}-curve declines abruptly at the outset of the test; and hence, any error induced may have further affected subsequent precision in readings. In this case, the filament-thinning behaviour for infected-sputum mimics that under MBM (ω=4, ξ=0.082; β=0.915), with break-up at shorter times (Figure 6.8b), when compared to their numerical counterparts.

6.4.4 First Normal Stress Difference (N_1) Fields:

High polymeric viscosity fluids β=0.262, pom-pom, MBM, various L/D: Filament-shape and first-normal stress difference (N_1) fields are presented in Figures 6.9-6.11, at different times using different time-scales. These are derived with pom-pom (q=4, ε_{pom}=0.99, α_{pom}=0) and MBM (ω=4, ξ=0.028) versions. To compare with experimental results and timings, the time unit of **T** is chosen as a scaling time (defined relative to the experimental CaBER-time) to calibrate against the numerical results, and $\mathbf{t_f}$ is then the CaBER process-time. For this highly-polymeric fluid (β=0.262), qualitative observation from the figures reveals significant variation in the manner of filament-thinning, when comparing predictions from pom-pom (kinematic-based) and MBM (thixotropic) models.

Aspect-ratio (ε_{Hencky})=1.6 & 1.8: A comparison across models at a starting Hencky-strain of 1.6 units is depicted in Figure 6.9(a-d). For the MBM filament, a pinching structure forms at the centre of the filament at t=0.6T. As time advances, the symmetrical filament-shape pattern is maintained with no fluctuations and the filament thins down gradually until numerical failure occurs. This feature is also present in a much reduced form with the pom-pom filament. For both models, the maxima in first normal stress (N_1) are located at the filament-core and as time progresses, the region of these maxima moves towards the filament mid-plane at the free-surface.

At median aspect-ratio, equivalent to a starting Hencky-strain 1.8, comparison is made across model-predictions as displayed in Figure 6.10(a-c). The pom-pom fluid

displays the thicker filament core at all times, and consequently, a longer step-strain period. Here, the MBM fluid provides the more bulbous feet, thinner core and shorter time to break-up. Under pom-pom results, N_1-maxima decrease from 11.69 to 0.89 units (over 0.2≤t≤3 time unit) increasing thereafter slightly to 0.96 units at termination-time (t=4 time unit) (see Figure 6.10a and 6.10c). The converse is the case under MBM prediction, with shorter time to break-up displaying a monotonic increase in N_1-maxima from 15.05 to 21.17 units (over 0.2≤t≤0.6 time unit) (see first normal-stress fields of Figure 6.10b, also R_{mid}-profiles of Figure 6.7). With stronger necking forces acting on the filament, the sooner the filament will thin down.

Aspect-ratio ***(ε_{Hencky})=2***: By L/D=2, the same behaviour occurs as with L/D=1.8 in terms of time-to-break-up, in both instances of pom-pom and MBM predictions (see Figure 6.11(a-c)). It is clearly apparent that the pom-pom fluid takes a longer time to reach its break-up point. For the pom-pom filament, centre and foot pinching structures are formed beyond the early fluctuation period (0.6≤t≤1 unit), and the filament thins down at a slower rate compared to that with MBM, until numerical failure is encountered. Attached to the filament-feet, a bulge structure in the upper and the lower portions of the filament length appears at t=0.6 unit and beyond. The associated axial travelling wave is more apparent here up to t=1 unit, gradually diminishing and drawing out into the filament-feet as the step-strain period advances. In this case, the central section of the filament is thicker, leading to longer life-period of the thinning filament.

With the MBM fluid, the filament necks-down most rapidly (t=0.4 unit) to a fine thread in the central region (see first normal stress fields of Figure 6.11b, also R_{mid}-profiles of Figure 6.8) before break-up occurs, leaving two characteristic wine-glass upper and lower filament sections attached to the end-plates. In this case, since the level of Hencky-strain is close to a critical state, the filament breaks up rapidly at t_f=0.6 units. Note that, the maxima in first-normal stress (N_1) plots for both models are located around the centre of the filament. In the case of pom-pom, N_1-maxima decrease from 13.20 to 4.23 units (over 0.2≤t≤3 time units); increasing thereafter rapidly to reach 23.63 units during the latter time (3≤t≤4 time units); prior to ultimate termination (just before filament break-up). Quantitative data in Figure 11 indicate that N_1-maxima increase monotonically from 18.17 to 20.05 units (over 0.2≤t≤0.6

time units) with MBM, as opposed to under pom-pom. These N_1-maxima lie consistently higher than those at equivalent CaBER process-time, when compare to the pom-pom fluid. Note that N_1-maxima at time-period of t=0.6 units for MBM closely approximate those at t=4 time units for pom-pom. Such disparity in stress development between the two contexts permits the longer period of stretching under the pom-pom representation. The reason for such differences in flow response may be principally attributed to the contrast in strain-hardening properties endured, as discussed above.

6.5 Overview remarks

In this chapter, experimental and computational approaches of Capillary Break-up Extensional Rheometer (CaBER) have been considered to predict extensional rheological response, and correlate this to the degree of infection in patients suffering from Chronic Obstructive Pulmonary Disease (COPD). In this manner, a measure of extensional rheology through R_{mid}-evolution of sputum (experimental), from three doner-patients with COPD at two stages (stable and exacerbation - without stimulation), has been compared against that derived from numerical prediction. Rheological models employed for this purpose are the pom-pom (kinetic-molecular theory) (SXPP) and the MBM (time-dependent thixotropic) models. Typically, the dynamic progress of the midpoint of the filament is monitored during the process of necking and failure, with the aim of linking this temporal data with that emerging from counterpart experimental trials.

The broad distribution of experimental results across three patient-samples suggests the necessity of adopting specific criteria, to derive consistent correlations between infected versus uninfected data. In this manner, three different criteria has been investigated through this study and the most appropriate criteria has been found to be the one with the longest-time to break-up, as well as the larger extensional viscosities (η_e) amongst the infected data. For the uninfected data, the closest R_{mid} starting-value to the infected state is chosen (equivalencing their step-strain Hencky-strain). The sensitivity of the simulation to the choice of aspect ratio (L/D=1.6, 1.8 and 2) has also been investigated to predict suitable windows for experimental

operation sets. The outcome suggests that the results commencing from Hencky-strain 2 is the superior choice to adopt.

Overall, in this preliminary study, the capability has been demonstrated of these rheological models (pom-pom and MBM) to qualitatively predict rheological measures that can gainfully be used to assess the disparity between infected and uninfected sputum samples. This points the way towards a biomarker for COPD (process and device accordingly), in detecting the severity of COPD-infection with appropriate criteria and parameter sets. In general, pom-pom R_{mid}-predictions (with $q=4$, $\varepsilon_{pom}=0.99$, $\alpha=0$ and $\beta=0.262$) follow similar patterns to those recorded for infected sputum. While, measured R_{mid}-profiles for uninfected sputum test-cases appear to be in good agreement with R_{mid}–predictions for thixotropic MBM ($\omega=4$, $\xi=0.028$ and $\beta=0.262$).

References

[6.1] C. Lacombe, H. Essabbah, *Comparative haemorheology of pathological blood*, Scand. J. Clin. Lab. Investig. **41** (1981) 249–250.

[6.2] J.R. Stokes, G.A. Davies, *Viscoelasticity of human whole saliva collected after acid and mechanical stimulation*, Biorheology. **44** (2007) 141–160.

[6.3] E. Zussman, A.L. Yarin, R.M. Nagler, *Age- and flow-dependency of salivary viscoelasticity*, J. Dent. Res. **86** (2007) 281–285.

[6.4] M. Agarwal, M. King, J.B. Shukla, *Mucous gel transport in a simulated cough machine: Effects of longitudinal grooves representing spacing between arrays of cilia*, Biorheology. **51** (1994) 11–19.

[6.5] M. King, J.M. Zahm, D. Pierrot, S. Vaquez-Girod, E. Puchelle, *The role of mucus gel viscosity, spinability and adhesive properties in clearance by simulated cough*, Biorheology. **26** (1989) 737–745.

[6.6] M. King, G. Brock, C. Lundell, *Clearance of mucus by simulated cough*, J. Appl. Physiol. **58** (1985) 1776–1782.

[6.7] M. King, *The role of mucus viscoelasticity in cough clearance*, Biorheology. **24** (1987) 589-597.

[6.8] P.W. Scherer, L. Burtz, *Fluid mechanical experiments relevant to coughing*, J. Biomech. **11** (1978) 183–187. doi:10.1016/0021-9290(78)90011-8

[6.9] P.W. Scherer, *Mucus transport by cough*, Chest. **80** (1981) 830–833.

[6.10] S.S. Davis, J.E. Dippy, *The rheological properties of sputum*, Biorheology. **6** (1969) 11–21.

[6.11] B. Yeates, *Mucus Rheology*, in: R. G. Crystal and J. B. West (Ed.), Lung Sci. Found., Raven Press, New York, 1991: pp. 197–203.

[6.12] H.T. Low, Y.T. Chew, C.W. Zhou, *Pulmonary airway reopening: effects of non-Newtonian fluid viscosity*, J. Biomech. Eng. **119** (1997) 298–308.

[6.13] R. Denton, *Rheology of human lung mucus*, Ann. N.Y. Acad. Sci. **106** (1963) 746–754.

[6.14] S.K. Lai, Y. Y. Wang, D. Wirtz, J. Hanes, *Micro-and macrorheology of mucus*, Adv. Drug Deliv. Rev. **61** (2009) 86–100. doi:10.1016/j.addr.2008.09.012

[6.15] H. Nielsen, S. Hvidt, C.A. Sheils, P.A. Janmey, *Elastic contributions dominate the viscoelastic properties of sputum from cystic fibrosis patients.*, Biophys. Chem. **112** (2004) 193–200. doi:10.1016/j.bpc.2004.07.019

[6.16] G.H. Mckinley, T. Sridhar, *Filament-stretching rheometry of complex fluids*, Annu. Rev. Fluid Mech. **34** (2002) 375–415.

[6.17] J. Eggers, *Nonlinear dynamics and breakup of free-surface flows*, Rev. Mod. Phys. **69** (1997) 865.

[6.18] S.L. Anna, G.H. McKinley, *Elasto-capillary thinning and breakup of model elastic liquids*, J. Rheol. **45** (2001) 115–138.

[6.19] M. Yao, G.H. McKinley, B. Debbaut, *Extensional deformation, stress relaxation and necking failure of viscoelastic filaments*, J. Non-Newtonian Fluid Mech. **79** (1998) 469-501. doi:10.1016/S0377-0257(98)00116-5

[6.20] M. Yao, G.H. McKinley, *Numerical simulation of extensional deformations of viscoelastic liquid bridges in filament stretching devices*, J. Non-Newtonian Fluid Mech. **74** (1998) 47–88. doi:10.1016/S0377-0257(97)00052-9

[6.21] M. Yao, S.H. Spiegelberg, G.H. McKinley, *Dynamics of weakly strain-hardening fluids in filament stretching devices*, J. Non-Newtonian Fluid Mech. **89** (2000) 1-43. doi:10.1016/S0377-0257(99)00028-2

[6.22] A. Bhardwaj, E. Miller, J.P. Rothstein, *Filament stretching and capillary breakup extensional rheometry measurements of viscoelastic wormlike micelle solutions*, J. Rheol. **51** (2007) 693. doi:10.1122/1.2718974

[6.23] R.J. Blackwell, T.C.B. McLeish, O.G. Harlen, *Molecular drag-strain coupling in branched polymer melts*, J. Rheol. **44** (2000) 121–136.

[6.24] J.P. Aguayo, P.M. Phillips, T.N. Phillips, H.R. Tamaddon-Jahromi, B.A. Snigerev, M.F. Webster, *The numerical prediction of planar viscoelastic contraction flows using the pom–pom model and higher-order finite volume schemes*, J. Comput. Phys. **220** (2007) 586–611. doi:10.1016/j.jcp.2006.05.039

[6.25] M. Aboubacar, J.P. Aguayo, P.M. Phillips, T.N. Phillips, H.R. Tamaddon-Jahromi, B.A. Snigerev, M.F. Webster, *Modelling pom-pom type models with high-order finite volume schemes*, J. Non-Newtonian Fluid Mech.**126** (2005) 207–220. doi: 10.1016/j.jnnfm.2004.09.012

[6.26] F. Bautista, J.M. De Santos, J.E. Puig, O. Manero, *Understanding thixotropic and antithixotropic behavior of viscoelastic micellar solutions and liquid crystalline dispersions. I. The model*, J. Non-Newtonian Fluid Mech. **80** (1999) 93–113. doi: 10.1016/S0377-0257(98)00081-0

[6.27] O. Manero, F. Bautista, J.F.A. Soltero, J.E. Puig, *Dynamics of worm-like micelles: the Cox–Merz rule*, J. Non-Newtonian Fluid Mech. **106** (2002) 1–15. doi:10.1016/S0377-0257(02)00082-4

[6.28] E.S. Boek, J.T. Padding, V.J. Anderson, P.M.J. Tardy, J.P. Crawshaw, J.R.A. Pearson, *Constitutive equations for extensional flow of wormlike micelles:*

stability analysis of the Bautista–Manero model, J. Non-Newtonian Fluid Mech. **126** (2005) 39–46. doi:10.1016/j.jnnfm.2005.01.001

[6.29] F. Bautista, J.F.A. Soltero, J.H. Pérez-López, J.E. Puig, O. Manero, *On the shear banding flow of elongated micellar solutions*, J. Non-Newtonian Fluid Mech. **94** (2000) 57–66. doi:10.1016/S0377-0257(00)00128-2

[6.30] F. Belblidia, I.J. Keshtiban, M.F. Webster, *Stabilised computations for viscoelastic flows under compressible implementations,* J. Non-Newtonian Fluid Mech. **134** (2006) 56–76. doi:10.1016/j.jnnfm.2005.12.003

[6.31] F. Belblidia, H. Matallah, B. Puangkird, M.F. Webster, *Alternative subcell discretisations for viscoelastic flow: Stress interpolation*, J. Non-Newtonian Fluid Mech. **146** (2007) 59–78. doi:10.1016/j.jnnfm.2006.12.009

[6.32] M.F. Webster, H.R. Tamaddon-Jahromi, M. Aboubacar, *Time-dependent algorithm for viscoelastic flow-finite element/volume schemes*, Numer. Meth. Part. Diff. Eqns. **21** (2005) 272–296.

[6.33] P. Wapperom, M.F. Webster, *Simulation for viscoelastic flow by a finite volume/element method,* Comp. Meth. Appl. Mech. Eng. **180** (1999) 281-304. doi: 10.1016/S0045-7825(99)00170-X

[6.34] K.S. Sujatha, H. Matallah, M.J. Banaai, M.F. Webster, *Modeling step-strain filament-stretching (CaBER-type) using ALE techniques*, J. Non-Newtonian Fluid Mech. **148** (2008) 109–121. doi:10.1016/j.jnnfm.2007.05.014

[6.35] M.F. Webster, H. Matallah, K.S. Sujatha, M.J. Banaai, *Numerical modelling of step–strain for stretched filaments*, J. Non-Newtonian Fluid Mech. **151** (2008) 38–58. doi:10.1016/j.jnnfm.2008.02.002

[6.36] R. Keunings, *An algorithm for the simulation of transient viscoelastic flows with free surfaces*, J. Comput. Phys. **62** (1986) 199-220.

[6.37] G.H. Mckinley, *Visco-Elasto-Capillary thinning and break-up of complex fluids*, Rheol. Rev. (2005) 1–48. doi:10.1007/s00247-009-1482-4.

Scenarios		FiSER		CaBER ;ε_{Hencky}=2	
Model	Parameters	β=0.262 (Highly-Polymeric)	β=0.915 (Solvent-dominated)	β=0.262 (Highly-Polymeric)	β=0.915 (Solvent-dominated)
		Hencky Strain	Hencky Strain	Time-to-breakup	Time-to-breakup
pom-pom	q=4; ε_{pom}=0.99; α=0	3.6	5.0	4	3.2
	q=8; ε_{pom}=0.99; α=0	5.0	5.0	4	3.6
MBM	ω=4.0;ξ=0.028	2.2	-	0.6 (0.8 pom-pom)	-
	ω=4.0; ξ=0.242	-	5	-	2.8(4.0 pom-pom)
	ω=4.0;ξ=0.082	-	3.8	-	2.2(4.0 pom-pom)

Table 6.1. FiSER and CaBER (L/D)=2 senarios; pom-pom & MBM

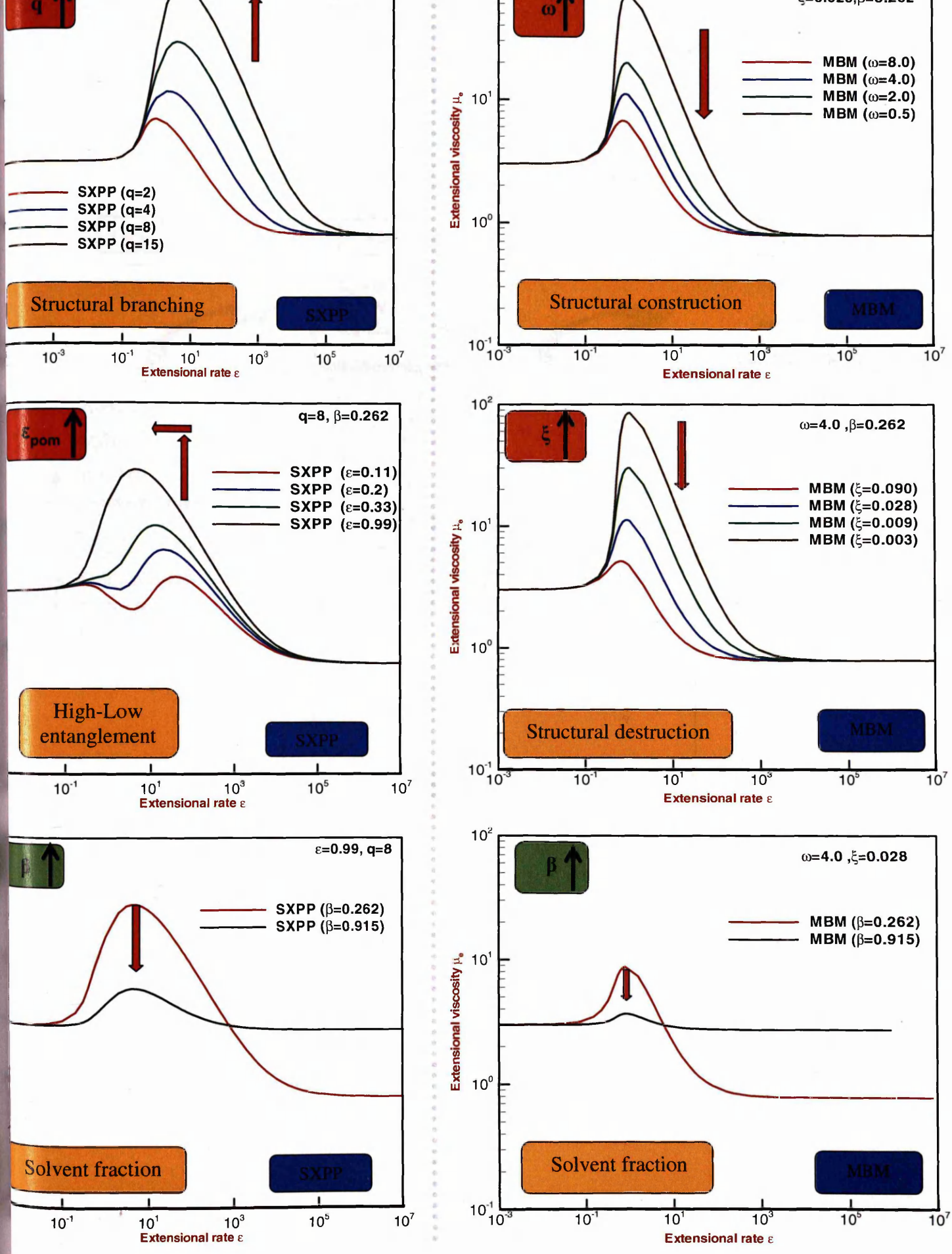

Figure 6.1. Extensional viscosity; a) pom-pom (SXPP) and b) MBM; variation of parameters

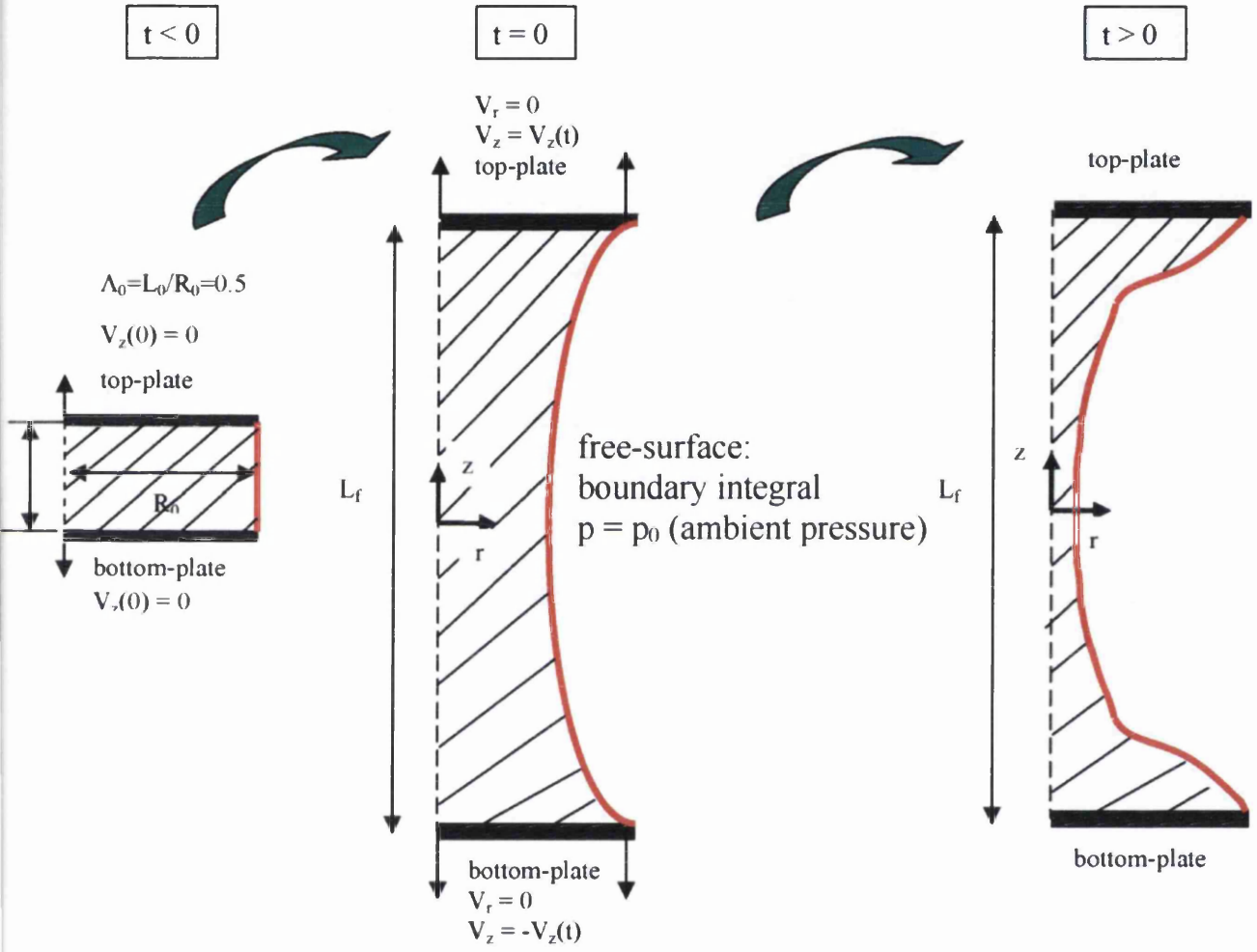

Figure 6.2. Step-strain schematic diagram

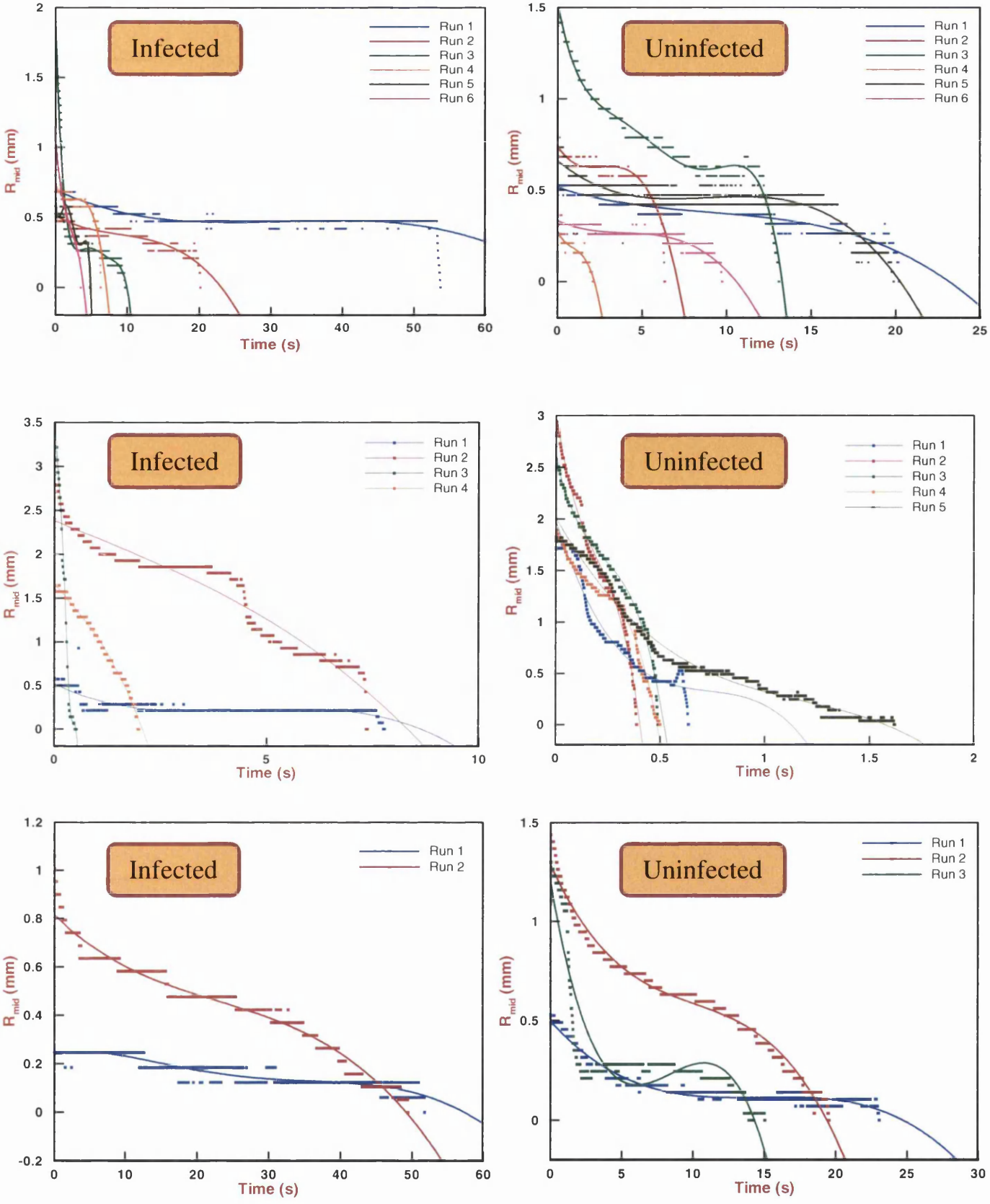

Figure 6.3. R_{mid} versus time; experimental CaBER raw data, infected and uninfected states; a) sample 1 b) sample 2, c) sample 3

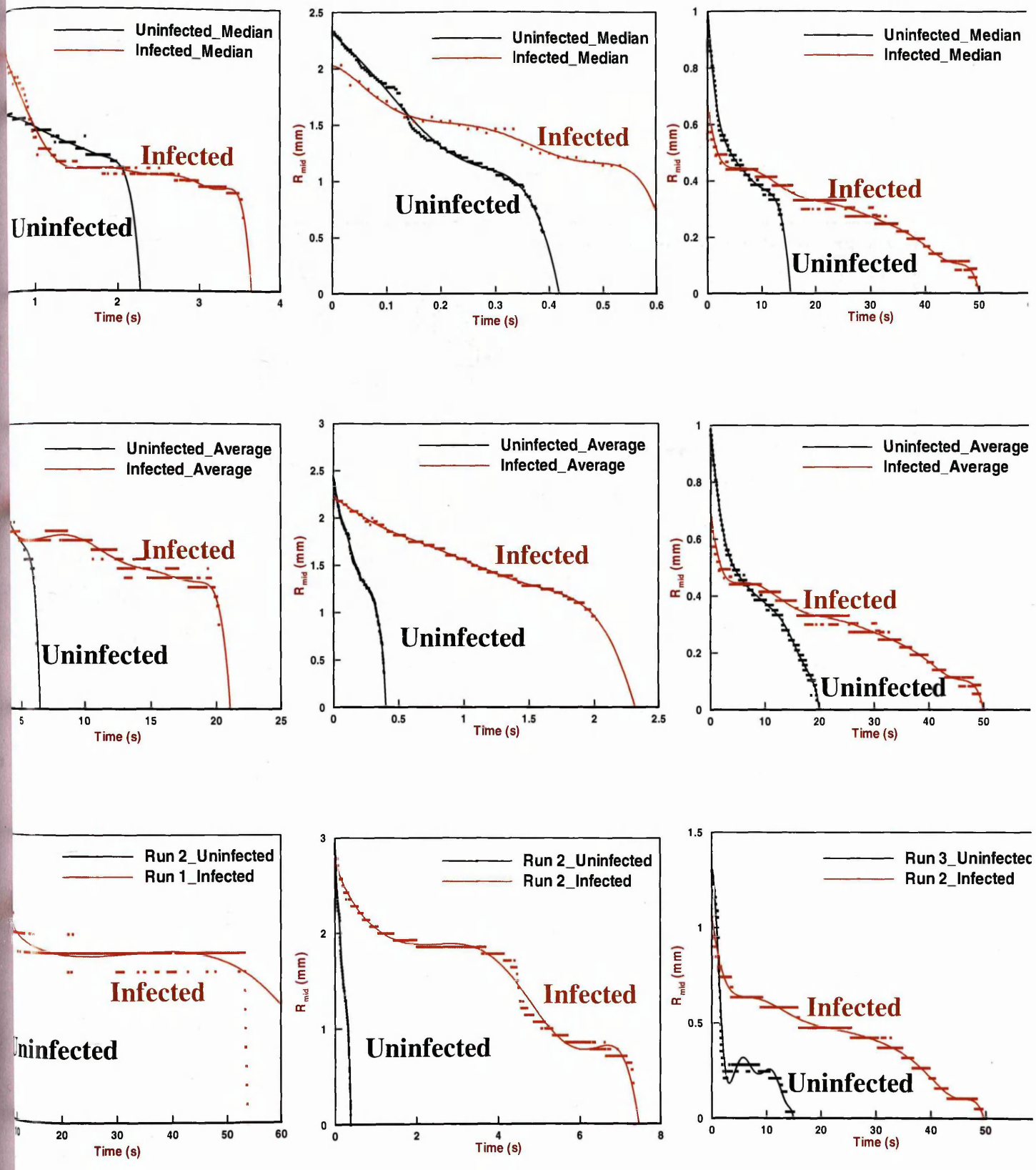

Figure 6.4. R_{mid} versus time; selected experimental data, three samples, infected and uninfected states; a) criteria 1, b) criteria 2, c) criteria 3

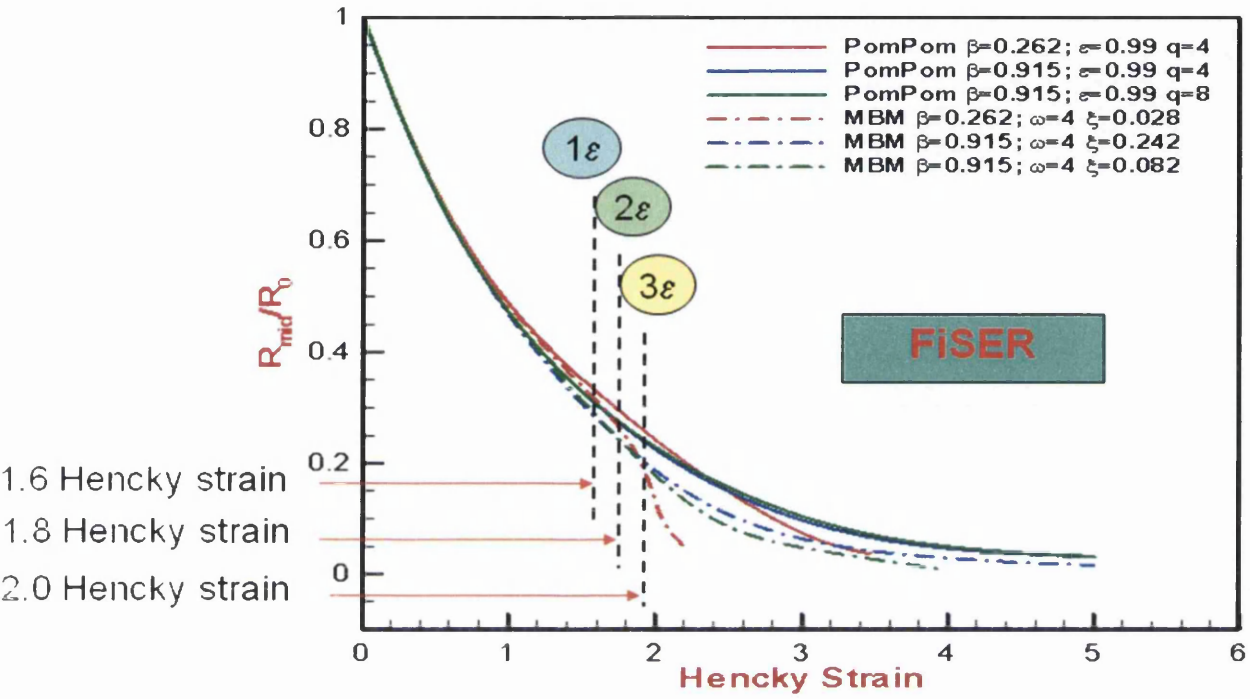

Figure 6.5. FiSER, development of R_{mid}; increasing ε; pom-pom & MBM

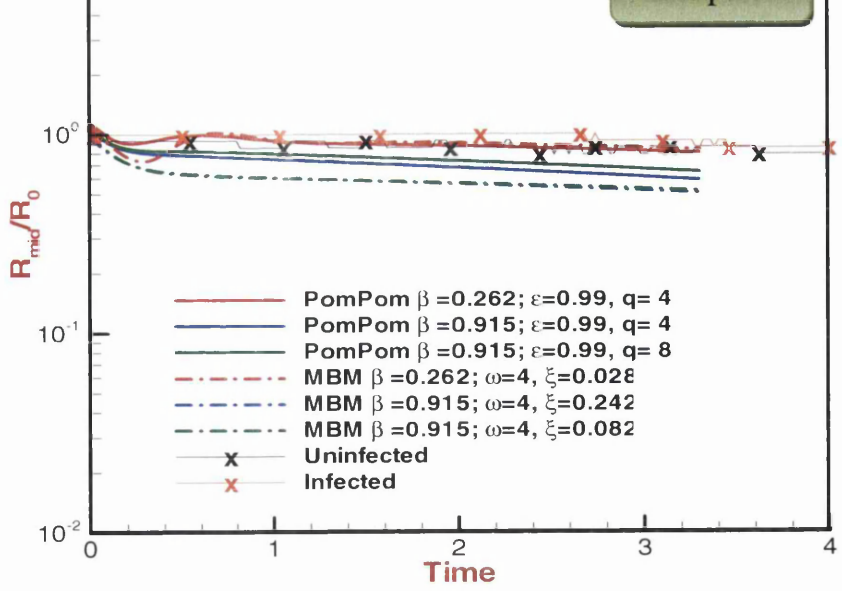

b)

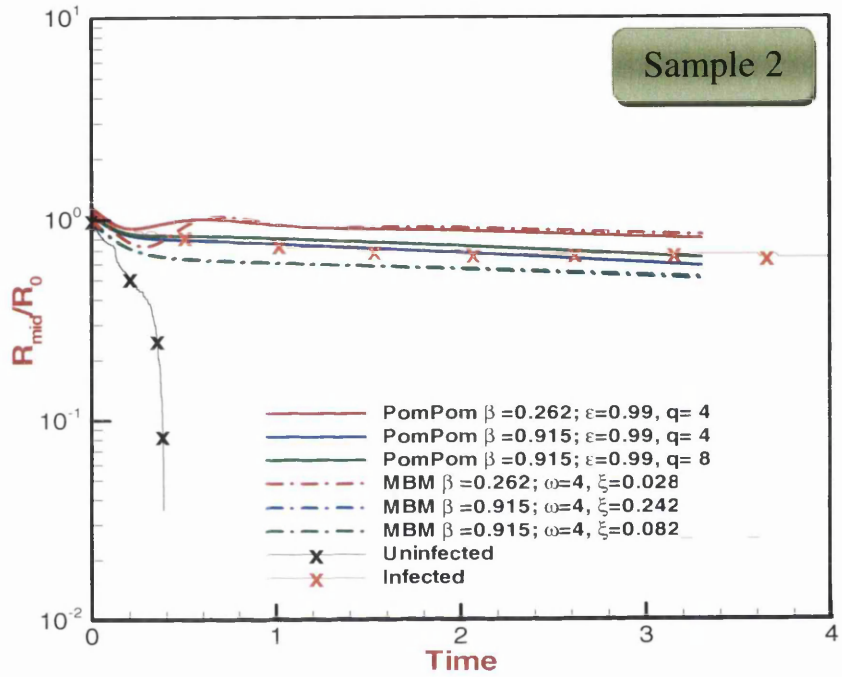

c)

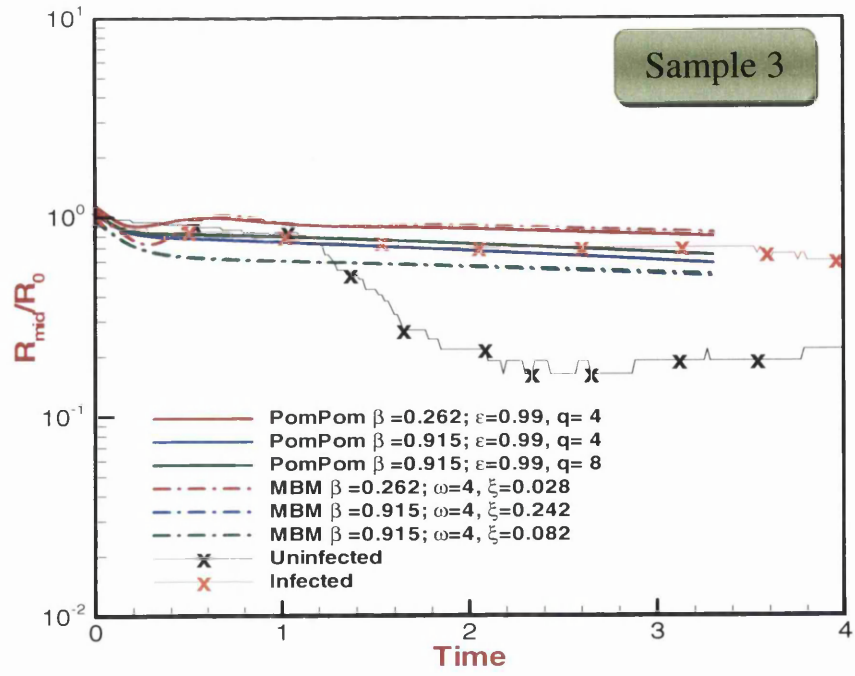

Figure 6.6. R_{mid} versus time, pom-pom and MBM, 3 different samples (a-c), L/D=1.6 (ε_{Hencky} =1.6)

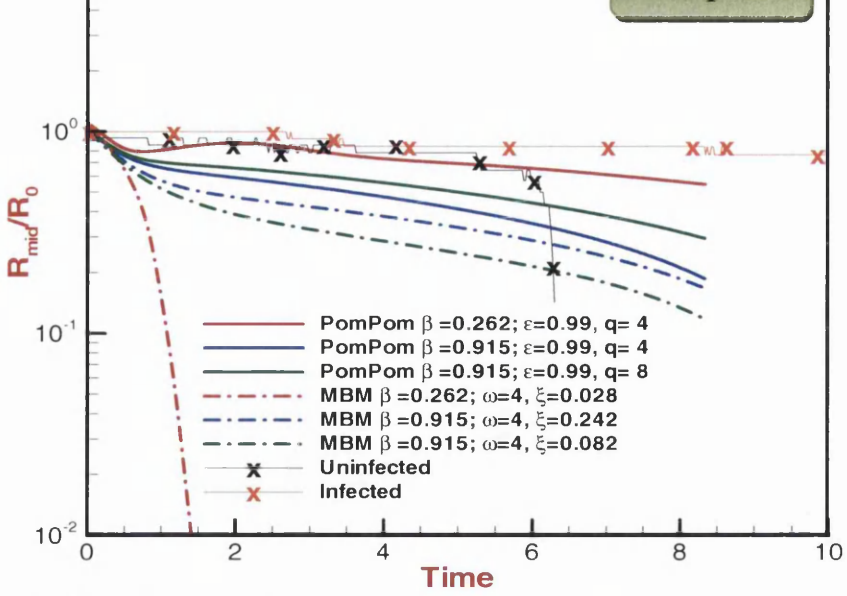

b)

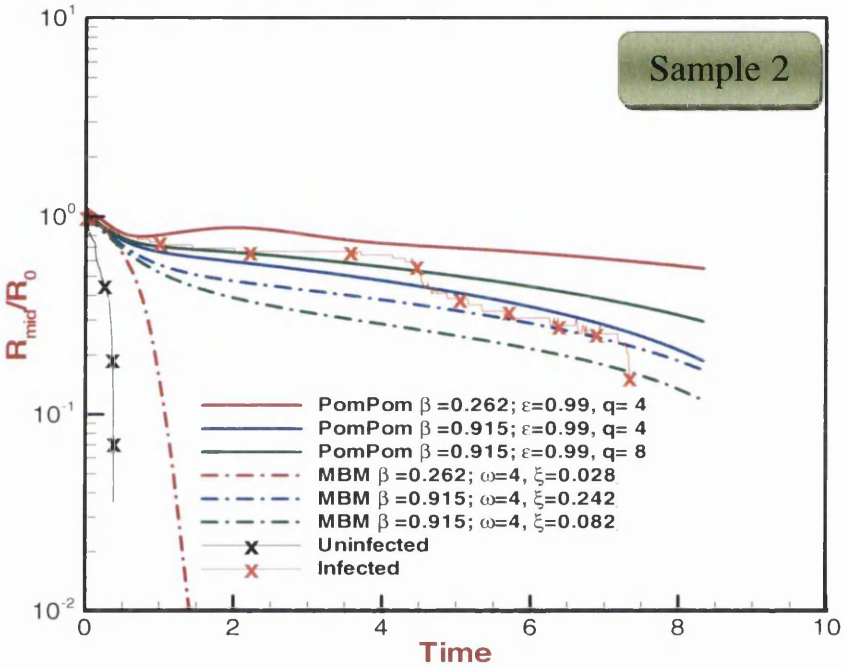

c)

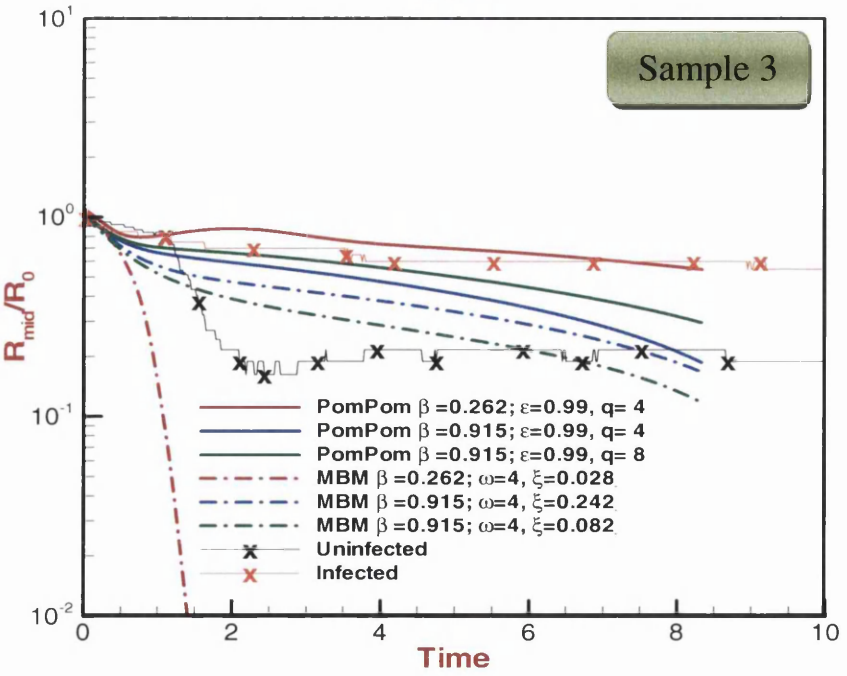

Figure 6.7. R_{mid} versus time, pom-pom and MBM, 3 different samples (a-c), L/D=1.8 (ε_{Henckv} =1.8)

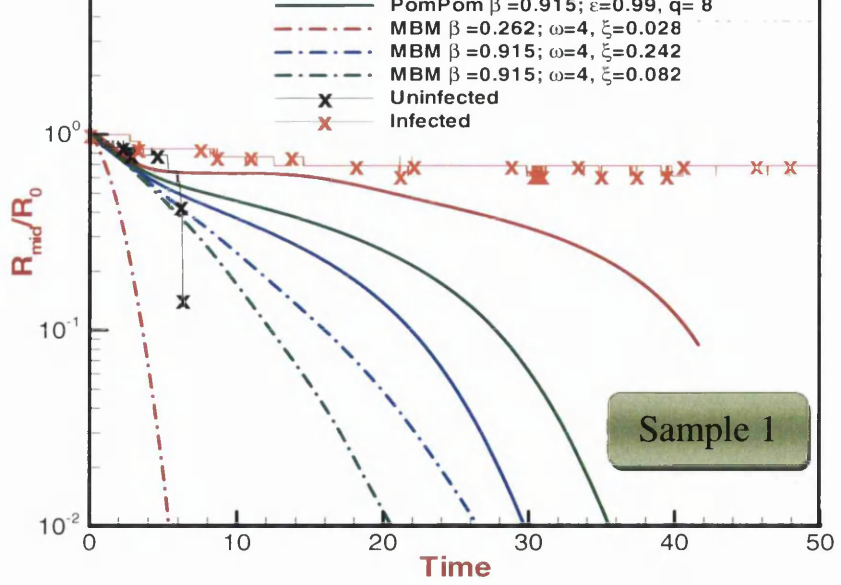

b)

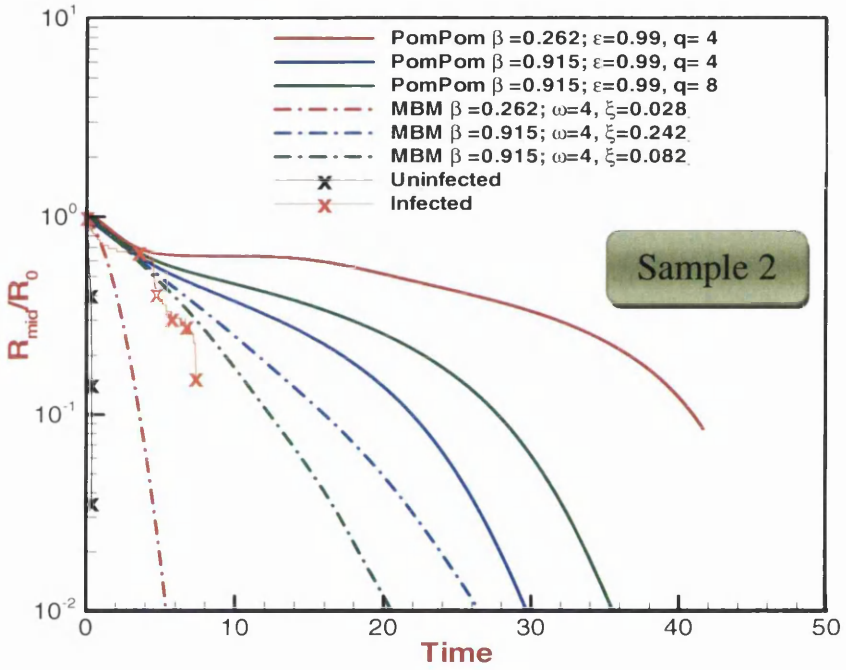

c)

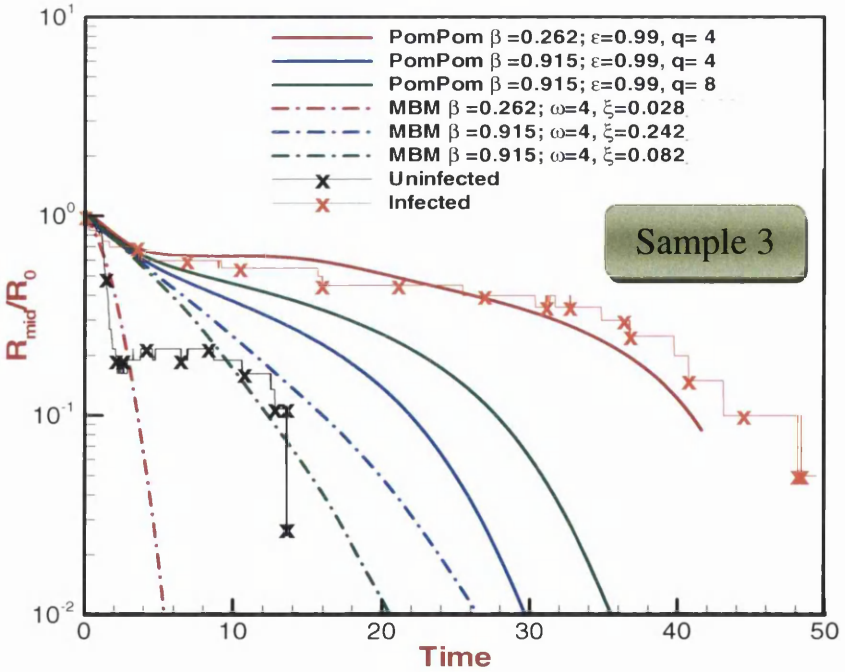

Figure 6.8. R_{mid} versus time, pom-pom and MBM, 3 different samples (a-c), L/D=2 (ε_{Hencky} =2)

m-pom

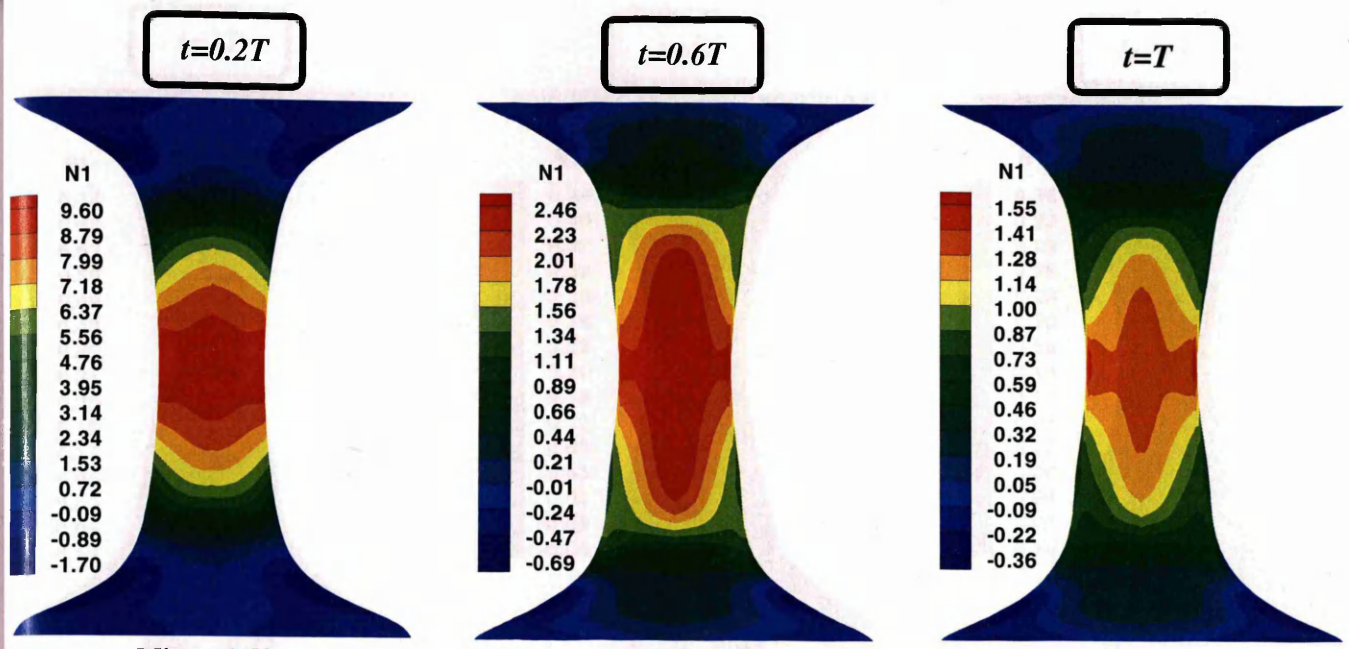

Min: -1.70
Max: 9.60

Min: -0.69
Max: 2.46

Min: -0.36
Max: 1.55

MBM

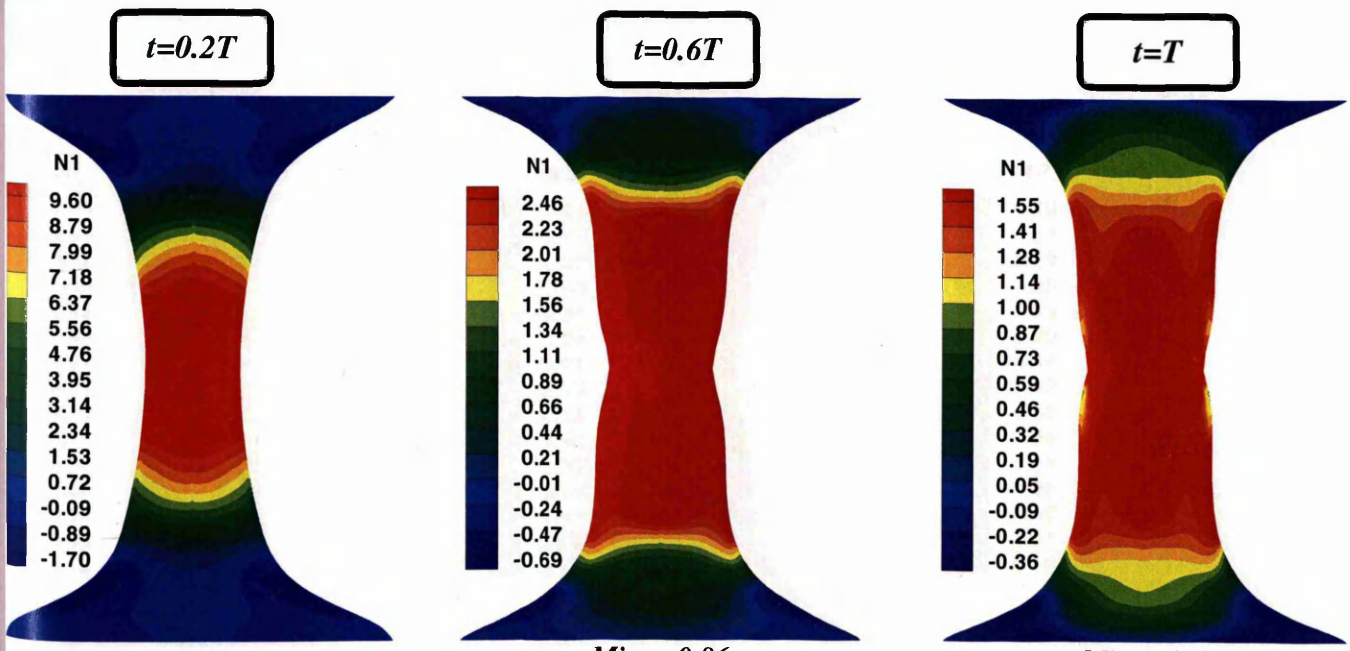

Min: -1.91
Max: 12.83

Min: -0.86
Max: 5.30

Min: -0.63
Max: 2.71

Figure 6.9(a-b). First normal stress (N_1) contours; β=0.262, L/D=1.6 (ε_{Hencky} =1.6): a) pom-pom b) MBM; t={0.2T, 0.6T, T} time units, (T)=0.8s

pom-pom

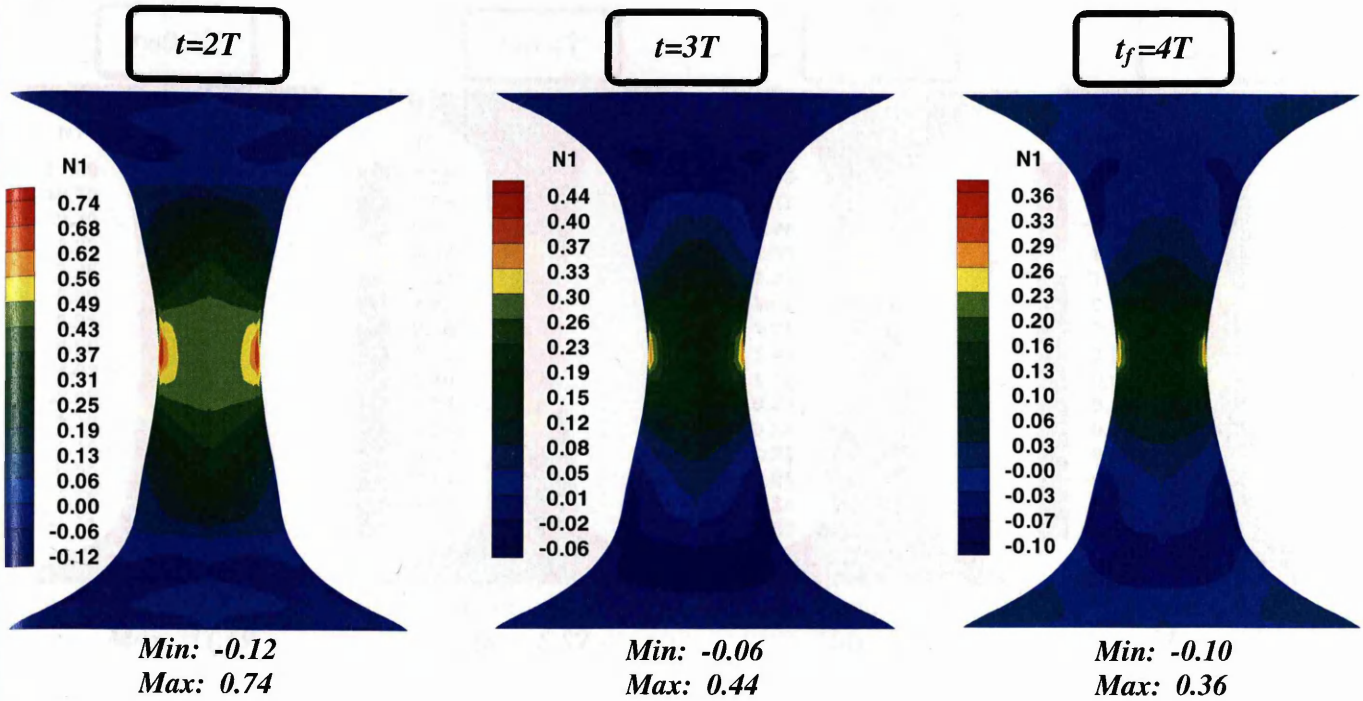

Min: -0.12 *Max: 0.74*

Min: -0.06 *Max: 0.44*

Min: -0.10 *Max: 0.36*

MBM

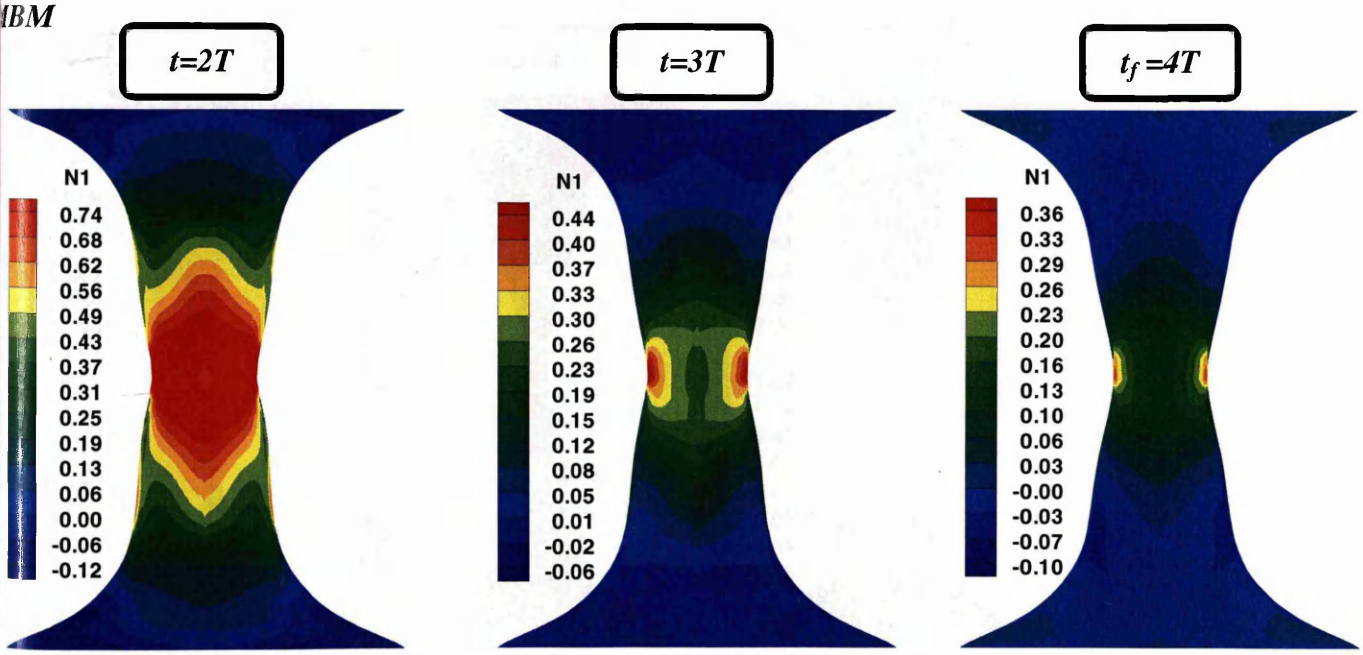

Min: -0.14 *Max: 1.11*

Min: -0.07 *Max: 0.51*

Min: -0.08 *Max: 0.35*

Figure 6.9(c-d). First normal stress (N_1) contours; β=0.262, L/D=1.6 (ε_{Hencky} =1.6): c) pom-pom d) MBM; t={2T, 3T, 4T} time units, (T)=0.8s

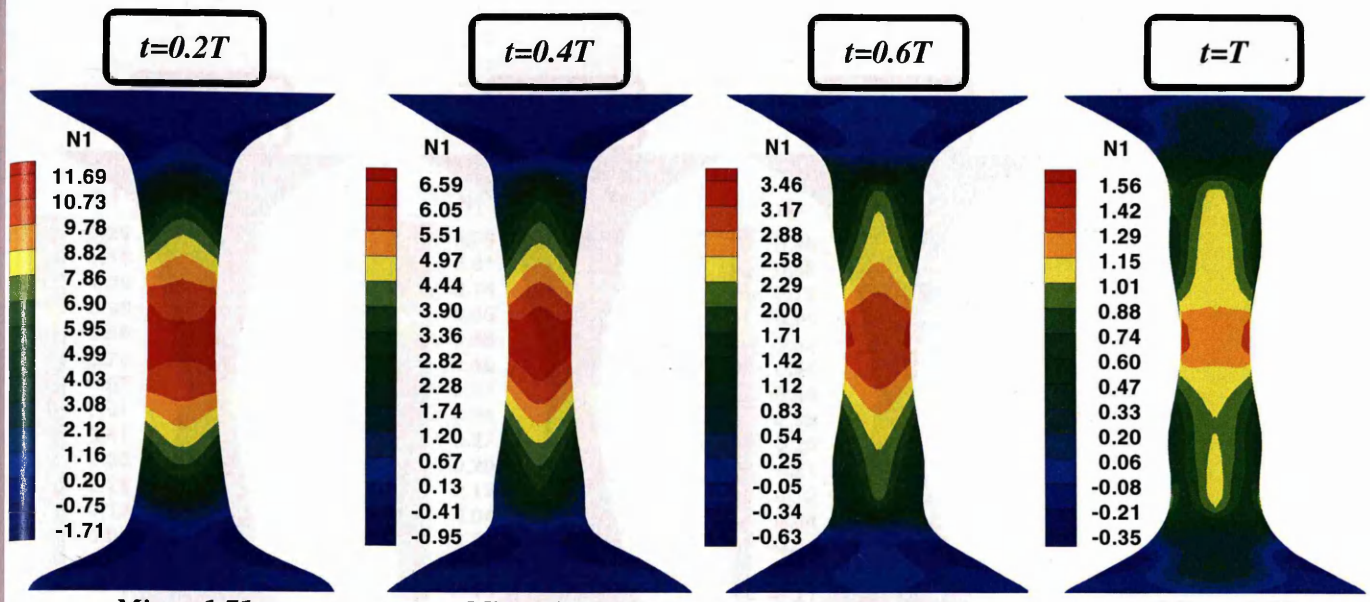

Min: -1.71
Max: 11.69

Min: -0.95
Max: 6.59

Min: -0.63
Max: 3.46

Min: -0.35
Max: 1.56

BM

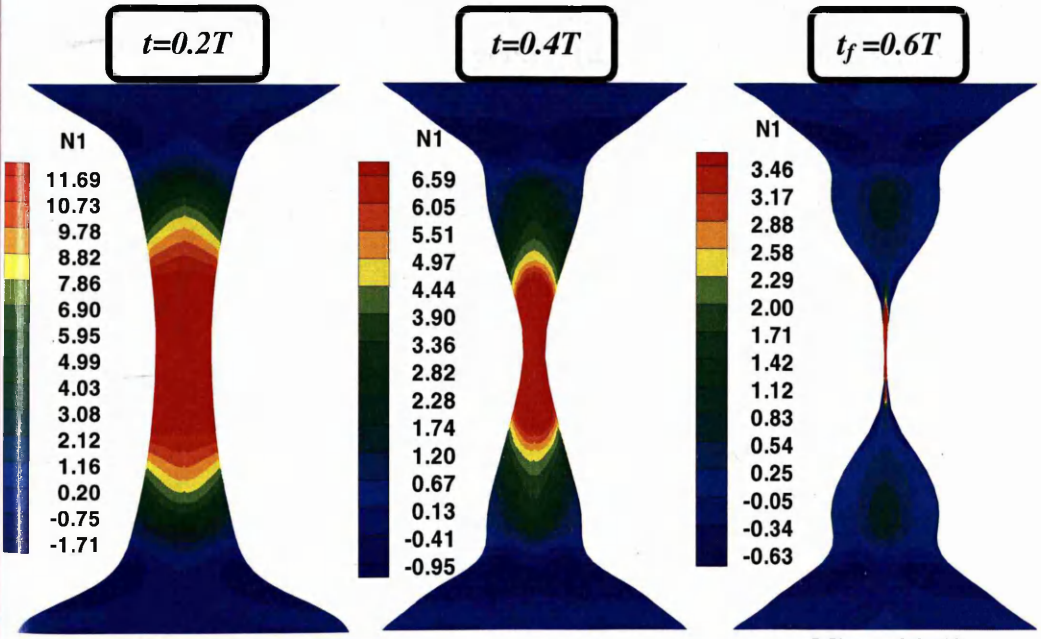

Min: -1.85
Max: 15.05

Min: -1.01
Max: 17.39

Min: -20.68
Max: 21.17

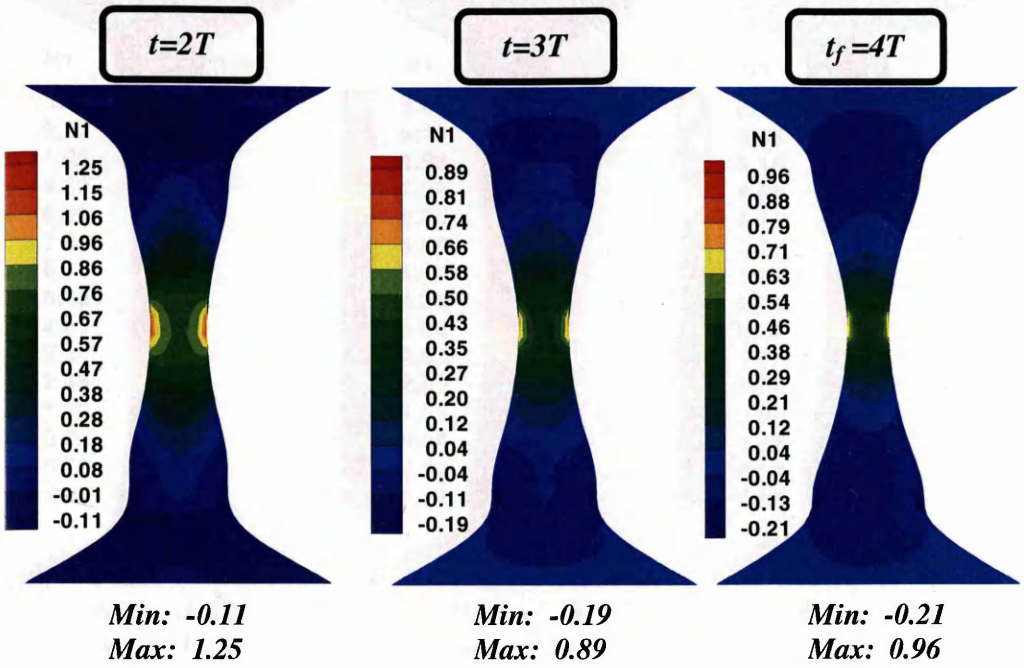

Figure 6.10. First normal stress (N_1) contours; β=0.262, L/D=1.8 (ε_{Hencky} =1.8):
a) pom-pom, t={0.2T, 0.4T, 0.6T, T}; b) MBM, t={0.2T, 0.4T, 0.6T};
c) pom-pom, t={2T, 3T, 4T} time units, (T)=2.05s

-pom

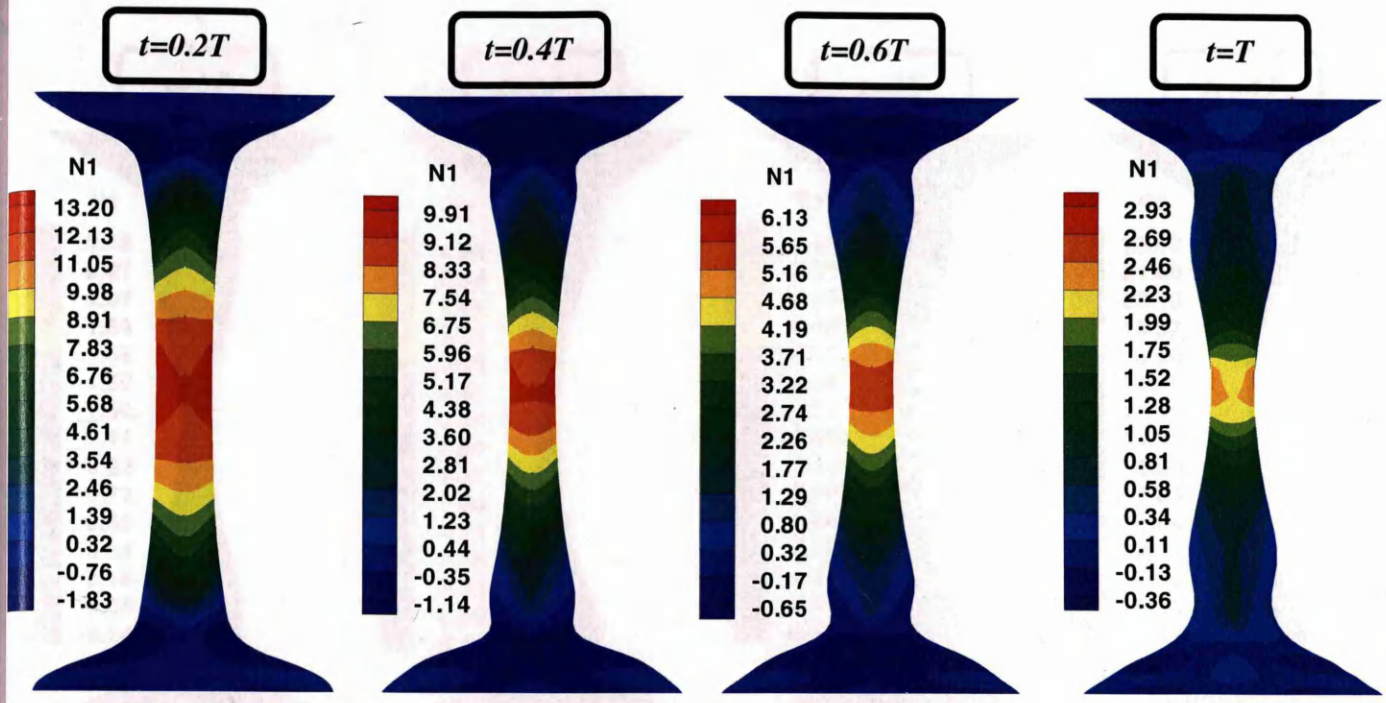

Min: -1.83
Max: 13.20

Min: -1.14
Max: 9.91

Min: -0.65
Max: 6.13

Min: -0.36
Max: 2.93

BM

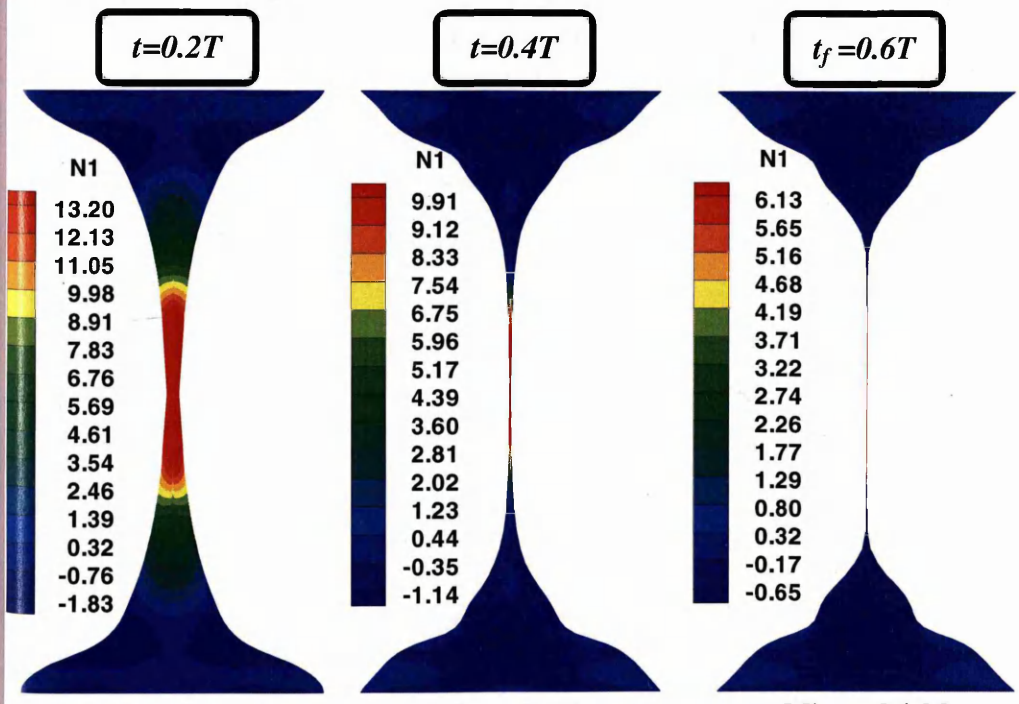

Min: -2.60
Max: 18.17

Min: -3.93
Max: 20.05

Min: -24.28
Max: 24.51

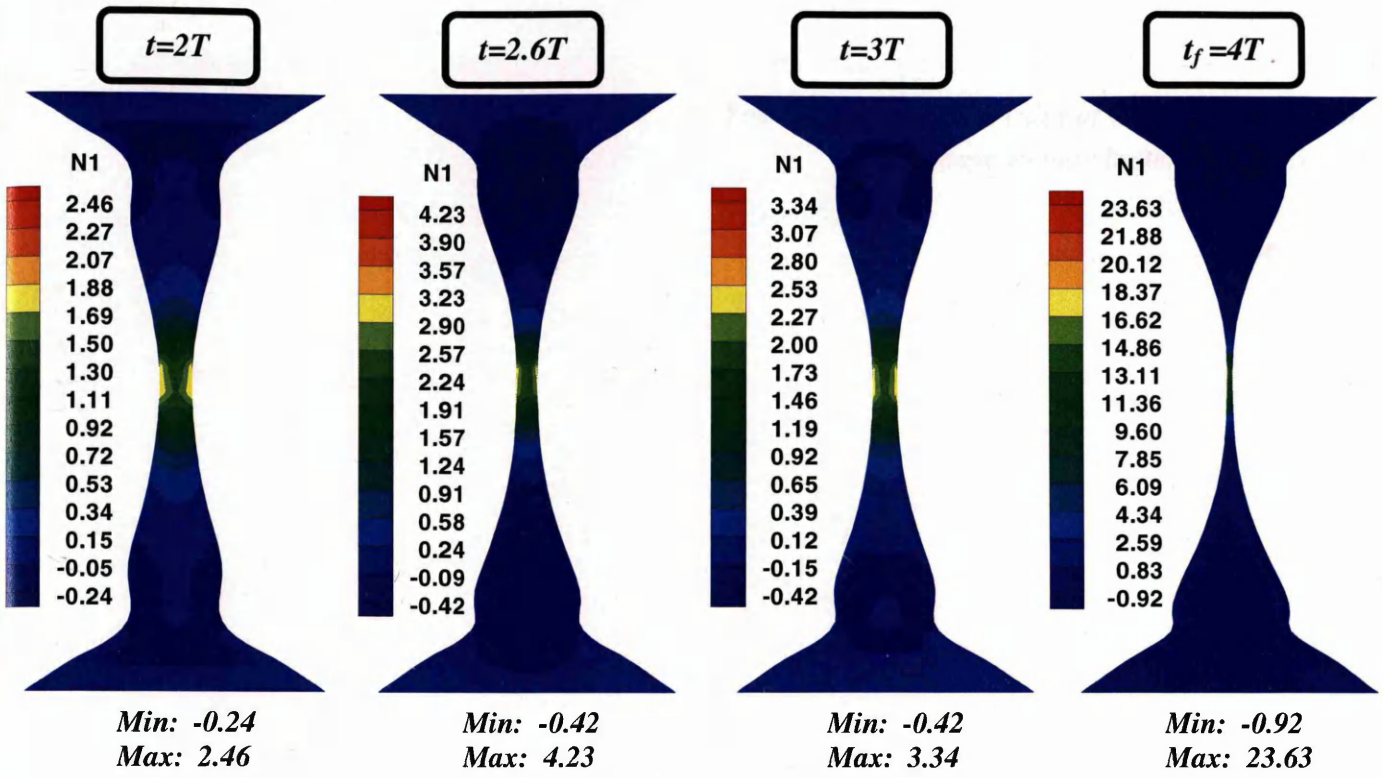

Figure 6.11. First normal stress (N_1) contours; β=0.262, L/D=2 (ε_{Hencky} =2): a) pom-pom, t= {0.2T, 0.4T, 0.6T, T}; b) MBM, t= {0.2T, 0.4T, 0.6T}; c) pom-pom, t={2T, 2.6T, 3T, 4T} time units, (T)=10.5s

You have to learn the rules of the game. And then you have to play better than anyone else.

Albert Einstein

Chapter 7
Concluding Remarks

This work has tacked the two bases of rheology, computational simulation and experimental rheometry. This has involved numerical solutions for two complex viscoelastic flow test problems: flows in axisymmetric hyperbolic 4:1:4 contraction/expansion configurations (dominated by shear deformation), and filament stretching and step-strain (dominated by extensional deformation). In addition, rheological characterization (experimental rheology) has been conducted for three polymer melts.

Through this study, a time-dependent hybrid finite element/finite volume (*fe/fv*) parent-subcell scheme has been employed, which has been developed in-house by the computational rheology group (INNFM) at Swansea University.

First, flow in a rounded-corner hyperbolic 4:1:4 contraction/expansion has been considered, comparing predictions for *time-dependent* thixotropic Modified Bautista-Manero (MBM) models and *time-independent* network-based EPTT models., This has been conducted under comparatively moderate and strong hardening response, for highly-polymeric and solvent-dominated fluids. At low-levels of elasticity ($We \rightarrow 0$), the MBM (micellar model) inconsistently predicted *epd*–values, as opposed to the network-based EPTT. Here, the MBM data-curve underpredicted the *epd* values at the Stokesian limit by {40%, 10%} for the {MH, SH} polymeric fluids, respectively. To overcome this anomaly in *epd* at low deformation rates (equivalent to low *We*), a correction to the MBM model has been proposed that introduces elastic effects into the structure equation (destruction) [7.1]**.** In this context, two model variants have been proposed:- namely, (i) a model in which the energy dissipated by the polymer to breakdown the structure of the material (NM_τ_p model) is used; and (ii) an option that considers the polymeric+solvent dissipation in its structural dynamic readjustment (NM_T model).

The capability of new models has been examined in predicting enhanced *epd.* For all three types of constitutive models used - MBM, new micellar models (NM_τ_p & NM_T) and EPTT- the relationship has been considered, under rising *We,* between the pressure-drop, the first normal stress difference (N_1) (along the symmetry line in extension, and the boundary wall in shear), the strain rate across the geometry and the material functions involved.

Advancing from the knowledge gained in our previous studies on the modelling of wormlike micellar solutions through contraction-expansion configurations [7.1], the influence of the shape of the contraction/expansion configuration and its effect on *epd* prediction has been demonstrated. This has been achieved by comparison against findings for the rounded-corner abrupt 4:1:4 geometry flow.

It should be noted that the majority of experimental research performed on wormlike micellar systems relates to steady-state (axisymmetric or planar),

oscillatory and extensional measurements, on standard commercial devices (to mimic ideal/model flow scenarios). The role for numerical simulations, as performed in the present study, is particularly useful in providing insight into complex flow response for these complex wormlike micellar systems. This may aid in future to help design and develop more advanced experimental techniques suitable for such material systems (tackling their inherent complexities, such as shear-banding behaviour).

Precise knowledge of the rheological behaviour of polymers (polymer melts in particular) is the key to setting up an accurate process operating window, typically governing temperature and flow rates, and in the development of new polymeric materials for smooth processing control. Also, rheological information is required for process simulation, which is considered as an essential component of any new process setup. Due to the sensitivity of polymer melts to small changes in polymeric structure, use of rheometers in the linear deformation-rate range is a most convenient strategy of choice to rheologically characterize polymer melts.

Chapter 5 has presented the experimental work and characterisation results for three polymer-melts. The study focuses on the determination of the dynamic viscoelastic properties, using small amplitude oscillatory shear (SAOS) technique, of High-Density Polyethylene (HDPE), Nylon 11 (Polyamide-PA11), and Poly-Vinylidene Fluoride (PVDF) melt, which were measured using a controlled-strain rheometer (TA Instruments ARES-G2). Frequency sweep measurements were performed in a frequency range from 100 down to 0.1 rad/s (in order to limit the effect of degradation), with the strain level of 1% (in the linear regime) at temperatures of 220°C, 230°C, and 240°C, respectively. The method of taking data measurements in a few intervals of frequency has been suggested to avoid problems with either long exposure time at high temperature, or with taking data in a time shorter than the thermal stability time. This approach allows for a small improvement in precision under the data acquisition. The data thus obtained has been interpreted in terms of the relevant shear viscosities. It is fairly apparent that a significant improvement in precision has been obtained at higher temperatures and lower frequencies. However, in the case of the PA11 melt, the viscoelastic properties cannot be investigated by a discrete frequency-sweep, since the substance has been found to change dramatically during the measurement. This renders a meaningful

status description almost impossible. An alternative procedure is to speed-up the data acquisition time – known as a Multiwave test, whereby investigating the frequency dependency proves to significantly shorten the measuring time.

Using the Cox-Merz rule, dynamic oscillatory data (in terms of $G^{'}, G^{''}$) were fitted to predictions derived according to the Cross model. Here, the experimental data collected was effectively used by others as characteristic material input-data to the same fe/fv simulation software suite, tackling such application problems as extrudate-swell and tube-tooling cable-coating (see [7.2]).

In chapter 6, combined experimental and computational studies have been performed for Capillary Break-up Extensional Rheometry (CaBER). This technique has been considered to predict extensional rheological response for the biofluid sputum; and to correlate this to the degree of infection in patients suffering from Chronic Obstructive Pulmonary Disease (COPD). In this manner, a measure of extensional rheology through R_{mid}-evolution of sputum (experimental), has been compared against that derived from numerical prediction. To this end, sputum samples were derived from three doner-patients with COPD, at two stages of disease development (stable and exacerbation - without stimulation). Rheological models employed for this purpose are the pom-pom (kinetic-molecular theory) (SXPP) and the MBM (time-dependent thixotropic) models. Typically, the dynamic evolution of the filament-midpoint has been monitored during this process of necking and failure, with the aim of linking this temporal data with that emerging from counterpart experimental trials. The aim is to link this type of data with that emerging from experimental/clinical trials, to provide a diagnostic tool (biomarker) revealing insight on the state of disease-disorder and to aid subsequent resultant (early) treatment.

The broad distribution of experimental temporal results across three patient-samples has suggested the necessity of adopting specific criteria, to derive consistent correlations between infected versus uninfected data. In this manner, three different criteria have been investigated through this study. The most appropriate criteria emerging, amongst the infected data, has been found to be that dependent on the longest-time to break-up, whilst possessing the larger extensional viscosities (η_e). For the uninfected data, the closest R_{mid} starting-value to the infected state has been chosen (equivalencing their step-strain Hencky-strain). The sensitivity of the

simulation results to the choice of aspect ratio (L/D=1.6, 1.8 and 2) has also been investigated to predict suitable windows for experimental operation sets. The outcome suggests that the results commencing from Hencky-strain 2 is the more superior choice to adopt.

Overall, the capability has been demonstrated of these rheological models (pom-pom and MBM) to qualitatively predict rheological properties that can gainfully be used to assess the disparity between infected and uninfected sputum samples. This points the way forwards towards a biomarker for COPD (process and device accordingly), in detecting the severity of COPD-infection with appropriate criteria and parameter sets. In general, pom-pom R_{mid}-predictions (with q=4, ε_{pom}=0.99, α=0 and β=0.262) follow similar patterns to those recorded for infected sputum. While, measured R_{mid}-profiles for uninfected sputum test-cases appear to be in good agreement with R_{mid}–predictions for the thixotropic MBM (ω=4, ξ=0.028 and β=0.262) model.

References

[7.1] J.E. López-Aguilar, M.F. Webster, H.R. Tamaddon-Jahromi, O. Manero, *A new constitutive model for worm-like micellar systems - Numerical simulation of confined contraction-expansion flows.* J. Non-Newton. Fluid Mech. **204** (2014) 7-21.

[7.2] A, Al-Muslimawi, H.R. Tamaddon-Jahromi and M.F. Webster, *Numerical computation of extrusion and draw-extrusion cable-coating flows with polymer melts.* Appl. Rheol. **24** (2014) 34188. DOI: 10.3933/ApplRheol-24-34188